# Aggregation and Fibrillogenesis of Insulin

# Monitored by

# Atomic Force Microscopy

DISSERTATION

zur Erlangung des akademischen Grades

Doktor der Naturwissenschaften

(Dr. rer. nat.)

vorgelegt von

## Dipl.-Chem. Ralf Jansen

aus Wesel

eingereicht beim

Fachbereich Chemie

der Universität Dortmund

Dortmund 2005

*Elisabeth*
*in Dankbarkeit gewidmet*

„Und was wir zu finden wünschen,

das werden wir, gefunden,

mit besonderem Mißtrauen ansehen.“


aus Bertolt Brecht „Leben des Galilei“

An dieser Stelle möchte ich die Gelegenheit wahrnehmen, mich bei allen Personen zu bedanken, die zum Gelingen der Doktorarbeit beigetragen haben.

Zuerst gebührt mein Dank meinem Doktorvater Herrn Prof. Dr. Roland Winter für die Gelegenheit an diesem hochinteressanten und fachübergreifenden Thema mit einer der modernsten und vielseitigsten Untersuchungsmethoden zu arbeiten. Neben seiner außergewöhnlichen fachlichen Unterstützung danke ich ihm auch für die vielen ermutigenden Gespräche, die mich bei auftretenden Schwierigkeiten und Rückschlägen nicht verzagen ließen.

Herrn Prof. Dr. Alfons Geiger danke ich für sein besonderes Interesse und die freundliche Übernahme des Korreferats.

Ganz besonderer Dank gilt Herrn Dr. Claus Czeslik, der mich mit kritisch-wohlwollendem Interesse, hohem wissenschaftlichen Sachverstand sowie steter Hilfsbereitschaft während meiner Diplomarbeit und Promotion begleitete. Ausdrücklich würdigen möchte ich seinen über die normalen Grenzen hinausgehenden menschlichen Einsatz.

Für die zahlreichen Ratschläge auf dem Gebiet der Molekularbiologie und Gedanken-experimente auch abseits der üblichen Wege möchte ich an dieser Stelle ganz besonders herzlich unserem Kooperationspartner Herrn Dr. Wojciech Dzwolak danken.

Dankend hervorheben möchte ich ausdrücklich Herrn Dipl.-Chem. Stefan Grudzielanek für die unschätzbaren fachlichen und nichtfachlichen Diskussionen, seine wertvollen Anregungen und sein uneigennütziges Engagement.  Neben seiner kameradschaftlichen Unterstützung werden mir stets  die vielen lustigen Momente in freudiger Erinnerung bleiben.

Nicht verschwiegen werden sollen auch alle übrigen wissenschaftlichen und nichtwissenschaftlichen Mitarbeiter des Lehrstuhls für Physikalische Chemie I, die durch ihre Kollegialität und Hilfsbereitschaft ein wunderbares Arbeitsklima geschaffen haben.

Mein allerherzlichster Dank aber gilt meinem Bruder Dr. Dr. Dirk Jansen und meinen Eltern für ihre großartige Unterstützung. Ihr Beistand war stets Vorraussetzung für mein gesamtes Chemiestudium.

# Contents

# Publications

1. Czeslik, C., Jansen, R., Ballauff, M., Wittemann, A., Royer, C. A., Gratton, E. and Hazlett, T. (2004). Mechanism of protein binding to spherical polyelectrolyte brushes studied *in situ* using two-photon excitation fluorescence fluctuation spectroscopy. *Phys. Rev. E* **69**, 021401-1 - 021401-9.

2. Dzwolak, W., Ravindra, R., Nicolini, C., Jansen, R. and Winter, R. (2004). The diastereoisomeric assembly of polylysine is the low-volume pathway for preferential formation of β-sheet aggregates. *J. Am. Chem. Soc.* **126**, 3762 - 3768.

3. Dzwolak, W., Smirnovas, V., Jansen, R. and Winter, R. (2004). Insulin forms amyloid in a strain-dependent manner: An FT-IR spectroscopic study. *Protein Sci.* **13**, 1927 - 1932.

4. Dzwolak, W., Jansen, R., Smirnovas, V., Loksztejn, A., Porowski, S. and Winter, R. (2005). Template-controlled conformational patterns of insulin fibrillar self-assembly reflect history of solvation of the amyloid nuclei. *Phys. Chem. Chem. Phys.* **7**, 1349 - 1351.

5. Jansen, R., Grudzielanek, S., Dzwolak, W. and Winter, R. (2004). High pressure promotes circularly shaped insulin amyloid. *J. Mol. Biol.* **338**, 203 - 206.

6. Jansen, R., Dzwolak, W. and Winter, R. (2005). Amyloidogenic self-assembly of insulin aggregates probed by high resolution atomic force microscopy. *Biophys. J.* **88**, 1344 - 1353.

7. Dzwolak, W., Grudzielanek, S., Smirnovas, V., Ravindra, R., Nicolini, C., Jansen, R., Loksztejn, A., Porowski, S. and Winter, R. (2005). Ethanol-perturbed amyloidogenic self-assembly of insulin: Looking for origins of amyloid strains. *Biochemistry*, in press.

8. Grudzielanek, S., Jansen, R. and Winter, R. (2005). Solvational tuning of the unfolding, aggregation and amyloidogenesis of insulin. *J. Mol. Biol.*, in press.

# List of Abbreviations

| | |
|---|---|
| Aβ | amyloid β-peptide |
| AD | Alzheimer's disease |
| AFM | atomic force microscopy |
| Ala | alanine |
| ASA | accessible surface area |
| Bov | bovine |
| BSE | bovine spongiform encephalopathy |
| CMAFM | contact mode atomic force microscopy |
| Cys | cysteine |
| FTIR | Fourier transform infrared |
| EM | electron microscope |
| EtOH | ethanol |
| HHP | high hydrostatic pressure |
| His | histidine |
| Hum | human |
| Ig | immunoglobulin |
| NMR | nuclear magnetic resonance |
| PAA | polyamino acid |
| PDL | poly(D-lysine) |
| PLL | poly(L-lysine) |
| Porc | porcine |
| PZT | plumbum zirconate titanate |
| SEM | scanning electron microscope |
| SPM | scanning probe microscope |
| STM | scanning tunnelling microscope |
| TFE | 2,2,2-trifluoroethanol |
| Thr | threonine |
| TMAFM | tapping mode atomic force microscopy |
| Val | valine |
| VDW | van der Waals |
| wt % | weight per cent (w/w per cent) |

# 1 Introduction

In November 1901, a mentally confused lady who suffered from amnesia and could not even recognize her husband was admitted to the "Urban Asylum for Lunatics and Epileptics" in Frankfurt am Main. The psychiatrist and neuropathologist Alois Alzheimer witnessed the patient who went down in medical history as "Auguste D.", losing more and more of her memory and self-awareness. After she had been dozing towards her premature end for five years the attending physicians determined early senile dementia as cause of death. Alzheimer could not accept that pathological result on account of her age and peculiar behavior. Therefore he examined Auguste Deter's brain under the microscope and discovered millet seed-sized deposits in the cerebral cortex, which he associated with her illness [Brettin, 2001; Groß, 2003].
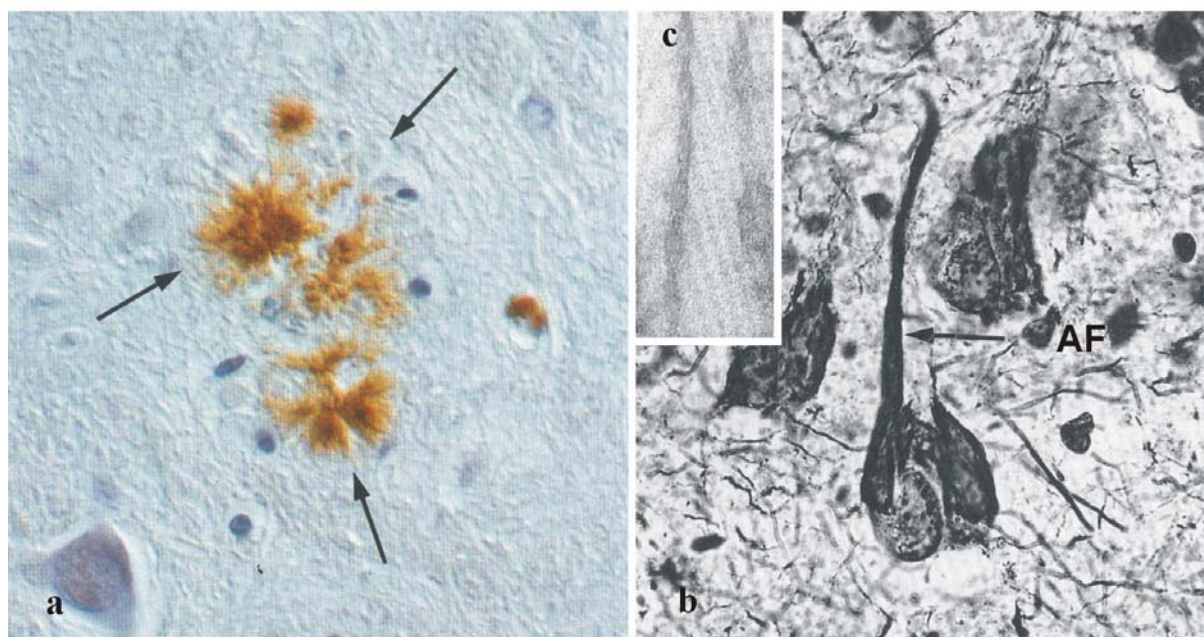


**Figure 1.1** (a) Immunohistochemical representation of an Alzheimer-plaque (arrows; magnification 1 : 400). (b) Alzheimer fibrils (AF) in cytoplasm and dendrite of ganglion cells in parietalcortex of a man with Alzheimer-dementia who had reached the age of 63 years (magnification 1 : 200). (c) Electron microscope (EM) image of paired helical Aβ-filaments (with a periodicity of 80 nm) as morphological correlative of the cytoskeletal malfunction [Schlote et al., 1993].

Today's pathologists diagnose this illness, which is now known as "Alzheimer's disease" (AD), by several anatomical characteristics: The brain of the person concerned begins to shrink due to the loss of cortical neurons with a corresponding loss of synapses. Inside the

necrotized neuronal tissue depositions of insoluble neurofibrillar plaque-coated tangles, composed of ordered amyloid β-peptide (Aβ) aggregates, are found [Katzman and Saitoh, 1991; Schlote et al., 1993; Selkoe, 1991] (cf. Fig. 1.1).

AD has evolved from a strange individual case to the major dementing disorder of the elderly within one century. In Germany, 850,000 citizens are currently affected. As a result of increased life expectancy there will be a doubling of the absolute number of disorders in the year 2015. The risk coming down with AD increases exponentially with age: Every twentieth in the group of 65 years old persons, every fifth in the group of 80 aged and every second from 90 years onwards will be affected [Kupczik, 2004]. If no therapeutic agent is found, AD will replace cancer as second most common cause of death in 50 years [Brettin, 2001]. In terms of economics, Medicare, a U.S. public health insurance system, has evaluated that the expenditures of medical treatment for AD will treble up to a value of 190 billion dollars per annum within the next ten years [Kupczik, 2004].

Other neurodegenerative disorders such as Parkinson's disease, Creutzfeldt-Jakob's disease, bovine spongiform encephalopathy (better known as BSE) or Huntington's disease are also accompanied by the appearance of stable, ordered, filamentous protein aggregates, commonly referred to as amyloid fibrils. The corresponding diseases are generally termed amyloidoses. They are characterized by the conversion of a specific protein or protein fragment from its natural soluble form into insoluble fibrils, which accumulate as "local", "organ-limited" or "general" (distributed throughout several vital organs) deposits in diverse regions of the body [Bellotti et al., 1999; Dobson, 1999; Linke, 1996; Rochet and Lansbury, 2000; Serpell, 2000; Uversky and Fink, 2004]. Actually, there is a list of 24 proteins, neither genetically nor structurally related, which are known to be involved in various amyloidoses [Uversky and Fink, 2004] (see Appendix, Table 7.1).

Concerning these differences amyloid fibrils share hallmarking common properties, including a similar fibrillar, microscopic morphology (i.e. bundles of straight, rigid fibrils ranging in width from 30 to 150 Å and in length from 1000 to 16000 Å [Sipe and Cohen, 2000]), a cross-β alignment of their constituting polypeptide chains and Congo Red binding [Sunde and Blake, 1998]. Thus, it has been proposed that amyloid formation is a generic property of the polypeptide backbone. Amyloid formation is favored whenever intermolecular interactions between polypeptide backbones (are allowed to) overrule specific intramolecular native side-chain contacts within a folded protein. Hence, many proteins, perhaps all, are potentially able to form amyloid fibrils under appropriate conditions [Chiti et al., 1999; Pertinhez et al., 2001; Fändrich and Dobson, 2002]. In other words, the formation of amyloid

presents an alternative to the native folding conformational struggle of a polypeptide chain in order to: (i) reduce its hydrophobic accessible surface area, (ii) saturate hydrogen bonding, and - finally - (iii) reach an alternative "non-native" global free energy minimum. Therefore, subsequent stages of hierarchical amyloid formation may be expected to enhance the burial of hydrophobic residues and the formation of energetically favorable hydrogen bonds.

The physiological and therapeutic importance of insulin, the wealth of biochemical and structural data, and its iatrogenic fibrillar occurrence in tissues of patients with diabetes I and II (which also highlights the relevance of pharmaceutic isolation and purification steps [Brange et al., 1987 and Nielsen et al., 2001a]), make the hormone an excellent model for protein aggregation studies. Especially bovine insulin, which differs from the human variant only at three positions (further details are mentioned later) is known to be very prone to forming fibrils [Brange et al, 1997] under appropriate conditions, such as low pH, high temperature and contact with hydrophobic media [Nielsen et al., 2001a; Sluzky et al., 1991; Gerlough and Bates, 1932; Vigenaud et al., 1933]. Insulin fibrils exhibit characteristic amyloid features: a "cross-β" X-ray diffraction pattern, specific green birefringence with Congo Red when observed in polarized light, a typical shift of the absorption and fluorescence spectra of the dye thioflavin T upon binding, biological dysfunction and high stability against temperature, pressure, low pH and proteases [Waugh, 1948; Burke and Rougvie, 1972; Turnell and Finch, 1992].

The insoluble and non-crystalline character of amyloids (including insulin fibrils) severely limits the number of suitable structure-determining methods, such as X-ray crystallography and solution NMR spectroscopy. However, amyloid formation is a multipathway process, involving multiple intermediate and product assemblies. Hence, the knowledge of the 3D structure of amyloid fibrils and their precursors is critical for understanding the mechanism of fibrillogenesis and might help to get new insights into the molecular basis of amyloid diseases and the aggregation properties of insulin with respect to its long-term stability in commercial pharmaceutical formulations and its utilization in the treatment of diabetes [Thompson, 2003; Bouchard et al., 2000]. One of the most potent research tools used for studying the ultrastructure of amyloids is atomic force microscopy (AFM) [Chamberlain et al., 2000] (see Fig. 1.2). This method contributes significantly to the fields of structural biology [Engel et al., 1999; Morris et al., 1999] and biophysical chemistry [Winter and Noll, 1998], since a nanometer-level resolution is attainable without the need to average over a large number of objects (single-molecule technique). Additional benefits arise from the relatively simple specimen preparation and new milder imaging modes (such as

tapping mode and, derived from that, phase shift imaging) that spare the harsh treatment of delicate samples, which are often employed in electron microscopy (fixation and staining) or X-ray fiber diffraction. In particular, TappingMode™ AFM, in which the scanning probe oscillates sinusoidally and gently taps the sample surface, produces faithful high-resolution images of protein surfaces, even when they are weakly attached to the support or exhibit a soft and therefore easily damageable surface [Möller et al., 1999]. Phase shift based AFM images, which can be recorded in tapping mode, may be more detailed and highlight areas with different elastic properties, and hence may yield new insight into the topology of growing insulin fibrils and early unstructured aggregates [Jansen et al., 2005].
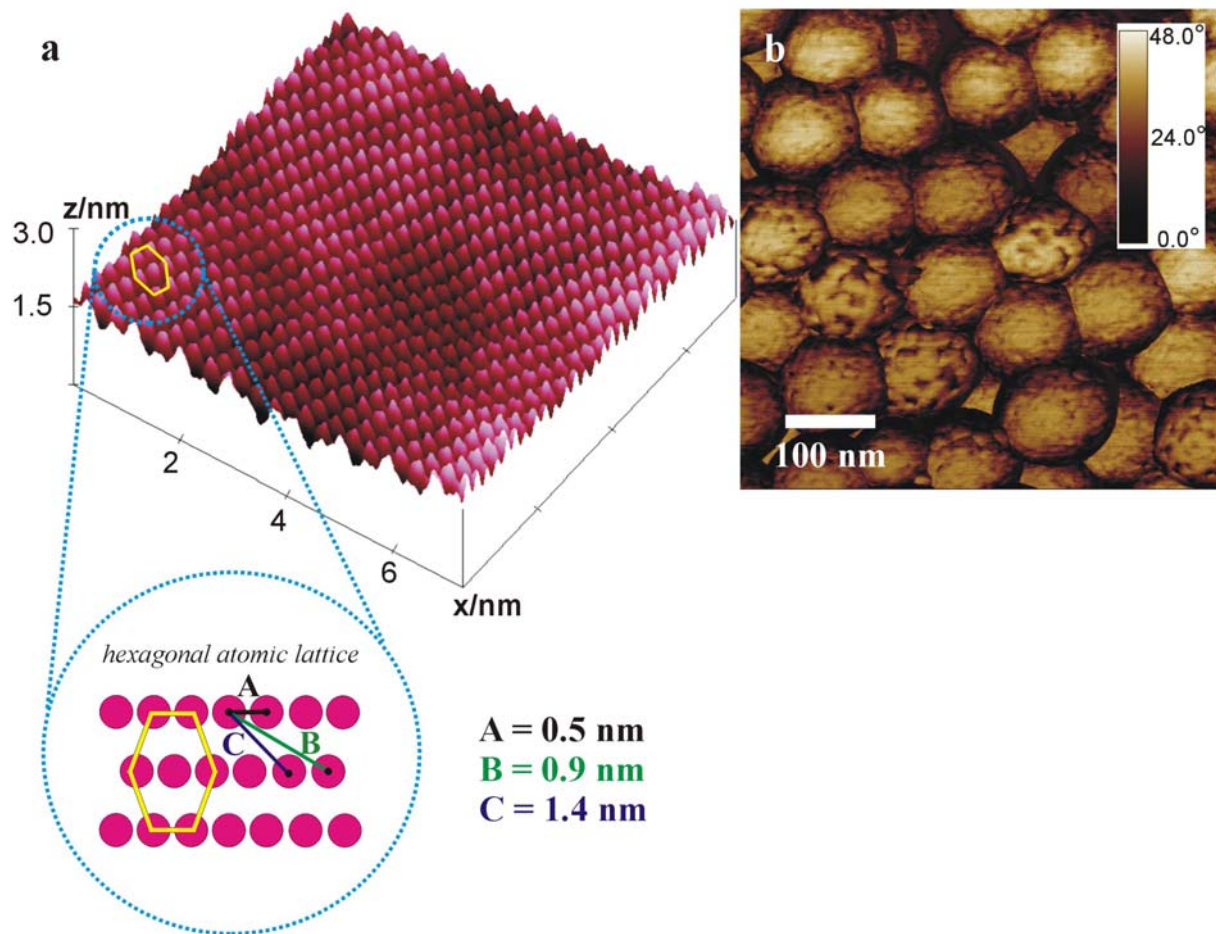


**Figure 1.2** The versatility of the AFM apparatus used in this study can be exemplified by its capability to cover a broad range of length scales within which structures are characterizeable. (a) Atomic scale: High resolution Contact Mode Image of muscovite mica. A hexagonal lattice is observed when looking from the top. The measured spacings between the atoms correspond well to X-ray crystallographic data from the literature (cf. A = 5.19 Å; B = 9.00 Å; C = 13.7 Å [Bailey, 1988]). (b) Mesoscopic scale: AFM image of spherical polyelectrolyte brushes with a polystyrene core (102 nm in diameter) and polyacrylic acid chains. This image was recorded in TappingMode™ at the air and displays the phase shift of the oscillating cantilever tip (cf. [Czeslik et al., 2004]) that particularly highlights the texture on the curved particle surface. The very same apparatus facilitates scanning of objects that range in height over three magnitudes.

The rationale of this work was to gain insight into the hierarchical assembly of insulin amyloid formation and to link these observations to conformational events observed by other biophysical, essentially spectroscopic methods. In order to explore the molecular events that are passed through on the multi-step pathway from the native protein to preaggregated nuclei and their subsequent conversion to fibrillar aggregates of higher complexity, the maturation of insulin fibrils in vitro was monitored by time-lapse AFM. By varying system parameters such as temperature, solvent composition and hydrostatic pressure, the balance between inter- vs. intra-protein interactions can be tuned in order to investigate the effects of various factors that promote or inhibit the protein aggregation and distinct aggregation pathways. In this context, also seeding and cross-seeding experiments were performed to focus on the puzzling phenomenon of prion strains stemming from multiple conformations that are adopted by a single amino acid sequence of the prion precursor protein [Aguzzi, 2004; Tanaka et al., 2004; Tuite, 2004]. The question as to whether "strains" represent an exclusive aspect of prion-type infectivity, or - rather - a feature common to all amyloids, is discussed.

In order to reveal early structures on fibrillogenesis pathways in a distinct manner, supplementary AFM studies with poly(L-lysine) (PLL) and poly(D-lysine) (PDL) were performed. One motivation for choosing these polyamino acids (PAA) was their high molecular weight of approximately 27 kD, which was appropriate to obtain detailed images of early preaggregated and aggregated structures. Also, their "sequenceless" character and hence the lack of distinct folds [Fändrich and Dobson, 2002] was a prerequisite to verify the recently voiced hypothesis of aggregation as being a common generic feature of proteins taking place whenever native intramolecular tertiary contacts are overruled by "polymer-like" intermolecular main chain interactions. Additionally, the stereoisomerism of the PAAs made it possible to explore the phenomenon of cooperative aggregation of enantiomers, which can be studied by the diastereoisomeric assembly of polylysine [Dzwolak et al., 2004a].

# 2   Fundamentals

This chapter provides the essential information concerning the experimental methods used and systems studied in this work.

## 2.1 Atomic Force Microscopy

Scanning Probe Microscopes (SPMs), the family of microscopes among which the AFM is the most versatile member, generate images of surfaces and their surface properties by scanning them line by line with a sharp tip (Fig. 2.1). In contrast, conventional (far field) microscopes collect radiation, which is transmitted through or reflected from the sample, with an optical system. Their ultimate resolution is limited by the physical diffraction phenomenon to half the wavelength of the light source. Therefore, naturally, light microscopes are approximately limited to a resolution of 200 nm [Winter and Noll, 1998]. (This theoretical resolution limit applies to blue light, which has the shortest wavelength ($\lambda \approx 400$ nm) within the visible spectrum and neglects inevitable adverse effects of optics. A rather realistic and technically achievable limit is 400 nm.)
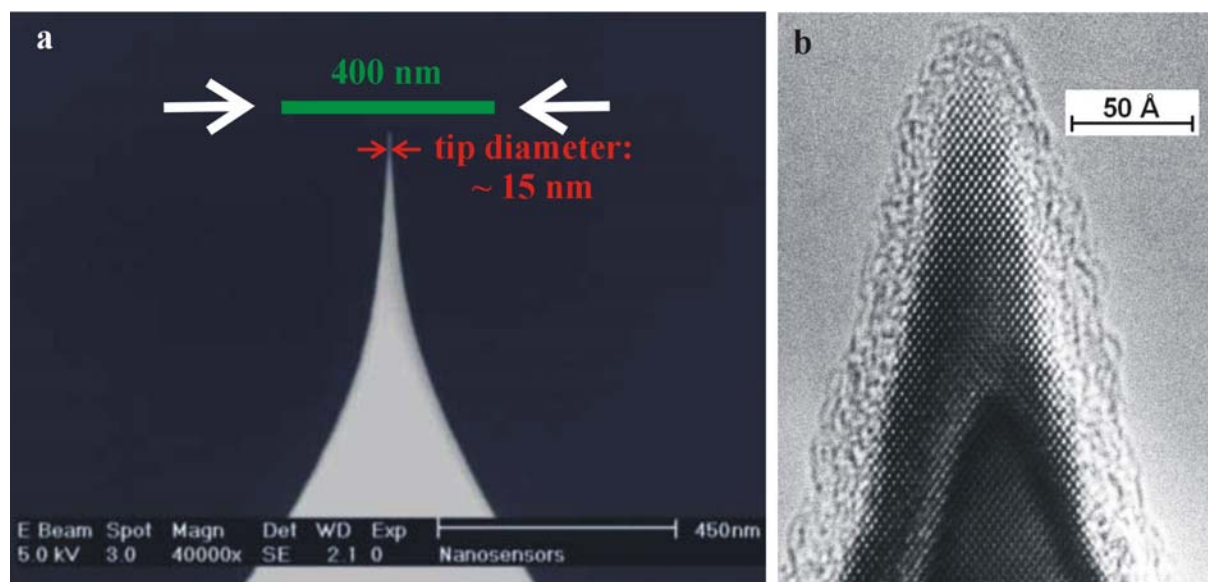


**Figure 2.1** (a) This scanning electron microscope image [Nanosensors™, 2004] of a conventional silicon AFM tip illustrates the resolution power of the AFM in relation to that of a light microscope. The sharp mechanical protrusion is able to access a smaller area than a light microscope is able to focus on. The Abbé diffraction limit restricts the maximum achievable resolution to half the wavelength of the light source. Green light, in the center of the visible spectrum, has a wavelength of 550 nm. Therefore, the theoretical spatial resolution is 275 nm. In

fact, the practical resolution limit (indicated by the green bar) for a high quality instrument is close to 400 nm [Morris et al., 1999]. (b) The transmission electron microscope image represents an extreme close-up of an ultra-sharp silicon AFM tip's apex region [Marcus et al., 1990]. As the native oxide has been etched away with hydrofluoric acid, the 15 nm to 20 nm thick tip-coating is mostly due to hydrocarbons which have been polymerized by the electron beam. The crystal structure appears to remain bulklike up to the apex of the tip [Giessibl, 2003].

Images showing a higher resolution can be obtained by using high energy electrons in an electron microscope (EM). Herein, the velocity of electrons is adjustable to such an extent that wavelengths of about 0.001 nm can be achieved, and therefore the resolving power of an EM increases a thousand times compared to that of the light microscope [Winter and Noll, 1998]. Thus, an entirely new insight into structures of macromolecular scale is disclosed. In spite of all recent improvements in electron microscopy, especially for reaching this high degree of resolution, it is necessary to operate under a pressure of or below $10^{-2}$ Pa. Therefore, biological samples cannot be inspected under physiological conditions. More importantly, biological specimens must be shock frozen, and their surface needs to get vapour-deposited with a conducting carbon or platinum layer [Russel, 2001].

The principle of an SPM is fundamentally different. As intimated earlier on, a stylus which is raster-scanning a surface with sufficient proximity or mechanical contact is used to monitor the changes in the magnitude of the interaction between probe and specimen. Thereby the resolution depends on the sharpness of the tip, the precision with which the probe can be moved over the surface and the sensitivity with which the interactions are detectable. The created image, comprising typically $10^4$ to $10^6$ pixels, which represent one measurement or the mean value of up to three measurements in each case, reflects a degradation of the probe and sample properties [Binnig et al., 1986; Magonov and Whangbo, 1996; Morris et al., 1999]. SPMs are not only capable of depicting surfaces with atomic resolution or even subatomic resolution [Herz et al., 2003; Giessibl et al., 2000] (the latter is still under debate, see [Hug et al., 2001; Giessibl et al., 2001]), but also of achieving a submolecular resolution in aqueous or gaseous milieus [Müller et. al, 2002]. In the case of macromolecules, atomic resolution is only attainable if the predominant number of atoms is in intimate contact with the surface of a flat substrate. Nevertheless, SPMs do allow nanoscale resolution on most biopolymers under natural and physiological conditions. Thus, SPMs offer the resolution power of EMs, but under experimental conditions comparable to those of light microscopy [Morris et al., 1999] (cf. Fig. 2.2).
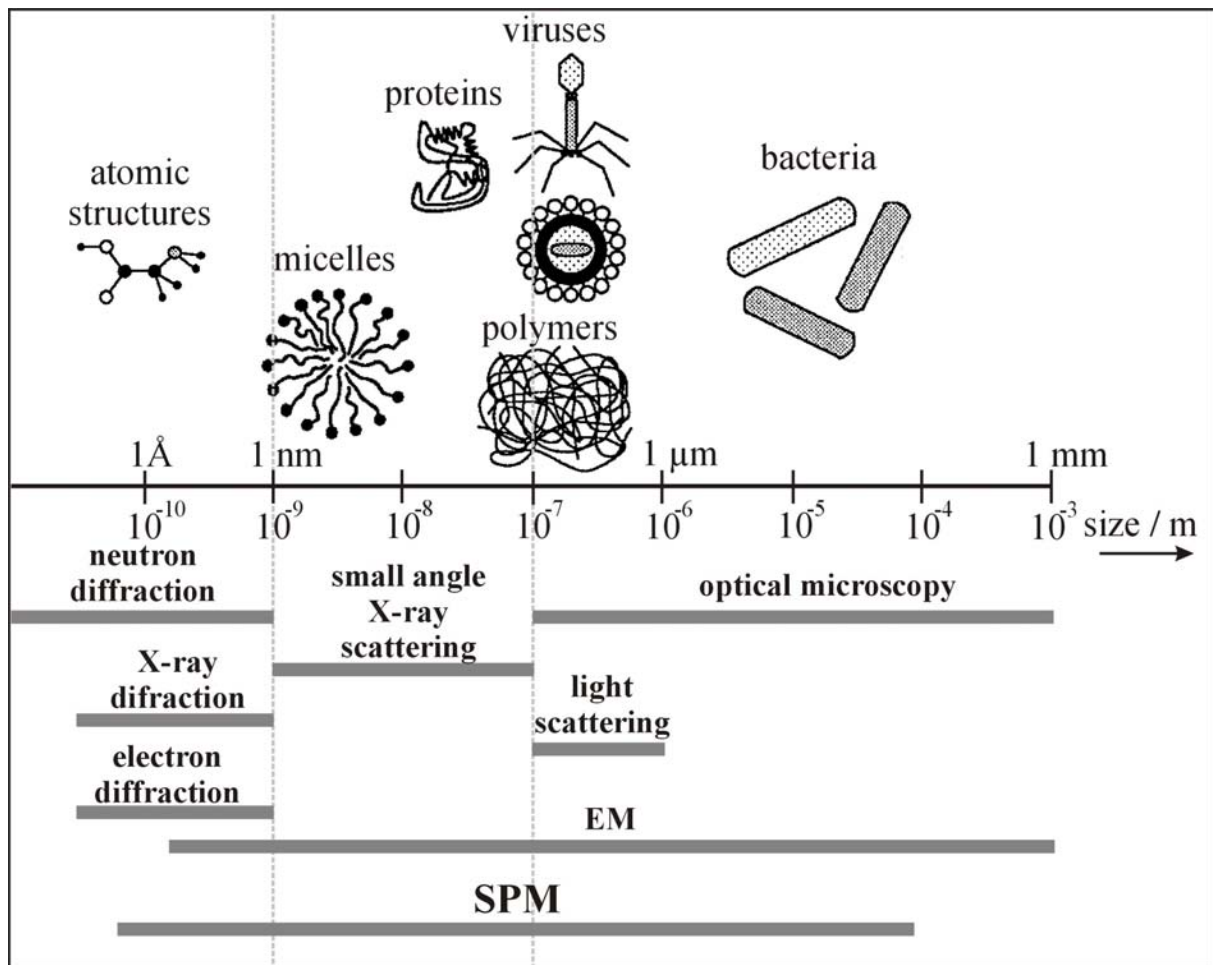
**Figure 2.2** This scheme illustrates the characteristic dimensions of biological and chemical systems in relation to length scales which can be covered by typical structural investigation methods (adapted from [Winter and Noll, 1998]). The whole range from macroscopic over mesoscopic up to microscopic regimes can be structurally analysed (apart from EM) by the diverse SPM techniques.

As any near field interaction is suitable for creating images by SPM, various types of scanning probe methods are applicable for structural investigations. Here, a brief sketch of some relevant methods of the permanently growing scanning probe family is given.

Scanning probe microscopy commenced in 1981 through Gerd Binnig's and Heinrich Rohrer's invention of the scanning tunnelling microscope (STM) at the IBM research laboratory in Zürich [Binnig et al., 1982]. (In 1986 they were awarded the Noble Prize in physics together with Ernst Ruska who developed the EM.) The principle of the STM is based on the quantum-mechanical tunnel effect. The schematic in Fig. 2.3 shows the main features of an STM.
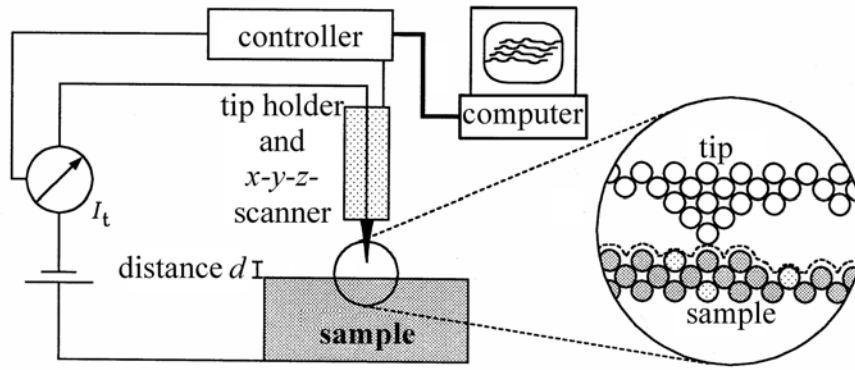
**Figure 2.3** Schematic representation of the main components of a scanning tunneling microscope. The ability to generate real space images of surfaces with atomic resolution depends on the fact that the tunnel current decays exponentially with increasing separation between surface and tip. A change in probe-sample distance of atomic scale leads to a change in the tunneling current of an order of magnitude. Thus, tunneling effectively occurs from the atom on the tip which is nearest the surface of the sample [Winter and Noll, 1998; Morris et al., 1999].

The probe, an ultra sharp metal tip, is moved above the conductive sample surface with spacings of typically 0.1 to 10 nm. If a weak bias voltage of some millivolt to volt is applied between tip and sample, a tunnel current on the nanoampère scale flows in spite of the gap:

$$I_t(d) \propto U_t \cdot e^{-2\kappa(R+d)} \cdot \rho(E_F),$$

(2.1)

where $I_t$ represents the tunnel current, $U_t$ is the applied bias voltage, $R$ is the metal tip radius, $d$ is the tip-sample distance, $\rho$ is the density of state at the Fermi level, $\kappa$ is the electron wave function's inverse fall-off length in vacuum, with

$$\kappa = \sqrt{\frac{2m \cdot \Phi}{\hbar^2}},$$

(2.2)

where $m$ is the free-electron mass, $\hbar$ is the Planck constant devided by $2\pi$, and $\Phi^1$ represents the average tunnel barrier height [Binnig et al., Giessibl, 2003].

Control electronics and piezoceramic actuators, which allow the movement of the tip with ca. 0.01 Å accuracy, maintain this current constant, thus yielding topographic information by the control deviation. In other words, an STM measures a surface with

---

[1] The average tunnel barrier height compares approximately with the arithmetic value of the electronic work function.

constant tunnelling probability. Here, the resolution depends on the sharpness of the tip, the smoothness of the sample and the distance between both of them. Since the tunnelling probability is exponentially related to the tunnelling distance (in vacuum approximately by a factor of ten per Ångström), ideally only one atom at the outmost end of the tip contributes to the tunnelling current. The actual attainable horizontal resolution of 0.01 Å is not reached by any other scanning probe method. Besides, the lateral resolution, mainly determined by the tip profile, is on the order of a few Ångströms. However, the rapid decay in tunnel current restricts investigations to the study of thin interfaces or individual biopolymers. For larger systems, the probe-sample separation becomes too large and any tunnel current would be expected to be too small to be detected. Moreover, the sample surface needs to be conducting or semiconducting, which usually requires the coating of biological samples, so that the main advantage of this SPM method is rather restricted [Winter and Noll, 1998; Wiesendanger and Güntherodt, 1992 and 1993; Bonnel, 1993; Morris et al., 1999].

After technical prerequisites, such as high precision actuators, had become available by the development of the STM, Pohl, Lewis and Fischer [Dunn, 1999; Zhu and Ohtsu, 1999] were able to introduce a near field optical derivative independently of each other in 1984 and 1985, respectively. These scanning near field optical microscopes (SNOM) produce optical contrast on the sample surface with laser light and its invisible evanescent fields[2] on length scales that are below radiation wavelength. Herein, a light source with small aperture (20 nm), which is typically an aluminum coated, off-tapering optical fiber, raster scans the sample surface at a constant distance of 1 to 5 nm (thereby circumventing Abbé's diffraction equation). The transmitted or reflected light is collected by an objective lens and detected from each point of the raster-area with a photomultiplier. Optical images constructed from these data provide a resolution which is only limited by the probe's aperture. Nowadays imaging down to a resolution of 10 nm is feasible. In addition to optical pictures also topographic images can be generated from distance control signals stemming from simultaneously measured tunnel currents or shear forces between tip and probe [Pohl, 1991].

In 1986, the Atomic Force Microscope, also named Scanning Force Microscope, was introduced by Binnig, Quate and Gerber [Binnig et al., 1986] as a modification of the STM. Early STM experiments had shown that significant forces act collaterally with the tunnel current whenever the tip-sample separation is small enough. Thus, these near-field interactions can be used solely to achieve atomically resolved images from surfaces even if they are not conductive. The detection principle of the AFM is based on the deflection of an

---

[2] Fields with decreasing amplitude, although no dissipative mechanisms (e.g. attenuation) take place, are called evanescent.

ultra sharp tip which is mounted at the free end of a cantilever of 100 µm to 200 µm length that reflects a laser beam onto a photodiode. As the tip moves in response of the sample topography during scanning, the reflection angle of the laser beam changes, and so the laser spot falling onto the photodiode moves, producing changes of intensity in each of its four segments. The photocurrent's differential signal between the top and bottom segments contains the topographic information, whereas the orthogonal difference quantifies any lateral or twisting motion of the tip [Tompkins, 1999]. By these means, frictional information can be distinguished from topographic information. In the simplest operating mode, the tip-sample distance is regulated by a feed-back in a way that the cantilever deflection (i.e. probed interaction) remains constant during a scan. The resulting control signal is recorded as a function of the lateral tip position and converted into a false color image wherein the color graduation reflects the extent of vertical displacement [Morris et al., 1999].
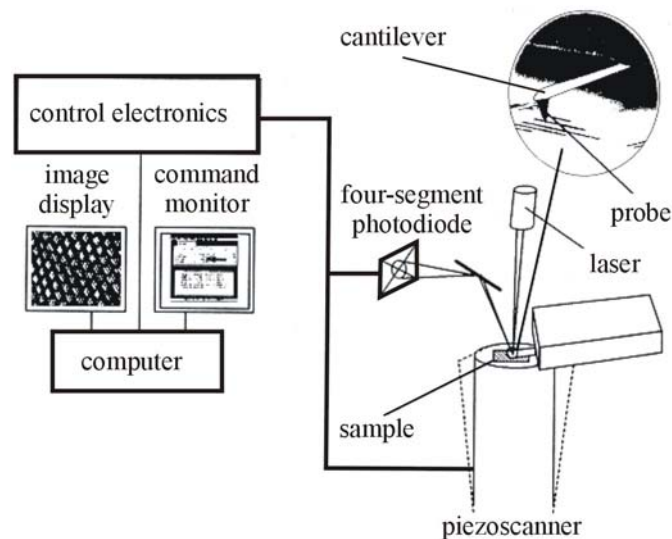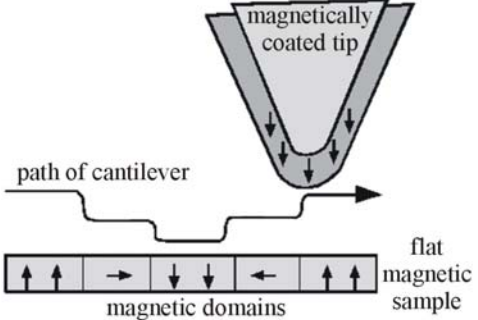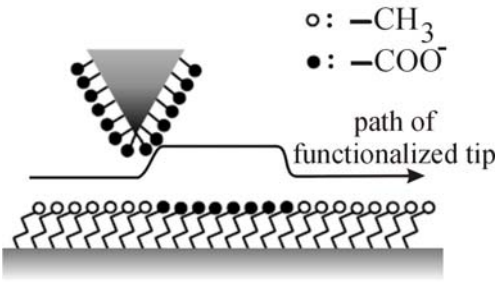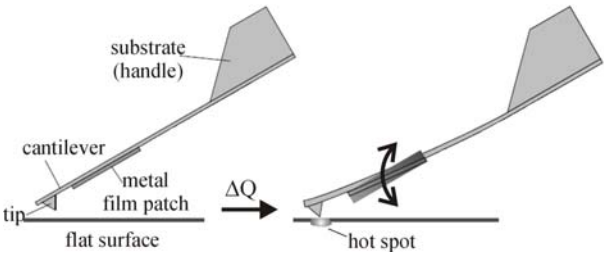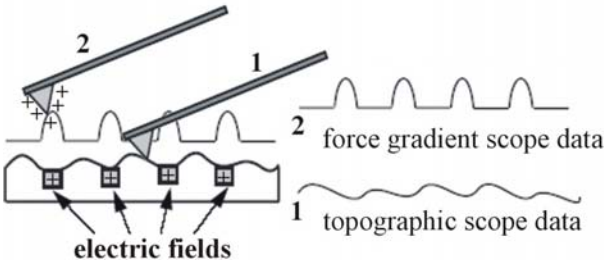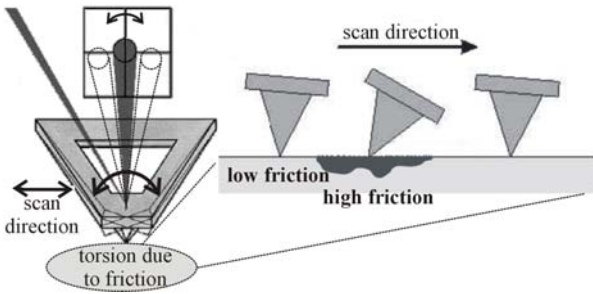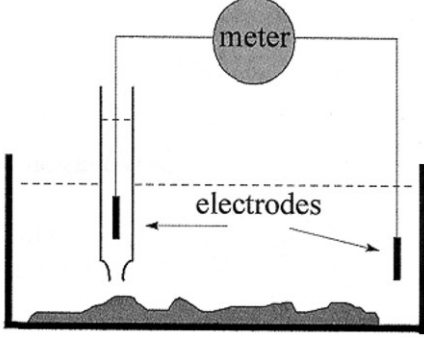
**Figure 2.4** Scheme of the main components of an atomic force microscope. This device incorporates an electronic unit and a computer station equipped with image and command monitors. The microscope itself includes a piezoscanner, a probe and a laser beam deflection system (adapted from [Margonov and Whangbo, 1996]).

The AFM not only provides the ability of in situ atomic scale imaging of sample surfaces, but is also suitable for displaying a wide spectrum of spatially resolved physical and chemical surface properties (including elastic moduli, electric conductivities, thermal properties and magneto-static forces). Each kind of property to be examined requires an appropriate probe. Table 2.1 lists several instrument types which are relevant to the progressive fields in nanotechnology and nanostructural science like electronics, informatics, robotics, surface science, optics and also medicine and biotechnology [Bundesministerium für Bildung und Forschung, 2002].

**Table 2.1** Listing of some further developments in scanning probe microscopy.

| Instrument type: | Description: |
| --- | --- |
| Magnetic Force Microscope (MFM)<br> | - Visualizes the spatial variation of magnetic forces on a sample surface by means of a tip coated with a ferromagnetic film.<br>- Mainly used in development and quality control of magnetic storage devices. |
| Chemical Force Microscope (CFM)<br> | - Chemically functionalized probes make distinguishable the interactions between particular functional groups.<br>- Enables the local determination of surface energies, pK-values and adhesive forces [Janshoff et al., 2000]. |
| Scanning Thermal Microscope (SThM)<br> | - A thermal probe with an integrated thermistor and/or bimetallic cantilever makes it possible to record spatially resolved temperature-images.<br>- Extra heatable probes provide information about local thermal transfers, thermal conductivities, rates of heat flow, etc. |
| Electrostatic Force Microscope (EFM)<br> | - With a voltage applied between tip and sample the tip hovers above the surface and deflects when it scans over static charges.<br>- Visualizes the capacitive properties of semiconductive surfaces and makes it possible to map electron concentrations in integrated circuits. EFM is a valuable tool for testing microprocessor chips at work. |

| Lateral Force Microscope (LFM) | - Identifies and maps friction resistances of surfaces through monitored cantilever torsion perpendicular to scan direction. |
| --- | --- |
| Scanning Ion Conductance Microscope (SICM) | - Records in electrolytic solution local variations in ion-flow by raster scanning a half-cell with small aperture close to sample surface.<br>- E. g., SCIMs can be used to provide electrophysiological data on biological systems like ionic currents through membrane pores. |

In addition, the AFM is a versatile tool for recording so called "force-distance-curves", in which the cantilever deflection is plotted during a whole engaging and retracting cycle of the tip as a function of the relative position from the sample surface (Fig. 2.5).
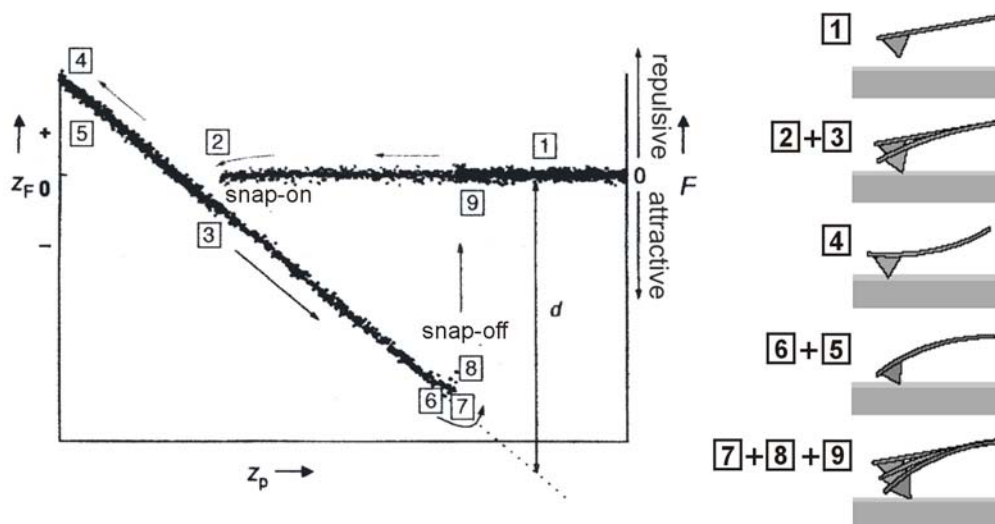
**Figure 2.5** Schematic plot of a force-distance-curve ($z_F$: cantilever deflection, $z_P$: vertical scanner displacement, $d$: tip-sample distance, $F$: force-gradient calculated from cantilever deflection); numbers and arrows illustrate the progress of a measurement: 1) Large tip-sample separation. Probing-tip approaches surface slowly. 2) Incipient attractive surface forces. 3) Tip abruptly gets in contact with sample surface. 4) Cantilever bends as the tip is even pushed closer to the surface. 5)-6) Tip is now retracted. Repulsive forces decrease. 7) Maximum of adhesive force. 8)-9) Abrupt tip surface separation [Janshoff et al., 2000].

Herein, the possible use of an AFM extends from indentation measurements with elastomers or thin organic layers over mechanical experiments on single macromolecules up to living cells. On the basis of the force-distance curves, a wealth of information related to the mechanics of single molecules can be achieved, such as conformational transitions, flexural moduli, bonding forces, rate constants and even information about potential shapes [Janshoff et al., 2000]. Fig. 2.6 exemplifies how single-molecule force spectroscopy opens up detailed insight into the mechanical properties of individual proteins at the level of single tertiary-structure elements.
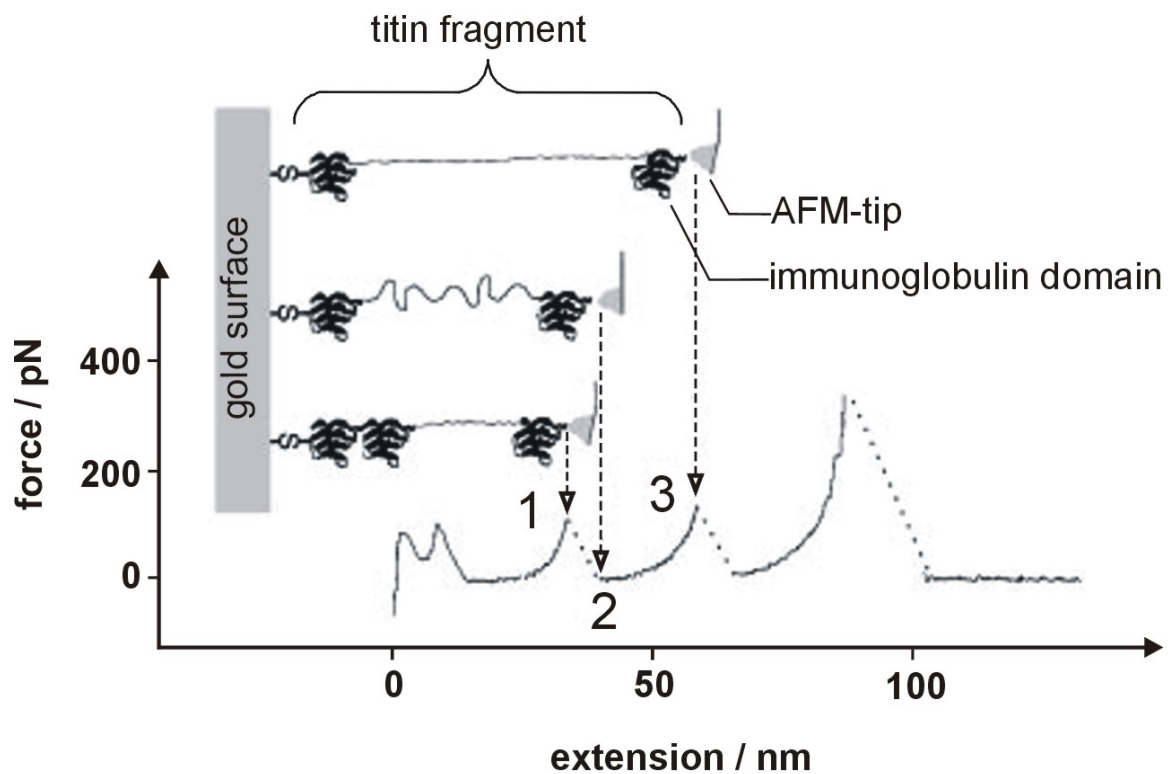


**Figure 2.6** AFM-stretching experiment with a titin fragment spanning four immunoglobulin (Ig) domains. The protein is covalently attached to a gold surface (cysteine, which is added to the C-terminal end, provides the covalent sulphur anchor) and picked up by adsorption to an AFM tip. Retracting the tip leads to a sequential unfolding of Ig domains which are mechanically in series. Resulting from this, a typical sawtooth pattern in the force extension plot is obtained. Before a domain unfolds, the extended polypeptide will be stretched until a maximum holding force is reached (1) and unfolding becomes highly probable. Unfolding of an Ig domain abruptly reduces the holding force (2) due to an increase in length of the extended polypeptide. Continued retraction of the AFM-tip again stretches the extended polypeptide until a force is reached (3), where the next domain unfolds. Doing so, the cantilever snaps back into its resting position and produces a black window in the force curve (dotted line) without any information about the unfolding process. The last peak in this recording is usually much higher than the preceding peaks and does not reflect the unravelling of a domain but the detachment from the tip [Rief et al., 1997].

### 2.1.1  Equipment

Comprising an optical block (resp. AFM head), a piezoceramic scanner and a base, which are the main components of the microscope itself, the AFM furthermore consists of a controller and a computer that monitors the tip-sample approach, records the strength of the probing interaction as a function of the tip position and converts the collected data into an image on the screen. For ultra high resolution images an additional vibration dumping system is required to prevent any small displacement of the tip or the sample. According to the prevailing environmental conditions the efforts to be made can be extremely different. In general, mounting the microscope on a sorbothane™ mat will be a sufficient way to shield from typical building vibrations (15 - 20 Hz). But an active piezoceramic vibration isolation system, filtering frequencies from 0.6 - 100 Hz [Halcyonics, 2002] and damping all six translational and rotational modes, is a much more reliable tool to provide the necessary isolation [Morris et al., 1999; Magonov and Whangbo, 1996].
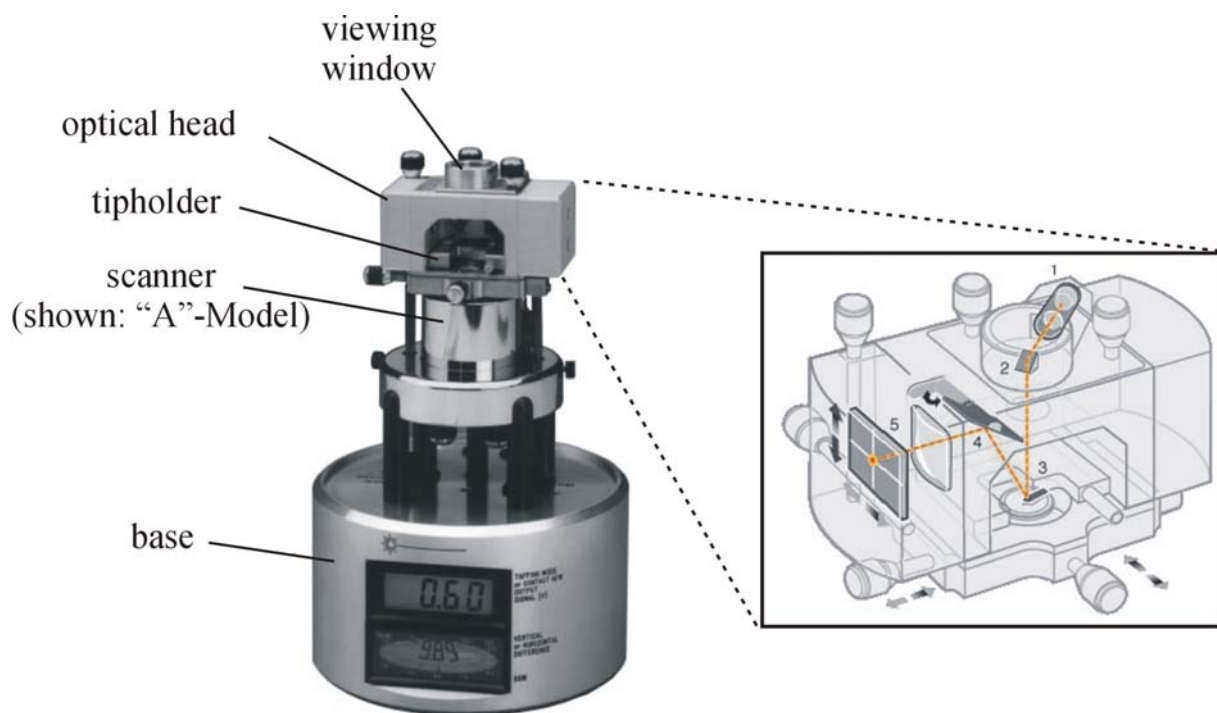


**Figure 2.7** The heart of the AFM is the microscope itself, consisting of three main components: I) The head with its optical cantilever detection system (see graphical inset: 1. laser, 2. mirror, 3. cantilever and underneath the sample-disk (mounted on top of the scanner tube), 4. tilt mirror, 5. four-membered photodetector), which measures the cantilever deflection during a scan. II) The piezoelectric scanner-tubus moves the sample in the three orthogonal directions x, y and z with picometer accuracy. III) The microscope base includes a stepper motor for coarse vertical sample positioning and diverse voltage meters displaying several photodetector output signals, which refer to deflection voltage, signal amplitude and sum signal, needed for a correct optical adjustment. Adapted from [Tompkins, 1999]. (A complete AFM-setup is shown in the Appendix.)

The AFM head contains the entire optical set for detecting the cantilever deflection, which consists of a laser diode (emitting a maximum 1.0 mW beam at 670 nm [Tompkins, 1999]), diverse laser beam deflectors and a four-quadrant positional photodetector. An optical microscope camera attached to a viewing window at the top of the head allows one to observe the cantilever for alignment of the laser beam and for positioning the tip over the sample areas of interest. The core of the AFM head comprises the cantilever holder with the tip positioned over the sample (which in turn is magnetically attached on top of the scanner tube). For exciting the cantilever oscillation in tapping-mode AFM, a small piezoelectric crystal is embedded inside the cantilever holder.

The central element of a force microscope - contributing to surface imaging and being the major instrumental difference compared to an STM - is the flexible cantilever, 100 - 500 μm long and 0.5 - 5 μm thick, with the tip integrated at its free end. In principle this is nothing but a spring leaf, sensing the force between tip and sample. The force contribution $F$ from the bending of the cantilever which acts on the sample in case of direct mechanical contact is determined by the following equation known as Hooke's law:

$$F = -k \cdot d \, ,\tag{2.3}$$

where $k$ is the force constant or stiffness of the cantilever and $d$ is its displacement. For application in AFM these probes need to have specific properties. For sensing normal tip-sample forces, the force sensor should be rigid in two axes and relatively soft in the third axis. Therefore common cantilevers are either rectangular or "V"-shaped.

For a rectangular cantilever, which was used exclusively in this study, the spring constant is expressed as [Chen, 1993]

$$k = \frac{Y \cdot w \cdot t^3}{4L^3} \, ,\tag{2.4}$$

where $Y$ is the elasticity (or Young's) modulus, and $w$, $L$, and $t$ are the width, length, and thickness of the cantilever, respectively. Typically, the elastic spring constants vary in the 0.01 - 50 N/m range and, as the occurring tip-sample interactions are on the order of nN [Israelachvili, 1994], ensure a detectable cantilever deflection. On the other hand, very small spring constants run the risk of a "snap in" of the tip onto the sample surface if the tip sample separation is sufficiently small [Israelachvili, 1994]. In general, cantilevers of small stiffness

are most suitable for imaging soft materials (intermolecular force constants of biological samples can be as small as 0.1 N/m; for solids they usually range from 10 N/m to 100 N/m [Giessibl, 2003]), while rigid cantilevers are needed for dynamic-mode AFM measurements (low noise instability) and for probing nanomechanical properties of sample surfaces [Magonov and Whangbo, 1996].
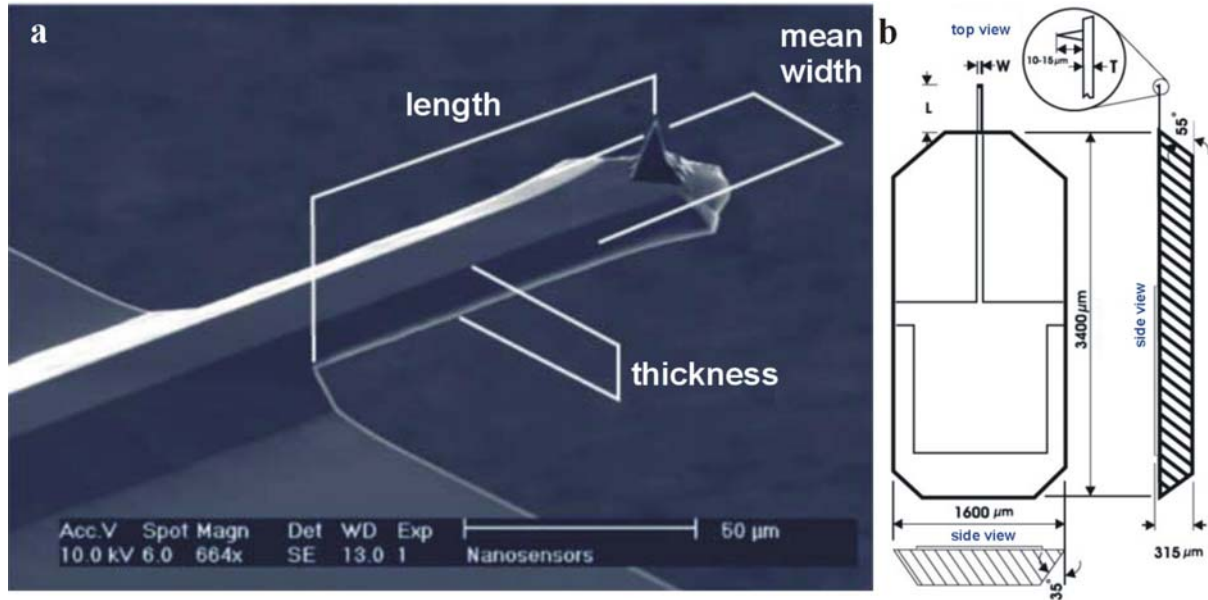


**Figure 2.8** (a) SEM micrograph of a silicon PPP-NCHR AFM-probe from Nanosensors™ which has been used in this study [Nanosensors™, 2004]. The AFM-probe consists of three elements: I) The tip, which here is shaped like a polygon-based pyramid with a height of 10 - 15 µm and a half cone angle smaller than 10° at the apex, is mounted on the free end of the cantilever. Ensuring high resolution images, the tip radius of curvature is typically ≤ 5 nm. II) Taking up the forces which are acting on the tip, the cantilever (or more precisely, its free end) bends like a spring leaf so that its deflection can be measured and converted into topographical information. The cantilever geometry is 125 µm in length, 30 µm in width and 4 µm in thickness. Further, the spring constant of this model is $k = 42$ N/m and the resonance frequency is $f_0 \approx 300$ kHz. III) The silicon holder (or probe substrate), which partly can be seen in the bottom left of the EM picture and is sketched in (b) [Nanosensors™, 2004], is an integral part of the probe and designed for manipulating and fixing it to the AFM.

The fundamental eigenfrequency $f_0$, which is also a property of interest, can be written as [Chen, 1993]

$$f_0 = 0.162 \frac{t}{L^2} \sqrt{\frac{Y}{\rho}} \ , \tag{2.5}$$

where $\rho$ is the density of the cantilever material. Here, the cantilever resonant frequency should be at least ten times higher than the typical acoustic noise and resonance spectrum

produced by the microscope (and environment). However, low force constant cantilevers have the disadvantage of low resonant frequencies (7 - 9 Hz) which makes them less stable and more difficult to use if scan conditions are not chosen carefully [Morris et al., 1999]. A useful measure for cantilever characterization is its quality factor $Q$, which depends on the damping mechanisms present in the lever. The $Q$ factor reflects the ratio between the energy of vibrational motion $E_v$ (multiplied by $2\pi$) and the energy loss $\Delta E_v$ of the lever during one period. Within a good approximation, this corresponds to the ratio between the lever resonance frequency $f_0$ and the half-height peak width $\Delta f$ of the resonance curve and is given by [Rao, 1995]

$$Q = \frac{2\pi \cdot E_v}{\Delta E_v} \approx \frac{f_0}{\Delta f} \ .$$

$(2.6)$

The higher the cantilever's quality (with given resonance frequency), the sharper the resonance curve will be. This effects an increase in the amplitude and phase signal sensitivity in dynamic-mode AFM (according to external forces) [San Paulo and García, 2001; Sulchek et al., 2000; Rodríguez and García, 2003]. For micro-machined cantilevers operated in air, $Q$ is mainly limited by viscous drag and usually runs up to a magnitude of $10^2$ - $10^3$, while in vacuum, internal and surface effects of the cantilever material cause damping, and $Q$ reaches values on the order of $10^5$ [Giessibl, 2003]. Especially for dynamic-mode AFM, a further requirement for cantilevers is important: utmost frequency stability over time and temperature changes [Giessibl, 2003].

These mechanical requirements mentioned above are fulfilled by photolithographically produced silicon nitride ($Si_3N_4$) and silicon cantilevers. Due to this manufacturing process, analogous to highly integrated circuits, it is possible to produce hundreds of cantilevers with integrated tips from a single silicon-wafer, whose spring constants and resonance frequencies hardly vary. In order to achieve atomic resolution, the front atom of the tip should ideally be the only one interacting strongly with the sample. It becomes evident that the tip radius should be as small as possible to reduce forces caused by the shaft of the tip. Sharp tips (integrated on a cantilever) are built from all-silicon, as chemically etching preferentially develops sharp-edged peaks in this material, provoked by anisotropic etching rates of silicon and silicon dioxide. The single crystal silicon tip (the whole wafer is a single crystal) of the most common cantilevers used today points in the <100> direction, so that the front atom has only two bounds to the rest of the tip and is

separated sufficiently from the adjacent Si-atoms (see appendix, Fig. 7.5) [Magonov and Whangbo, 1999; Giessibl, 2003; Nanosensors™, 2004].
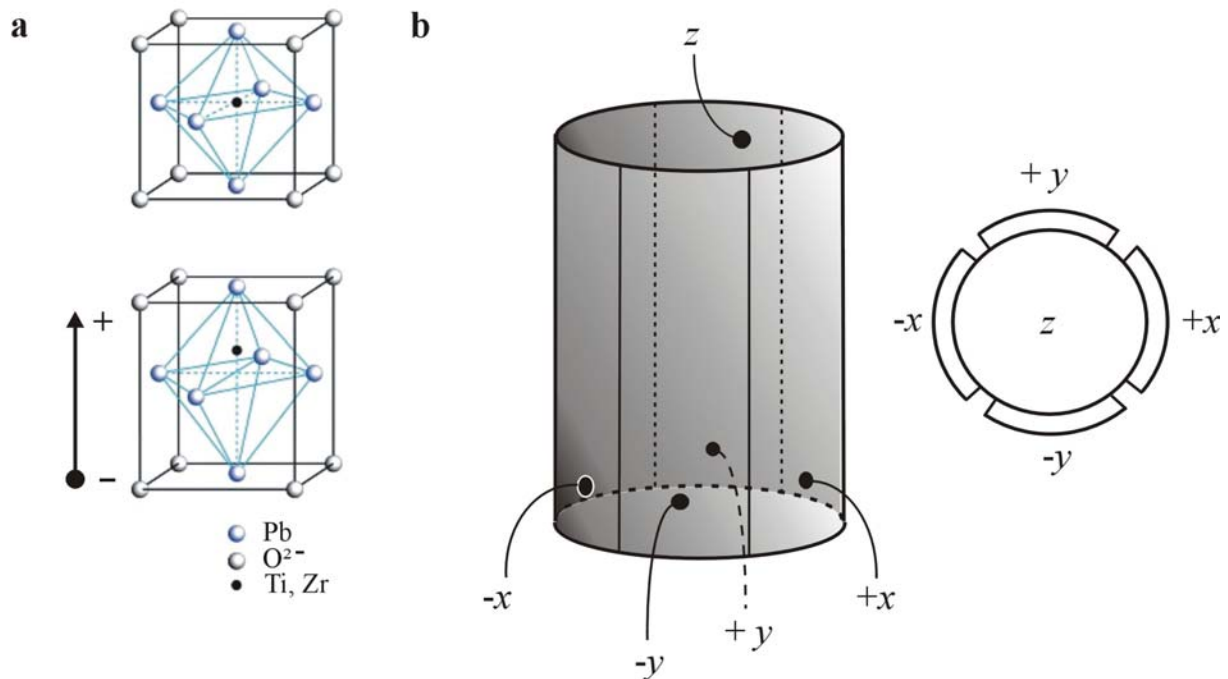


**Figure 2.9** (a) PZT unit cell: The upper graphic represents a Perovskite-type lead zirconate titanate (PZT) unit cell with cubic symmetry. On the other hand, the lower graphic displays a tetragonally distorted unit cell under applied voltage [Physik Instrumente, 2004]. Thus, in the poled piezoelectric material, the ions in the unit cells are shifted and, additionally, dipolar domains (here not shown) change their degree of alignment. The result is a corresponding change of the dimensions (expansion or contraction) of the PZT material. (b) Schematic representation of a piezoelectric tubular scanner (adapted from [Morris et al., 1999]), which consists of thin-walled piezoelectric ceramic and is split into quarters parallel to its long axis. The scanner tube expands or contracts vertically when a voltage is applied between the inner and all outer electrodes ($z$, $+x$, $-x$, $+y$, $-y$). A signal applied to one of the outer electrodes ($+x$, $-x$, $+y$, $-y$) provokes a corresponding horizontal bending.

By means of a tubular piezoceramic actuator, commonly called "scanner", the sample's three-dimensional driving motion beneath the cantilever is performed with an accuracy of one picometer. The reverse piezoelectric effect is based on the phenomenon, that the ions in the unit cells are shifted and, additionally, the dipolar domains change their degree of alignment when a bias voltage is applied to the poled piezoelectric material. Consequently, the dimensions (expansion, contraction) of the material change correspondingly. The scanner tube consists of thin-walled PZT (lead zirconate titanate) ceramic which is polarised radially. As shown in Fig. 2.9(b), five electrodes are attached to the internal and external faces of the tube, with the external face divided up into four segments parallel to the long axis. By applying a voltage between the inner and all outer electrodes, the scanner tube will move

vertically, whereas the tube bends in *x* or *y* directions if a voltage is only applied to one of the outer electrodes. Any arbitrary lateral motion is provoked by steering the outer electrodes simultaneously with different voltages, so that a combination with the inner electrode enables any spatial movement [Morris et al., 1999; Taylor, 1993].

### 2.1.2   Tip-Sample Interactions

Several forces between tip and sample contribute to the bending of an AFM cantilever. Commonly, they are divided in short range and long range forces. Interactions between atoms are often described on the basis of atom-atom pair potentials such as the Lennard-Jones potential [Magonov and Whangbo, 1996; Israelachvili, 1994; Czeslik et al., 2001]:

$$V_{Lennard-Jones}(r) = 4\varepsilon \left[ \left( \frac{r_0}{r} \right)^{12} - \left( \frac{r_0}{r} \right)^6 \right],$$

(2.7)

where *r* represents the distance between pairs of atoms and $\varepsilon$ the minimum energy at $r = 2^{1/6}r_0$. For $r = r_0$, the potential energy is zero. Strongly repulsive at short distances due to the Pauli exclusion principle and slightly attractive at a longer distance, the short range repulsive interaction is more indicative according to very small changes in the tip-sample separation. The atomic-scale image contrast originates from the variation of the tip-sample repulsive force and therefore contains local information due to the short range character of this force. Consequently, a steep force-distance relationship provides the basis for high-resolution surface imaging in AFM.

Starting with a tip-sample separation of ca. 1 nm, the van der Waals (VDW) attractive interaction caused by fluctuations in the electric dipole moment of atoms and their mutual polarisation exerts its influence between sample and tip-atoms [Giessibl, 2003]. Calculated by the Hamaker approach [Hamaker, 1937], the van der Waals potential for a spherical tip with radius *R* next to a flat surface, where *z* is the distance between the plane connecting the centers of the surface atoms and the center of the closest tip atom, is given by [Israelachvili, 1994]

$$V_{VDW} = -\frac{A_H \cdot R}{6z}.$$

(2.8)

Thus, the van der Waals force for spherical tips is proportional to $1/z^2$, while for pyramidal and conical tips, a $1/z$ force dependence holds true [Giessibl, 1997]. The Hamaker constant $A_H$ depends on the atomic polarizability and density of the tip and sample material. Relevant to AFM, the magnitude of the van der Waals forces for the tip-sample system is estimated to be in the 1 - 20 nN range [Goodman and Garcia, 1991]. As bodies at separations well beyond the chemical bonding distances experience van der Waals interactions (even at distances in the 50 - 100 nm range [Magonov and Whangbo, 1996]), they are ranked among the long distance forces. In vacuum, van der Waals forces are major disturbances in force microscopy, apart from electrostatic forces.

Due to liquid contamination layers on tip and sample (consisting of water or hydrocarbons), which are omnipresent under ambient conditions [Müller et al., 1997], a meniscus between tip apex and sample is formed. Estimated to be in the range of 10 - 100 nN, attractive capillary forces are effective up to 10 - 200 nm [Magonov and Whangbo, 1996]. Unfortunately, the meniscus around the tip apex spreads the tip-sample interaction area and therefore gives rise to deterioration in resolution. At worst, the tip can get stuck to the sample surface or, if the overall imaging force had to be adapted to these adverse conditions, delicate samples could be damaged or moved over the substrate.

Although in this study no aqueous AFM investigations were conducted, they are nevertheless important in to many biological applications of AFM. Considering that in water many surfaces are charged, either due to dissociation of surface groups or adsorption of ions onto the surface, electrostatic forces acting between tip and sample have also to be mentioned for the sake of completeness as they could get strong enough to interfere with imaging [Müller et al., 1999]. The surface charge is balanced by dissolved counterions. Attracted back to the surface by the electric field, but likewise spread away from the surface to increase the entropy, these ions form a diffuse layer. The ensemble of the counterions and the charged surface is named electric double-layer [Butt et al., 1995]. With respect to Boltzmann's law, the counterion concentration decreases exponentially with the distance from the surface. This decay is characterized by the Debye length

$$\lambda_D = \sqrt{\frac{\varepsilon_0 \varepsilon_e kT}{e^2 \sum_i c_i q_i^2}} \ , \tag{2.9}$$

where $k$ is the Boltzmann constant, $T$ is the absolute temperature, $e$ is the unit charge, $\varepsilon_0$ is the permittivity of the vacuum, and $\varepsilon_e$ is the dielectric constant of the medium, in this case water.

The Debye length is determined by the ionic valency $q_i$ and the concentration $c_i$ of the ith electrolyte component of the liquid and can be interpreted as the thickness of the diffuse electrical double-layer [Israelachvili, 1994; Butt et al. 1995; Müller et al., 1999].

An electrostatic interaction arises when the electrical double-layers of tip and sample perturb each other, which occurs at a separation of a few tens of a nanometer [Müller et al., 1999]. (E.g., in case of identically charged surfaces, the concentration of ions between tip and sample increases and results in a repulsive force.)

The electrostatic force between a spherical tip and a flat surface (the shape and the surface properties of both the AFM tip and the sample define the electrostatic double-layer interaction, depending on the surface charge density) is given by

$$F_{el}(z) = \frac{4\pi \cdot R \cdot \sigma_s \cdot \sigma_t \cdot \lambda_D}{\varepsilon_0 \cdot \varepsilon_e} \cdot e^{-z/\lambda_D}, \qquad (2.10)$$

where $z$ is the distance between the two surfaces, $R$ is the tip radius, and $\sigma_s$ and $\sigma_t$ are the surface charge densities of sample and tip [Müller et al., 1999], respectively. Increasing with the surface charge density and decreasing roughly exponentially with the distance, $F_{el}$ can be affected by the electrolyte concentration and pH of the buffer solution. Thus, the distance-dependent interaction between tip and sample can be tuned via the electrolyte to be repulsive or attractive [Butt, 1991a, b; Ducker, 1991]. Additionally, the range of the double-layer forces, which decay exponentially with the distance, can be controlled by the salt concentration according to Eq. (2.9) [Butt et al., 1995; Müller et al., 1999]. Finally, it has to be mentioned that in case of repulsive electrostatic tip-sample interactions, the external force applied to bring the tip in contact with the sample surface, should overcome this electrostatic force. Otherwise, what is imaged reflects the surface charge distribution rather than the sample topography [Magonov and Whangbo, 1996; Senden et al., 1994].

fluid film damping
(ca. 10 μm)

electrostatic forces,
attractive or repulsive
(up to 1 μm)

capillary forces,
attractive
(10 - 200 nm)

van der Waals forces,
attractive
(up to 100 nm)

repulsive force due to
the Pauli principle
(fractions of an Ångström)

surface plane
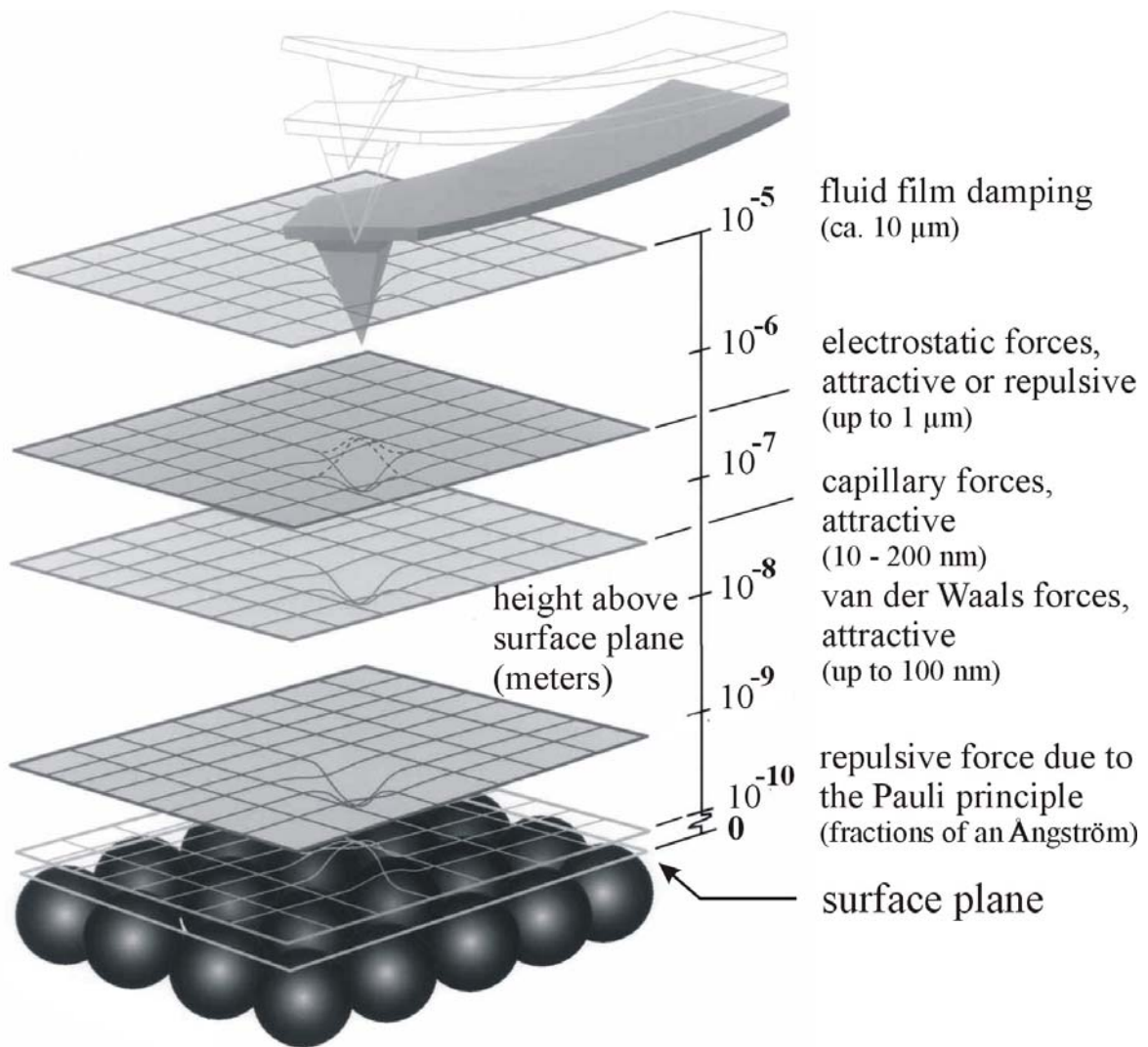
**Figure 2.10** This graphic illustrates different forces encountered by an AFM probe as it approaches the sample surface (adapted from [Farley, 1999]). The film damping phenomenon is exclusive to oscillating probes. A damping air film is developed when an oscillating probe comes within 10 μm of the sample surface. At this distance, either the air is squeezed between probe and surface during the downstroke or a partial vacuum is created due to the upward rebounding of the probe, so that the resulting pumping effect dampens probe motion. (This phenomenon disappears after the probe is lowered down to the surface) [Farley, 1999].

### 2.1.3   Operating Modes

The great spectrum of operating modes in AFM can basically be divided into two categories, underlying a statically or dynamically bending of the cantilever. Within the scope of this work, the description will be restricted to three important modes, of which the first represents a static operating mode while the other two dynamic modes were the ones to be applied in this study.

The fundamental mode is the so-called contact mode where the AFM tip is brought into permanent mechanical contact with the sample surface. (Thus, imaging is performed in a repulsive regime dominated by the short range interactions due to the Pauli exclusion principle.) By means of a feedback control, the static bending and deflection of the cantilever and therefore the translated force on the sample surface is kept constant at a setpoint chosen by the operator. The *z*-signal reflecting the vertical movement of the scanner to correct the position of the sample beneath the tip is used to achieve the topographic information during a raster scan (height image). Oppositely, it is possible to maintain the vertical position of the sample constant, so that the deflection signal of the cantilever can be converted into height information (deflection image).

Under appropriate conditions, i.e. high vacuum, ultra sharp tips and smooth, rigid samples, contact mode is the operating method which leads to the best resolutions achievable in AFM. Contact mode AFM (CMAFM) measurements can provide topographic information with vertical resolutions < 0.5 Å and lateral resolutions up to 0.5 nm [Strausser et al., 1994; Engel et al, 1997]. However, there are some fundamental disadvantages which have to be accepted. Although during a raster scan only small bearing forces between 0.1 and 100 nN [Magonov and Whangbo, 1996] are exerted by the apex of the tip onto the sample surface, a distortion, lesion or even detachment of a soft and delicate sample from the substrate cannot be excluded. Lateral forces, like shear and friction forces, which are inevitably applied to the sample (while the tip slides across the surface) and which can even be amplified by the omnipresent tip-sample meniscus under ambient conditions, are the major problems [Magonov and Whangbo, 1996]. In that respect, contact mode imaging proved to be less suitable for weakly fixed structures, as single macromolecules are often pushed away by the AFM stylus [Karrasch et al., 1993]. Thus, diverse macromolecules have been observed [Radmacher et al., 1994; Martin et al., 1995; Kasas et al., 1997; Shlyakhtenko et al., 1998] that could not be imaged with CMAFM but with a more gentle AFM procedure which is described next [Möller et al., 1999].

In tapping mode atomic force microscopy (TMAFM), the cantilever oscillates vertically at its resonance frequency (or close to its resonance value) with a free oscillation amplitude ranging between 1 to 100 nm [San Paulo and García, 2001; Möller et al., 1999]. Approaching the sample surface, the vibrating tip extends into the repulsive regime during a part of the oscillation, so that the tip intermittently touches or "taps" the surface at the end of its downward movement. Thereby the vibrational amplitude is damped for a little amount. This drop of the amplitude is used as a feedback signal for surface height tracking. The

resulting height data correspond to the change in piezo height needed to keep the vibrational amplitude of the cantilever constant. Compared to CMAFM, this imaging mode has the advantage that friction forces applied to the surface are greatly reduced, and the short tip-sample contact time prevents inelastic surface modifications [Magonov and Whangbo, 1996; Möller et al., 1999]. Thus, it becomes evident that TMAFM is especially suitable for soft and weakly attached samples, such as biological macromolecules.

Originally introduced for ambient-condition experiments, TMAFM should enable the tip to penetrate through the contamination overlayer, which (often) causes artefacts and involves the risk of broken cantilevers in contact mode (as the tip could get stuck to the surface). The energy delivered to the sample from the tip is determined by the amplitude of the free vibration ($A_0$) and the set-point drop ($\Delta A$) in the amplitude. Therefore, small values should be chosen for the $A_0$ and $\Delta A$ parameters to examine soft materials or to achieve high resolution images. Unfortunately, under ambient conditions, the reduction of these parameters is limited by the contamination overlayer. For this reason, the utilization of only freshly prepared samples with a negligible contamination film becomes evident.

An alternative signal to be recorded in TMAFM is the phase shift of the cantilever oscillation relative to the driving signal as a reference. This phase imaging is based on the fact that the tip not only provokes a modification in amplitude, when it strikes the sample surface, but also a lag in phase as a consequence of the energy dissipated in the tip-sample contact [Cleveland et al., 1998]. The amount of energy loss is dependent on the local elastic properties of the sample so that this imaging mode can be applied to explore surfaces with heterogeneous viscoelastic and adhesion material features [Stark et al., 2001]. A model suggested from Magonov et al. [Magonov et al., 1997] allows the interpretation of the phase contrast. Taking a freely oscillating cantilever as a starting point, characterized by the spring constant $k$, mass $m$, quality factor $Q$ and the resonance frequency $f_0$ (or resonant angular frequency $\omega_0$) of the lever, which again is related to $k$ and $m$ as [Rao, 1995]

$$k = 4\pi \cdot m \cdot f_0^2 = m \cdot \omega_0^2 \,, \tag{2.11}$$

the phase angle $\phi$ of free cantilever oscillation is

$$\phi = \arctan\left( \frac{m \cdot \omega \cdot \omega_0}{Q \cdot \left(k - m \cdot \omega^2\right)} \right), \tag{2.12}$$

where $\omega$ is the vibrational frequency. The phase angle varies sharply around $\omega_0$ as a function of $\omega$. At $\omega = \omega_0$, $\phi$ is $\pi/2$, smaller than $\pi/2$ for $\omega < \omega_0$, and larger than $\pi/2$ for $\omega > \omega_0$. In the case of dominating repulsive tip-sample forces (after bringing the oscillating cantilever close to the sample), the frequency is shifted to larger values, and as a consequence, the phase angle curve follows this shift so that $\phi_0$ (i.e., $\phi$ at $\omega_0$) becomes smaller than $\pi/2$ [Whangbo et al., 1998; Magonov et al., 1997].

To a first approximation, the force constant of the cantilever is changed by the tip-sample interactions to a new effective value

$$k_{\text{eff}} = k + \sigma \, ,\qquad\qquad(2.13)$$

where $\sigma$ represents the sum of the force derivatives for all forces $F_i$ acting on the cantilever

$$\sigma = \sum_i \frac{\partial F_i}{\partial z} \, .\qquad\qquad(2.14)$$

The relative tip-sample displacement is represented by $z$. Provided, $\sigma$ is very small in magnitude compared to $k$, the phase angle is given by

$$\phi = \arctan\left( \frac{m \cdot \omega \cdot \omega_0}{Q\left(k + \sigma - m \cdot \omega^2\right)} \right) ,\qquad\qquad(2.15)$$

and

$$\phi(\omega_0) = \phi_0 = \arctan\left( \frac{k}{Q \cdot \sigma} \right) .\qquad\qquad(2.16)$$

Therefore, the phase shift angle $\Delta\phi_0$ between free and interacting tip is obtained by

$$\Delta\phi_0 = \frac{\pi}{2} - \arctan\left( \frac{k}{Q \cdot \sigma} \right) \approx \frac{Q \cdot \sigma}{k} \, .\qquad\qquad(2.17)$$

This approximation holds when $\sigma$ is much smaller than $k$.

The sign of the phase shift coincides with that of the overall force derivative $\sigma$, i.e., the phase shift is positive in case of dominating repulsive forces and negative in the adhesive regime.

The magnitude and duration of the tip-sample repulsive force essentially depend on the stiffness of the tip and sample [Sarid et al., 1996]. Assuming that a spherical tip and a plane surface under force *F* leads to a circular contact area of radius *a* and indentation depth *d*, the relation between surface stiffness *S* and effective Young's modulus $Y^*$ can be written as [Pethica and Oliver, 1987]

$$S = \frac{\partial F}{\partial d} = \varepsilon \cdot a \cdot Y^*,$$

(2.18)

where $\varepsilon$ is a number between 1.9 and 2.4 [Magonov et al., 1997] describing the strain of the surface.

Taking into account that in dynamic mode AFM the tip is not in permanent contact with the surface, it is appropriate to use time averaged values of the contact radius < *a* > and surface stiffness < *S* >. When tip and surface are in contact, the force derivative $\sigma$ is dominated by the surface stiffness,

$$\sigma \approx \langle S \rangle = \varepsilon \cdot \langle a \rangle \cdot Y^*$$

(2.19)

so Eq. (2.17) can be rewritten as

$$\Delta \phi_0 \approx \langle S \rangle \cdot \frac{Q}{k} = \varepsilon \cdot \langle a \rangle \cdot Y^* \cdot \frac{Q}{k}.$$

(2.20)

The last equation shows that by means of phase imaging a map of stiffness variation on the sample surface can be obtained (cf. Fig. 2.11). Stiff areas with large values of effective elastic moduli will cause more positive phase shifts than soft regions. On the other hand, a softer material can lead to a larger contact area with a longer tip-sample contact, which especially occurs under great bearing force. Here, the contact radius < *a* > can dominate the phase shift, compared to the effective Young's modulus $Y^*$, and enlarge it. If this is the case, an inversion of phase contrast is recorded and soft regions lead to greater phase shifts than

stiff regions. Under low bearing force, adhesive tip-sample forces become increasingly important so that a phase contrast inversion is recorded, as well (due to the sign change of the overall force derivative $\sigma$) [Magonov et al., 1997]. Thus, the quantitative interpretation of phase images remains difficult, as the sources that contribute to the dissipation are not readily accessible, and are strongly influenced by the sample topography [Stark et al., 2001].
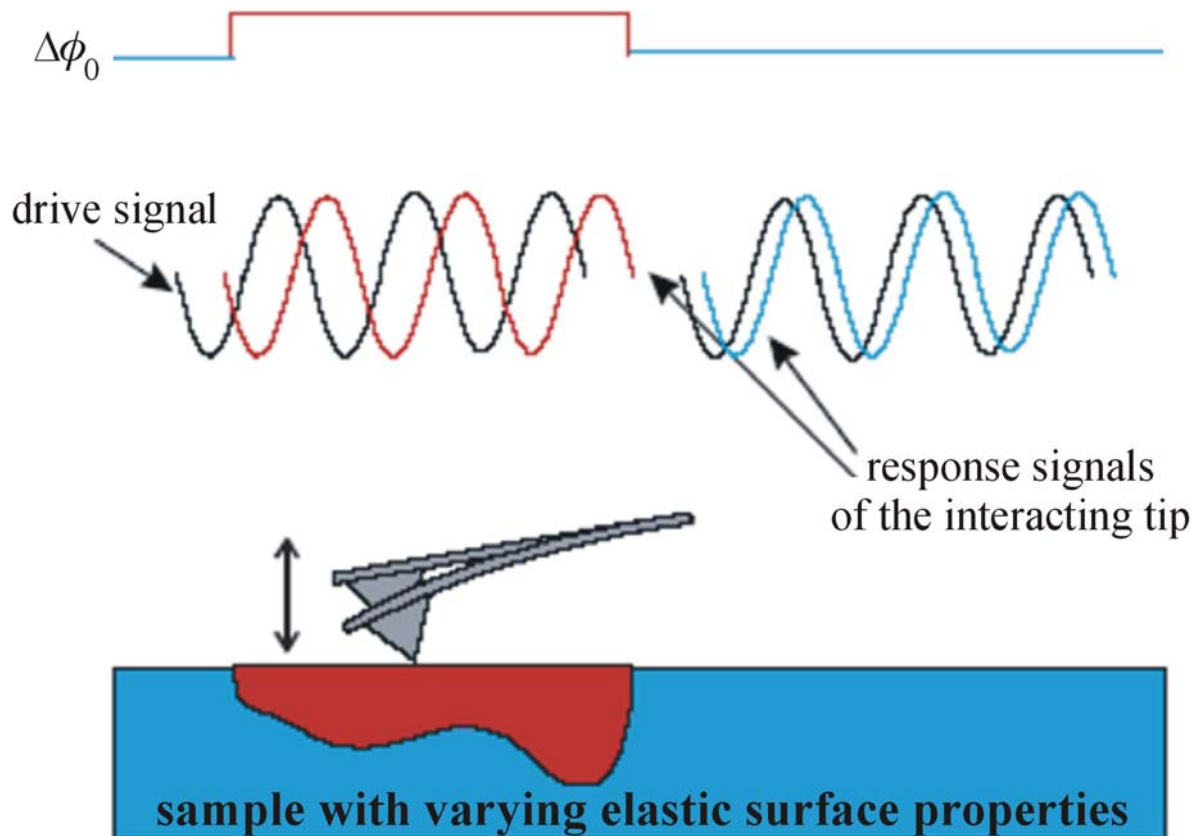


**Figure 2.11** Phase shift variation depending on material-stiffness (adapted from [Delineau, 2001]).

 Nevertheless, phase imaging is a powerful technique to achieve more detailed pictures from appropriate sample surfaces (an example is given in Fig. 2.12) and may highlight areas of different surface features, even those of one-component systems with different density distributions (especially with respect to the grade of image-contrast that cannot be achieved by common height images). Hence, phase shift-based AFM images may yield new insight into the topology of structures which may be concealed for conventional AFM methods under normal circumstances.

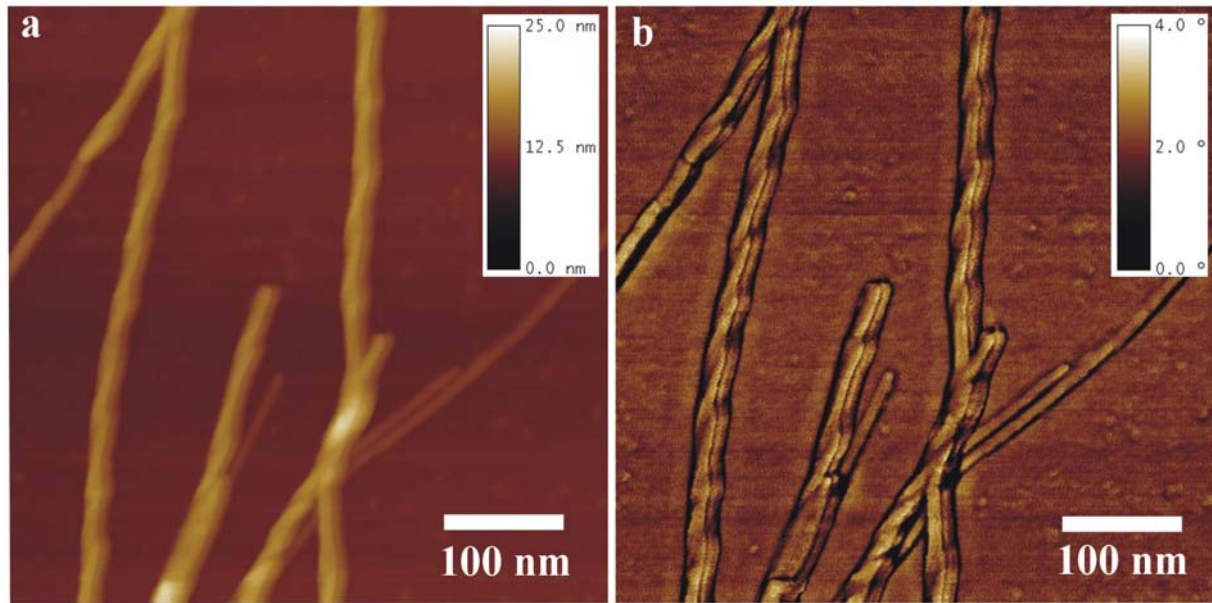**Figure 2.12** The power of phase imaging can be illustrated by comparing a conventional AFM topography image (a) with its corresponding phase shift pendant (b). Although the color-scaling of a phase image does not correspond with the object's height but with the phase shift of the oscillating tip (see vertical color scale bars), a phase image can be considerably more detailed and contrasty.

### 2.1.4 Tip-induced Artefacts

Apart from artefacts caused by damaged or contaminated tips, scanner-hysteresis or thermal and vibrational noise, there is one aspect that has to be primarily taken into consideration for three-dimensional AFM data interpretation, since it is inherent to the system. The AFM images obtained have to be regarded as a convolution of the real topography of the sample and the shape of the tip [Villarrubia, 1996]. In general, the height of an object above the surface can be determined accurately, but the lateral dimension in the plane of the image (width) is distorted due to the shape and finite size of the tip, as the radius of tip curvature and its apex angle can interact with vertical sample features. In addition to this effect, commonly known as "probe broadening", the apparent magnitude of features can also be affected by the topography around them. For example, if one investigates particles adsorbed on a rough substrate, their shape will be influenced by the topography of the substrate around them. Generally, the effects of tip convolution on AFM images of specimens pose a significant problem. Image de-convolution, commonly based on the comparison of recorded images of special "tip-estimation" grids with real shape scanning electron microscope (SEM) pictures, [Markiewicz and Goh, 1995] is a non-trivial process due to factors such as compression and distortion of molecules by the AFM tip [Yang et al., 1996], and inherently unpredictable incidents such as tip shape modification during scanning due to wear or contamination

[Schabert and Engel, 1994]. For samples which are closely packed and have a very low surface roughness, tip convolution becomes negligible because only the apex of the tip takes part in the imaging process.

As a consequence, no additional deconvoluting image processing was performed in this study. To ensure an accurate length and height metrology of sample features, AFM imaging was exclusively conduced on mica-substrate, exhibiting an atomically flat surface over large (typically several microns) areas. Furthermore, horizontal distances were only ascertained if height data between two corresponding topographic maxima could be unambiguously determined. (For further information see chapter 3.)
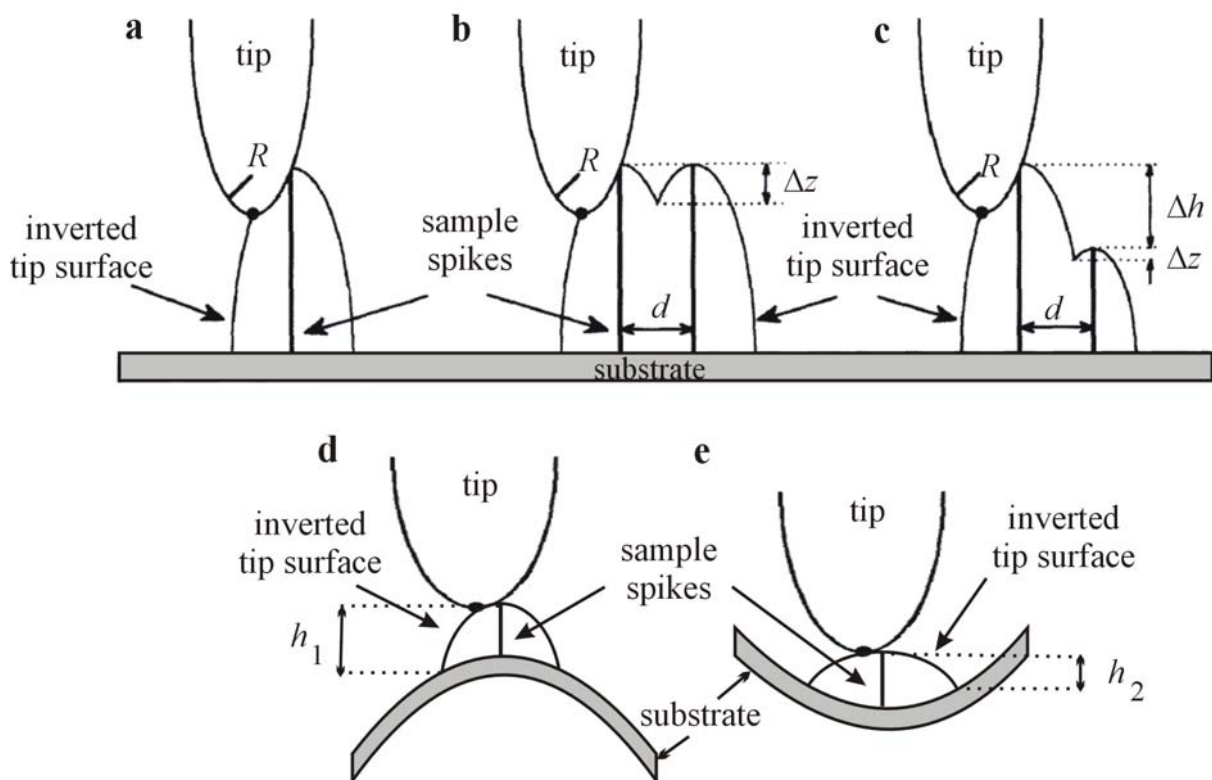
**Figure 2.13** Schematic drawing demonstrating the process of image formation in AFM. (a) Image of a spike obtained with a parabolic tip. (b) Image of two spikes of similar height close together. (c) Image of two spikes of different height. The ability of the AFM to resolve two spikes separated by a distance *d* depends on the size of the dimple $\Delta z$ in the image and decreases with increasing height difference $\Delta h$ between the spikes. Thus, flat samples lead to higher resolution images than rough ones. *R* is the radius of curvature of the tip. (Adapted from [Bustamante et al., 1997].) (d) + (e) In addition to the tip shape, also the local topography of the substrate contributes to the image formation process. Apparently, the particle in the sink seems lower and more flattened than the particle on the peak ($h_1 < h_2$).

## 2.2  Insulin

Insulin is a small globular protein hormone with a molecular weight of 5.7 kD which is produced *in vivo* within the pancreatic β-cells of the islets of Langerhans. It is found not only in all vertebrates including fish but also in starfish, worms and protozoa [Falbe and Regitz, 1995]. Insulin is the primary hormone responsible for controlling the cellular uptake, utilization and storage of glucose, amino acids and fatty acids while inhibiting the breakdown of glycogen, protein and fat. Together with its antagonist glucagon, insulin keeps the blood sugar level constant within certain physiological limits. Stimulating the glucose intake, especially in muscle-tissue, adipose-tissue and liver by binding to specific transmembrane receptors, and triggering a complex signaling pathway that leads to a higher glucose cell membrane permeability, insulin is responsible for the blood sugar drop, while in turn glucagon has the opposite effect [Löffler and Petrides, 1990; Lee and Pilch, 1994].
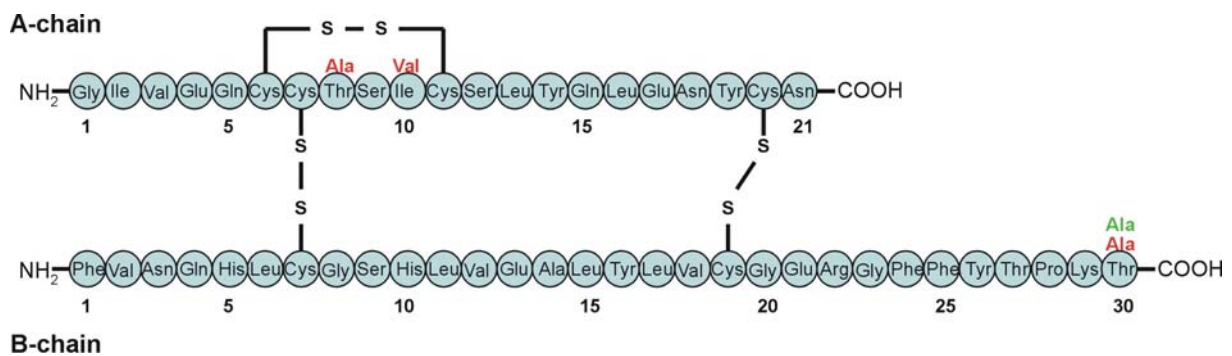


**Figure 2.14** Primary structure of human insulin. The colored superscripts indicate those amino acid residues which are different in bovine (red) and porcine (green) insulin. Adapted from [Nielsen et al., 2001b].

Apart from being included as a medium supplement for cell culture, the foremost pharmacological importance is due to its application in the treatment of diabetes mellitus, which has become one of the most widespread and increasing diseases of civilization. Predominantly, porcine and bovine insulin (which are purified from an ethanol/phosphoric acid extract of pancreas by multiple ammonium sulfate and isoelectric precipitations), as well as human insulin, which is either obtained genetically or through enzymatic conversion of porcine insulin (where Ala is replaced by Thr at B30) [Falbe and Regitz, 1995], are used for the production of medical insulin preparations. To prevent harmful side effects due to badly regulated insulin profiles (which in worst case can lead to a hypoglycemic shock), insulin preparations commonly consist of insulin-protamine (Neutral-Hagedorn-Insulin) or zinc-

insulin compounds, so that a retarded and a middle- to long-termed activity is ensured [McCormick and Quinn, 2002].

In the early nineteen fifties, insulin was the first proteohormone whose amino acid sequence could be deciphered completely by Frederic Sanger and coworkers after a ten-year work in Cambridge [Löffler and Petrides, 1990]. The insulin molecule is composed of two polypeptide chains, the A-chain with 21 residues and the 30 residue B chain. The chains are connected by two disulfide bridges: A7-B7 and A20-B19, while a third bridge comprises cysteine residues 6 and 11 of the A chain. As illustrated in Fig. 2.14, the primary structure of human insulin differs from that of the bovine protein at three amino acid positions (A8 $Ala^{Bov}$/$Thr^{Hum}$, A10 $Val^{Bov}$/$Ile^{Hum}$, B30 $Ala^{Bov}$/$Thr^{Hum}$), whereas it differs from porcine insulin only at one position (B30 $Ala^{Porc}$/$Thr^{Hum}$) [Derewenda and Dodson, 1993]. Structural investigations revealed that these sequential deviations are not located at positions which are functionally significant [Falbe and Regitz, 1995].
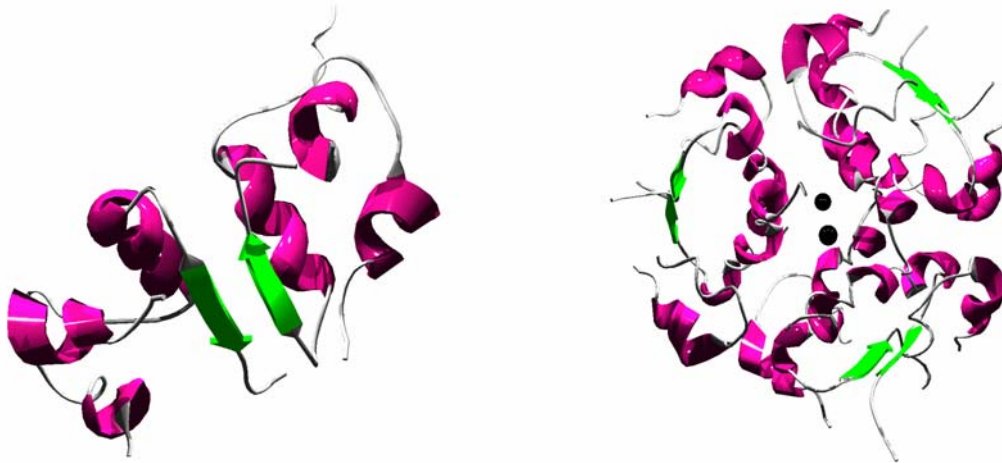


**Figure 2.15** Ribbon diagram of an insulin dimer at pH = 2 (left), which is facilitated by antiparallel β-strand formation between residues B24-B28 of the two monomers, and van der Waals contacts between hydrophobic residues of the B chain α-helix and the β-strand [Whittingham et al., 2002]. The hexamer solution structure at pH = 7 (right) contains two zinc ions at the center interacting with the B10 His side chains ($R_6$ state). This figure was created by POVRAY (version 3.6) [POVRAY], based on the records 1GUJ (dimer) [Whittingham et al., 2002] and 1AIY (hexamer) [Chang et al., 1997], respectively, of the Brookhaven National Laboratory's Protein Data Base [PDB].

Under physiological conditions, the predominant storage form of insulin is a zinc-coordinated hexamer, which is composed of three dimers and stabilized by two or four $Zn^{2+}$ ions [Nieslen et al., 2001b]. For example, in $T_6$ insulin, designating one of three hexameric forms, which to this day have been characterized by X-ray structural analysis, two zinc ions coordinate the B10 His side-chains of the three dimers. (In presence of a high chloride ion

concentration, three of B chain N termini (B1 - B8) adopt a frayed α-helical conformation, which is termed the $R_f$ state. A further hexameric form is the $R_6$ state with all six B chain N termini adopted in a fully α-helical conformation.) In each monomer of the dimer, the A and B chains form a compact fold, including two α-helices in the A chain (residues A1-A6 and A12-A20) joined by a loop and one α-helix in the B chain, spanning residues B9-B19. Among a variety of external factors, decreasing protein concentration or lowering the pH, thereby protonating B10 His side-chains and preventing the coordination of metal ions [Yao et al., 1999], shift the equilibrium towards smaller oligomers. Dimer formation is facilitated by β-strand formation between residues B24-B28 of the two monomers and van der Waals contacts between hydrophobic residues of the B chain α-helix and the β-strand [Whittingham et al., 2002]. Dimer and hexamer formation lead to the burial of exposed hydrophobic surfaces, and may protect the protein from random aggregation interactions. Consequently, conditions that promote the monomerisation, like strongly acidic conditions (complete monomerisation can be achieved by dissolving the native insulin in 20% acetic acid, even at high concentrations, such as 20 mg/ml [Zhang et al., 2002]), give rise to the formation of insulin fibrils [Whittingham et al., 2002].

## 2.3   Polylysine

Poly(L-lysine) (PLL) and Poly(D-lysine) (PDL) are synthetically produced polyamino acids which are mainly used in life sciences to coat slides and other surfaces (glass as well as plastic material) in order to enhance cell adhesion and protein adsorption by altering surface charges due to their polycationic character [Mazia et al., 1975].
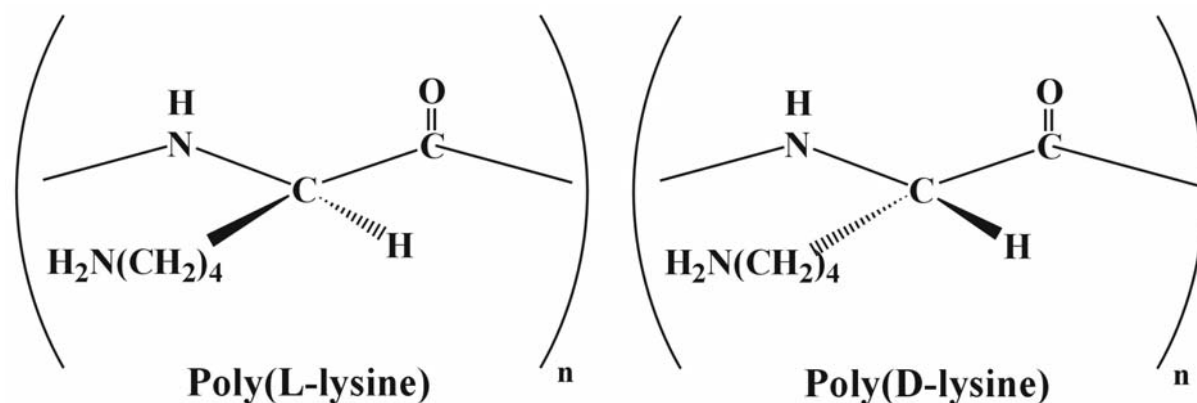


**Figure 2.15** Primary structures of the polyamino acids PLL (left) and PDL (right).

In addition to promoting cell adhesion, polylysine surface treatments support neurite outgrowth and improve the survival of many primary cells of the central nervous system in culture.

A further application of polylysine is as a food and cosmetics additive due to its antibacterial and viscous properties (with growing molecular weight, the viscosity of a polylysine solution increases). In this context it is worth mentioning that polylysine does not cause any flavor deteriorations.

Possible medical application of polylysine as a vehicle for extracellular targeted local drug delivery, which provides high accumulation and long-term retention within the vascular wall [Sakharov et al., 2001], are still under discussion.

There is a wealth of studies on structural transitions in polylysine. PLL (the same is expected for its enantiomer PDL) has a random coil structure in water at pH = 7, but collapses readily into an $\alpha$-helical structure if the pH is increased to 11.1 [Fändrich and Dobson, 2002]. Above this pH level, increasing temperature induces an $\alpha$-to-$\beta$-transition and aggregation in PLL [Jackson et al., 1989]. The process is reversible only at low concentrations. Readjusting the pH from 11.1 to neutral or acidic values leads to the immediate conversion of $\beta$-PLL into a random coil state [Fändrich and Dobson, 2002]. Under these conditions, neither helical nor extended structures of polylysine are energetically favorable because of repulsive forces between positively charged side-chain residues [Dzwolak et al., 2004a]. On the other hand, compensation of the polylysine charges through interactions with negatively charged polyglutamic acid allows both polypeptides to assemble into a $\beta$-sheet even at pH = 7 [Ismail and Mantsch, 1992]. Several factors have been implicated to affect the $\alpha$-to-$\beta$-transition in polylysine. Those promoting hydration of the polypeptide (e.g. high hydrostatic pressure [Carrier et al., 1990b]) were shown to favor the helical conformation, while the generally dehydrating lipid bilayers [Carrier et al., 1990a] and anesthetics [Chiou et al., 1992] have the opposite effect.

## 2.4  Amyloids

Virchow (1854) denominated certain deposits as "amyloid" (Greek: starch flour-containing) which he found postmortem in organs and tissues that gave a positive reaction when stained with iodine. Later it was realized that the material, although originally associated with carbohydrates, particularly glucosoaminoglycans, was in fact predominantly proteinaceous in nature [Sunde and Blake, 1998].

Nowadays, the term "amyloid" describes more precisely the fibrous, misfolded form of originally soluble proteins and polypeptides, which in case of certain degenerative diseases (amyloidoses) are deposited extracellularly in diverse organs. Usually, amyloids consist of straight rigid fibrils ranging in width from 3 to 15 nm and in length from 100 to 1600 nm which in turn are made of diverse filaments [Sipe and Cohen, 2000]. Other common features of these water insoluble aggregates are a specific Congo-Red binding and, as a consequence, a typical green birefringence observed in polarized light. Furthermore, amyloid binding causes a typical shift in the absorption and fluorescence spectra of the fibril-specific dye thioflavin T. Amyloids exhibit a high stability towards temperature, pressure, low pH and proteases. Its X-ray diffraction pattern (with characteristic meridional reflections at ~ 4.7 Å and equatorial reflections at ~ 10 - 12 Å [Sunde and Blake, 1998]) reveal a periodic molecular structure consisting of polypeptide chains in an extended β-conformation, forming hydrogen-bonded-β-sheets which run parallel to the long axis of the fibril, whereas the constituent β-strands are arranged perpendicular to this axis. This core "cross-β-sheet" structure (alternatively called: cross β-conformation) can also be taken as a two-dimensional crystal since the packing is highly ordered along the direction of the fiber axis, but laterally the packing is poor [Sunde et al., 1997].
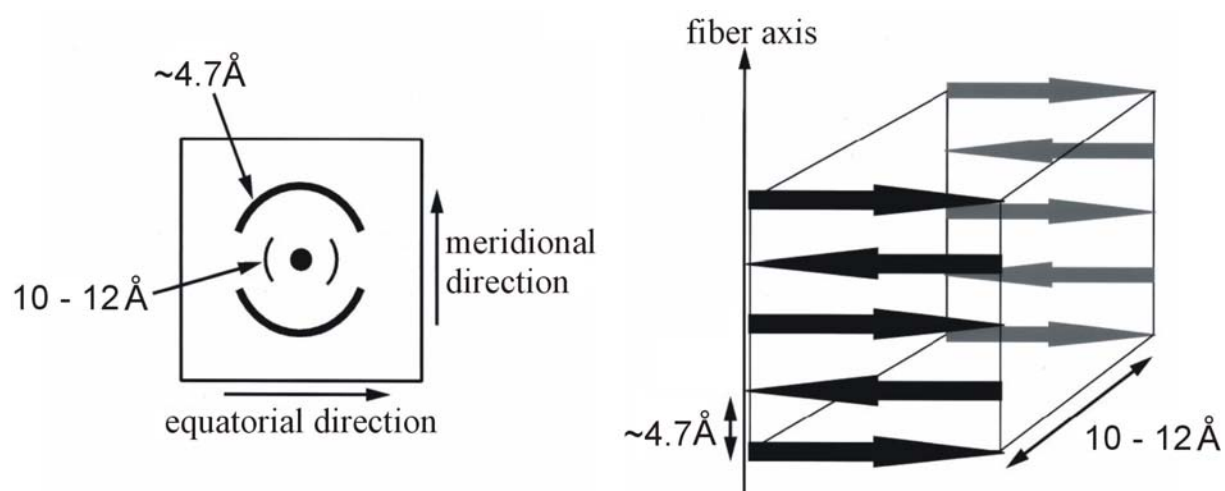


**Figure 2.16** Sketch of a characteristic X-ray diffraction pattern from amyloid fibrils. The strong meridional 4.7 Å reflection corresponds to the hydrogen bonding distance between the strands in the β-sheet structure. A more diffuse equitorial 10-12 Å reflection arises from the intersheet distance (adapted from [Serpell, 2000]).

Regarding the X-ray diffraction pattern of insulin fibrils, a sharp and intense meridional reflection occurs at 4.8 Å and a weaker, more diffuse but still intense reflection is observed at 11 Å [Bouchard et al., 2000]. The 4.8 Å meridional reflection corresponds to the spacing between the strands in the β-sheet structure, and the 11 Å equatorial reflection stems

from the intersheet distance [Sunde and Blake, 1997]. Infrared spectra of the insulin amyloid suggest a parallel arrangement of the β-strands [Buchard et al., 2000], and mass spectrograms of insulin molecules retrieved from fibrils (by alkali extraction) confirm that the disulfide bonds of the native hormone are retained in the amyloid conformation, which is in accordance with a 3D model (see Fig. 2.17) proposed for insulin amyloid fibrils [Jiménez et al., 2002].
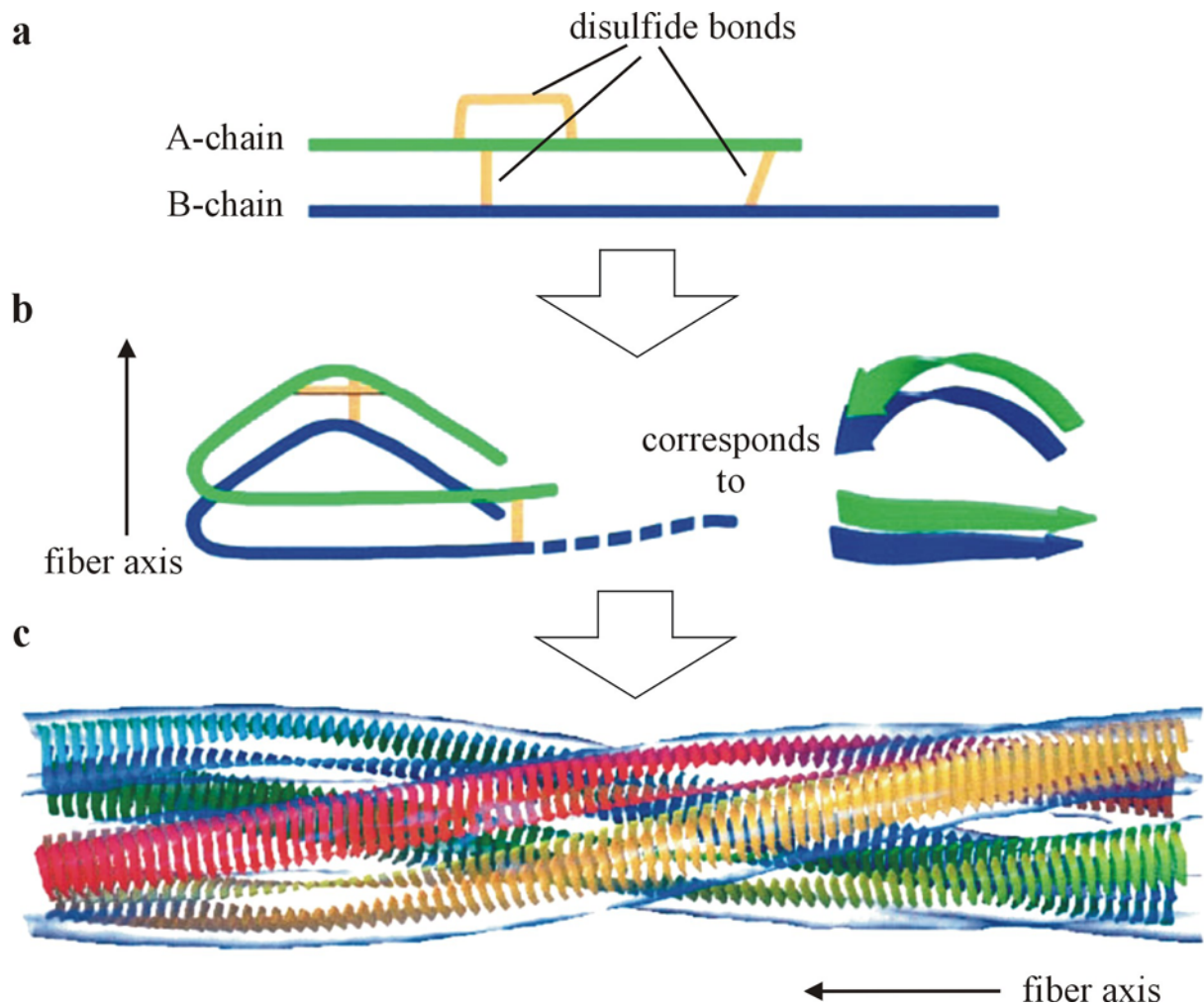


**Figure 2.17** (a) Schematic representation of the topology in an unfolded insulin molecule. (b) Proposed arrangement of the polypeptide chain in the amyloid fiber. The dashed line represents the C-terminus of the B-chain which is not required for fibril formation[3]. The corresponding β-strand model (right) shows that each molecule occupies two layers which are linked by the interchain disulfide bonds. (c) Conceivable schematic β-strand arrangement and protofilament assembly in an insulin amyloid fibril [Jiménez et al., 2002].

As amyloid fibrils can be formed *in vitro* from disease-associated as well as from disease-unrelated proteins, even from proteins like myoglobin with a marginal sequential propensity for the β-sheet fold [Fändrich et al., 2001] under appropriate destabilizing

---

[3] It was shown that Insulin aggregates without 5 or 8 amino acids at the C-terminus of the B-chain (des-pentapeptide insulin (DPI)/des-octapeptide insulin (DOI)) as well.

conditions, including extreme pH [Nielsen et al., 2001a], high temperature [Arora et al., 2004], high pressure [Ferrao-Gonzales et al., 2000], point mutations [Booth et al., 1997], tertiary structure disrupting co-solvents [Chiti et al., 1999], denaturants [Ahmad et al., 2003] and hydrophobic media [Sluzky et al., 1991], amyloid formation is supposed to be a generic feature of polypeptide chains [Fändrich and Dobson, 2002; Stefani and Dobson, 2003]. Nevertheless, the case of natively unfolded proteins, like α-synuclein, shows that a disordered conformation requires appropriate physicochemical circumstances to become susceptible to fibrillation as well [Munishkina et al., 2003].
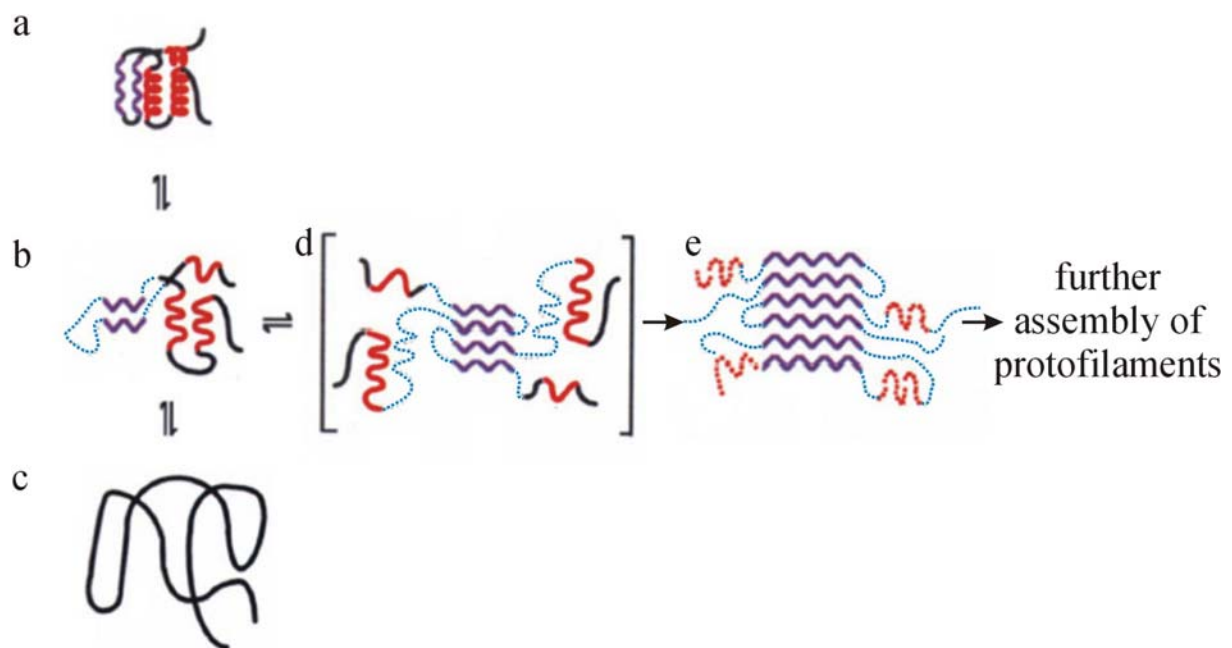


**Figure 2.18** Proposed mechanism of amyloid fibril formation from a typical globular α-/β- protein (adapted from [Booth et al., 1997]). Violet, β-sheet structure; red, helical structure; dotted lines, undefined structure. (a) Distinct form of the native state. (b) A partly unfolded, molten globule-like form of the protein. Conversion of α- to β-structure will be easier in the molten globule state than in the native state because of the lower cooperativity of the unfolding process [Ptitsyn, 1995]. (c) Denatured state. (d) Self-assembly of the β-domain acts as a template for the progressive recruitment of polypeptide chains into the nascent fibril, with the growth of hydrogen-bonded β-structure providing the context for the deposition of polypeptide chains into the stable cross-β fold (e). The undefined regions in (e) indicate that not all of the polypeptide sequence needs to be involved in the cross-β structure. Therefore, the nature and the structural type of this residual structure remain unclear.

Supported by these observations, a recent study [Fändrich and Dobson, 2002] suggested that protein aggregation reflects the "polymeric" character of polypeptides and occurs when main chain interactions are allowed to overrule the specific side-chain contacts within a natively folded protein. Therefore, the formation of amyloids can be understood as an alternative to the native packing conformational struggle of a polypeptide chain to: (i) reduce its accessible

surface area (ASA), (ii) saturate hydrogen bonding, and finally (iii) reach an alternative "non-native" global free energy minimum. In this context, subsequent stages of hierarchical amyloid formation may be expected to enhance the burial of hydrophobic residues and the extent of energetically favorable hydrogen bonding.

Regarding globular proteins (such as insulin), several studies implicate [Bouchard et al., 2000; Booth et al., 1997; Ferrão-Gonzales et al., 2000; Dzwolak et al., 2003] that the initial step for fibrillogenesis is a loosening of the rigid native structure and a conversion into a destabilized partly unfolded conformation which is often coined a "molten globule" state. (The molten globule state is characterized by the presence of a significant degree of secondary structure, folded into a compact hydrophobic core with a highly dynamic or fluctuating tertiary structure [Bryant et al., 1992]). Thus, it becomes clear that for insulin a monomerisation is indispensable, as its native hexameric and dimeric assemblies protect the protein from conformational modifications (see above) [Wittingham et al., 2002]. The structural transformation into this "sticky" but still compact intermediate prone to aggregation facilitates an α-helical to β-sheet conversion thermodynamically because of the lower cooperativity of the unfolding process [Ptitsyn, 1995]. The development of stable β-structure via an intermolecular association can then act as a template for the progressive recruitment of polypeptide chains into the nascent fibril, with the growth of hydrogen-bonded β-structure providing the scaffold for the further incorporation of polypeptide chains into the stable cross-β fold [Booth et al., 1997].

## 2.4.1   High Hydrostatic Pressure Effects

In accordance with Le Châtelier's principle (mobile equilibrium principle), high pressure (at $T = $ const.) shifts (bio-)systems towards the state that occupies a smaller volume and accelerates processes for which the transition state has a smaller volume than the initial state. In other words, pressure favors processes that are accompanied by negative reaction volume changes.

For the specific case of protein structural transitions in aqueous solution, three or four effects deserve particular attention. First, dissociation of chemical species into ions contributes to an overall reduction in system volume due to the electrostrictive effect of separated charges, which causes a more dense arrangement of water molecules in the vicinity of ions than in bulk water. Hence, structural transitions with concomitant formation of charged residues should be favored at high pressure and may foster protein unfolding and

disaggregation. Decreasing the rate of reassociation or reaggregation can be explained by the possibility that non-native salt bridges may be disrupted by high pressure, and pressure-mediated increases in protein charge will serve to increase electrostatic repulsion between protein molecules [Randolph et al., 2002].

Second, owing to a decrease of hydrophobic interaction pressurization leads to penetration of water into the protein interior, and thus the elimination of internal cavities contributes to a substantial volume decrease and may lead to the disruption of the folded structure [Royer, 2002]. Water penetration under pressure can induce the formation of a molten globule-like state, i.e., a compact, partially folded conformation without specific tertiary structure [Boonyaratanakornkit et al., 2002].

Third, the exposure and hydration of polar groups is also accompanied by a decrease in volume. All three pressure effects result in a net-destabilization of compact secondary and tertiary structural elements which are stabilized in the native state apart from hydrogen-bonding through hydrophobic and ion pair interactions [Royer, 2002].

Another, yet debated [Boonyaratanakornkit et al., 2002] factor contributing to the pressure effect on polypeptide assemblies stems from the hydration of hydrophobic residues under high pressure. As hydration volumes of model hydrocarbons, such as benzene or methane, are negative (inter alia, the hydrophobic solvation layer is assumed to be more densely packed than the loosely packed structure of pure water [Kauzmann, 1959]), the exposure of hydrophobic residues which occurs upon the unfolding of proteins appears to be favored at elevated pressure [Gross and Jaenicke, 1994; Randolph et al., 2002].

**Table 2.2** Reaction volumes associated with selected biochemical reactions in water (25°C). (Adapted from [Gross and Jaenicke, 1994; Randolph et al., 2002].)

| Reaction | Example | $\Delta V$ / ml·mol$^{-1}$ |
|---|---|---|
| Ion-pair formation | protein-COOH $\rightarrow$ protein-COO$^-$ + H$^+$ | - 10 |
| | protein-NH$_2$ + H$_2$O $\rightarrow$ protein-NH$_3^+$ + OH$^-$ | - 20 |
| Hydrogen-bond formation | poly(L-lysine) helix formation | - 1 |
| Hydrophobic hydration | C$_6$H$_6$ $\rightarrow$ (C$_6$H$_6$)$_{water}$ | - 6.2 |
| | (CH$_4$)$_{hexane}$ $\rightarrow$ (CH$_4$)$_{water}$ | - 22.7 |
| Hydration of polar groups | n-propanol $\rightarrow$ (n-propanol)$_{water}$ | - 4.5 |

As shown in theoretical studies [Hummer et al., 1998], high pressure generally retards folding kinetics [Panick and Winter, 2000], though it may also induce alternative non-native conformations in proteins [Herberhold and Winter, 2002]. There is an apparent paradoxical

effect of hydrostatic pressure on protein aggregation because, on the one hand, it prevents the aggregation (as water molecules can fill in the protein's void volume when it becomes accessible upon subunit dissociation leading, to a total volume contraction) [Gross and Jaenicke, 1994; Mozhaev et al., 1996; Dzwolak et al., 2003] and favors dissociation of protein aggregates [Gorovits and Horowitz, 1998; Foguel et al., 2003]. On the other hand, it may trigger formation of aggregation-prone intermediates [Smeller et al., 1999; Ferrão-Gonzales et al., 2000]. In most cases, fibrils are then formed after pressure release, only. Since high pressure was shown to disfavor insulin aggregation, as this proceeds through an expanded intermediate structure [Ahmad et al., 2003], the question arises weather moderately high pressure promotes a competing "low volume" conformational pathway leading to a structurally distinct amyloid.

### 2.4.2   Cosolvent Effects

Under physiological conditions, the native fold of a protein and hence its normal biological activity is balanced by a rather complex mixture of water, cosolvents and other cosolutes [Timasheff, 1993]. Moreover, the aggregation behavior of proteins, such as the onset, the aggregation rate, and the final morphology of the aggregated state (i.e., amorphous precipitates or fibrils), has been found to depend strongly on the properties of the protein environment in solution as well as on the intrinsic thermodynamic stability of the native state of the protein relative to that of the aggregation competent state [Chi et al., 2003]. Furthermore, folding and aggregation of partly denatured folding intermediates are thought to underlie predetermined patterns that minimize the free energy of destabilized proteins states, like the burial of hydrophobic residues, the saturation of dangling hydrogen bonds or the reduction of the ASA. Also, the competition between intra- vs. inter-protein interactions is influenced by solvational preferences of the participating protein states.

Quite early it has been recognized that certain solutes (e.g. polyols, sugars and certain salts, such as ammonium sulfate) stabilize the native state of proteins as well as their oligomeric assemblies, whereas other solutes act as protein denaturants and foster dissolution of hydrophobic aggregates (e.g. urea and guanidine hydrochloride) [Moelbert et al., 2004; Timasheff, 1998]. These observations can be explained by different binding preferences of these weakly interacting solutes for native and unfolded states. Destabilizers bind to the protein-water interface of the unfolded state to a higher degree - essentially due to the larger ASA - than to the native state, thus favoring unfolding [Chi et al., 2003]. On the other hand,

protein stabilizers, such as sucrose and glycerol (which is also known to enhance ordered aggregation, thereby reducing the ASA of the protein [Yang et al., 1999]), are preferentially excluded from the surface of the protein molecule, and the degree of exclusion is proportional to the ASA [Timasheff, 1998]. These cosolvents - at least at low and medium high concentrations - are depleted in the vicinity of the protein and, as a consequence, the relative concentration of water molecules increases at the protein interface. Preferential exclusion of the cosolvent and an excess of water in the immediate vicinity of the protein is defined as "preferential hydration" and can be interpreted thermodynamically as negative binding. During the unfolding process, the protein surface area increases, leading to a larger excluded volume. The increase of negative binding upon unfolding makes the native state thermodynamically more favorable.

A thermodynamic way to explain the mechanism by which preferential hydration stabilizes the native state is to consider that an unfavorable interaction between the cosolvent and the protein coincides with an increase of the chemical potential of the protein [Timasheff, 2002]. The system tends to minimize its chemical potential. Therefore, protein states with reduced ASA are favored over more solvent-exposed states. Hence, the free energy of unfolding is increased in the presence of preferentially excluded cosolutes. Furthermore, the assembly of monomers into oligomers also reduces the ASA of the protein and therefore is favored [Chi et al., 2003].

More subtle effects are observed in the case of monoalcohols and their fluorinated derivates, such as ethanol and 2,2,2-trifluoroethanol (TFE), which are assumed to be more potent in inducing structural conversions of proteins [Hirota et al., 1998]. It is generally observed that alcohols promote secondary structure, especially α-helices, but at the same time act as destabilizers of tertiary and quaternary structures within the folded protein [Buck, 1998], occasionally leading to partially folded molten globule-like conformations. However, their mode of action is still a matter of dispute and certainly depends on their concentration. Alcohols exhibit a lower dielectric constant than water and are much weaker hydrogen bond acceptors. These properties give rise to a series of proposed interaction mechanisms, including perturbation of the protein water shell [Walgers et al., 1998; Kentsis and Sosnick, 1998], diminution of hydrophobic interactions [Thomas and Dill, 1993], strengthening of intra-protein hydrogen bonding, and less shielding of electrostatic interactions due to the lower polarity of alcohols [Hirota et al., 1998]. Other mechanisms include preferential binding with simultaneous dehydration of the immediate vicinity of the protein [Bull and Breese, 1978; Fioroni et al., 2002] and the impact of cosolvent clustering to provide local regions of

low polarity [Hong et al., 1999]. The effects of alcohols on protein folding were shown to depend on the alcohol concentration in a non-monotonic fashion [Cinelli et al., 1997]. Likewise, the promotion of aggregation-prone folding intermediates has been observed in a limited range of alcohol concentrations, as has been shown, for instance, for the Alzheimer β-protein [Fezoui and Templow, 2002], α-synuclein [Munishkina et al., 2003] and the acidic fibroblast growth factor [Srisailam et al., 2003]. These observations point to the importance of the interplay between various, eventually antagonistic, effects on protein aggregation in the case of alcohols as cosolvents.

### 2.4.3    Relation to Prion Strain Phenomenon

One of the fundamental tenets of molecular biology states that under physiological conditions only one "native" three-dimensional structure may be formed out of a single amino acid sequence of a biologically functional protein. This view has recieved powerful experimental support ever since the pioneering works by Anfinsen [Anfinsen et al., 1954; Anfinsen, 1973] and became the pillar of protein folding theories relating the global energy minimum with the native state of the protein. This paradigm is illustrated in the folding funnel model [e.g. Onuchic and Wolyness, 2004], wherein a protein conformation surfs downwards, decreasing its free energy and conformational entropy. By sampling only a limited number of transient conformations, this quickly leads to the global energy minimum and - inevitably - to the native structure of the protein. But the perplexing observation that a single amino acid sequence of the prion protein propagating in genetically identical hosts may still evoke several distinct phenotypes (both in terms of clinical symptoms, e.g. incubation times and brain lesions pattern, and physicochemical properties) of the prion - the so-called prion strains - was used as an argument against the prion theory (along with the difficulty in de novo creating of the prion type infectivity) [Weissmann et al., 2002]. It appears to be well established by now, however, that the phenomenon of strains originates from the conformational diversity of yeast [Tanaka et al., 2004], human [Vanik et al., 2004], hamster and mouse [Peretz et al., 2002] prions. The tendency to form a particular strain may be enhanced by the amino acid sequence itself, i.e., also mutations [Chien and Weissmann, 2001], by the binding of peptide ligands [Tremblay et al., 2004] and ions [Wadsworth et al., 1999], or by varying physicochemical parameters, such as temperature [Tanaka, et al., 2004].

A very important hallmark of prion strains is the ability to preserve an original folding and aggregation pattern based on a once-formed template while spreading in an environment

that exhibits an inherent thermodynamic preference for another type. The interspecies-barriers prions are facing *in vivo* [Weissmann et al., 2002], and the ability of prions to overcome such barriers by evolving a new and more promiscuous type of strain [Peretz et al., 2002] are the two prominent aspects of the "strain" behavior.

The claim of a common generic character of amyloids as polymers leads to the question whether prion strains themselves stem from an analogous common generic trait of amyloids, including those unassociated with prion diseases. To test this hypothesis, a suitable amyloidogenic protein like insulin, which is genetically unrelated to strain-forming precursors, is employed in this study. Insulin is a suitable model, because insulin aggregation is an energetically self-sustaining process [Dzwolak et al., 2003], enabling seeding experiments at ambient temperature. Inducing amyloid formation through seeding, rather than through an en masse destabilization of the native protein (e.g. by prolonged heating), has the advantage of being a more adequate model for an *in vivo* process. Moreover, seeding under non-denaturing conditions effectively prevents spontaneous formation of different templates (e.g., "lateral" templates). A perturbation of hydrational forces affects the stability of insulin aggregation nuclei and leads to distinct fibrillar types [Nielsen et al., 2001a]. Therefore, the examination (in form of cross-seeding experiments) of the question, whether such solvent-programmed conformation may act as templates inducing conserved fibrillar types, even under conditions favoring different morphologies, could reveal parallels to the prion strains phenomenon and act as an argument for the generic character of strains.

# 3 Materials and Methods

## 3.1 Materials

Bovine insulin, poly(L-lysine) (PLL) and poly(D-lysine) (PDL) were purchased from Sigma Aldrich, Steinheim, Germany and used without further purification. The molecular weight of the polyamino acids was approximately 27 kD. Muscovite mica was purchased from Plano GmbH (Wetzlar, Germany). Other chemicals of "suprapur" or "ultrapure" grade (including sodium hydroxide, hydrochloric acid, ethanol, glycerol, and 2,2,2-trifluoroethanol (TFE)) were obtained from VWR (Merck GmbH, Darmstadt, Germany). Throughout all experiments, only ultrapure water (resistivity at 25 °C > 18 MΩ cm) produced from an ELGA PURELAB Classic polisher system (ELGA LabWater, Celle, Germany) was used.

All accessories required for preparation and handling of insulin and PDL/PLL amyloid samples, such as vessels and tips, were either disposable, single packed and classified as "biopur", or - in case of glass materials - cleaned with a saturated solution of sodium hydroxide in ethanol (both chemicals of the "suprapur" grade) for at least five days and subsequently rinsed with aqueous HCl-solution and ultrapure water.

## 3.2 Insulin Amyloid Formation

### 3.2.1 Time-Resolved Experiments at 60 and 70 °C

Fresh 0.1 wt % (0.17 mM) insulin solutions, pH-adjusted with diluted HCl solution to 1.6, were incubated at 60 or 70 °C for 0 min, 0.5 min, 1 min, 5 min, 10 min, 20 min, 30 min, 1 h, 24 h and 1 week. Immediately after the incubation, the protein samples were diluted 400 times with ultrapure hydrochloric acid in water (pH = 1.6), and 30 µL were spread onto freshly-cleaved muscovite mica of 9 mm diameter, which was attached to a 15-mm magnetic steel disc serving as AFM sample holder. The abrupt dilution of these samples immediately quenches the concentration-dependent aggregation process. Moreover, the deposition of the tiny aqueous droplets on the mica surface is followed by very fast (timescale of seconds) evaporation of bulk solvent, which eventually prevents further aggregation. Therefore, throughout the following overnight drying period no further structural transitions are likely to occur in the amyloid samples. The AFM samples were dried gently with a nitrogen flow and

left overnight before the measurements, which helps to improve the quality of the AFM data due to a reduction of moisture layer covering the sample. Control samples (freshly cleaved mica, mica and aqueous HCl-solution) were also investigated with AFM to exclude possible artifacts.

### 3.2.2   High Hydrostatic Pressure Experiments

The fibrillization of bovine insulin (0.5 wt % in water, pH-adjusted to 1.6 with hydrochloric acid) was performed within a pressure cell from ISS (Champaign, Illinois, USA), originally built for a K2 fluorometer of the same company. The samples were kept at 60 °C for 20 hours after increasing the pressure either to 750, 1200 or 1500 bar, and kept for one hour after pressure-release. Control samples were kept at ambient pressure and 60 °C for 21 hours. The further AFM-sample preparation procedure equals that of the time-resolved experiments (see above).

### 3.2.3   Cosolvent Experiments

Fresh 0.1 wt % insulin solutions, in different water/cosolvent mixtures (see Table 3.1), pH-adjusted to 1.6 with hydrochloric acid, were incubated at 60 °C for 6 days. Upon a 400 fold dilution with HCl at pH = 1.6, 30 µL were applied onto freshly cleaved mica and allowed to dry. The further AFM-sample preparation proceeded in accordance with the instruction given in paragraph 3.2.1.

**Table 3.1** Experimental overview of the water/cosolvent mixtures and incubation times used.

| Incubation time | Cosolvent | Cosolvent content of the reaction solution |
| --- | --- | --- |
| 6 days | TFE | 5 wt %, 20 wt %, 40 wt % |
| 6 days | Glycerol | 5 wt %, 20 wt %, 40 wt % |
| 6 days | EtOH | 5 wt %, 20 wt %, 40 wt %, 70 wt % |

### 3.2.4   Seeding and Cross-Seeding

For the seeding experiments, 0.1 wt % solutions of bovine insulin in either $H_2O$ or 20 wt % ethanol in water were pH-adjusted to 1.6 with diluted HCl solution. The clear solutions were incubated for 24 h at 60 °C, which results in complete fibrillization of the insulin. Subsequently, the obtained fibril suspension was sonicated (in a Sonorex RK 100 SH ultrasonic bath, which had a HF-peak output of 2×160 W/per. at a permanent frequency of 35 kHz and was purchased from Bandelin GmbH & Co. KG, Berlin, Germany) for 30 min at room temperature prior to the mixing with the native protein. For seeding and cross-seeding, respectively, fresh insulin solutions (0.1 wt %; pH-adjusted to 1.6) in either $H_2O$, or 20 wt % ethanol in water were doped with freshly sonicated -fibril suspensions (water or 20 wt % EtOH/water) at a 20 : 1 volume ratio (see Fig. 3.1). The seeded samples were incubated for 24 hours at 25 °C, which was sufficient for complete insulin aggregation.
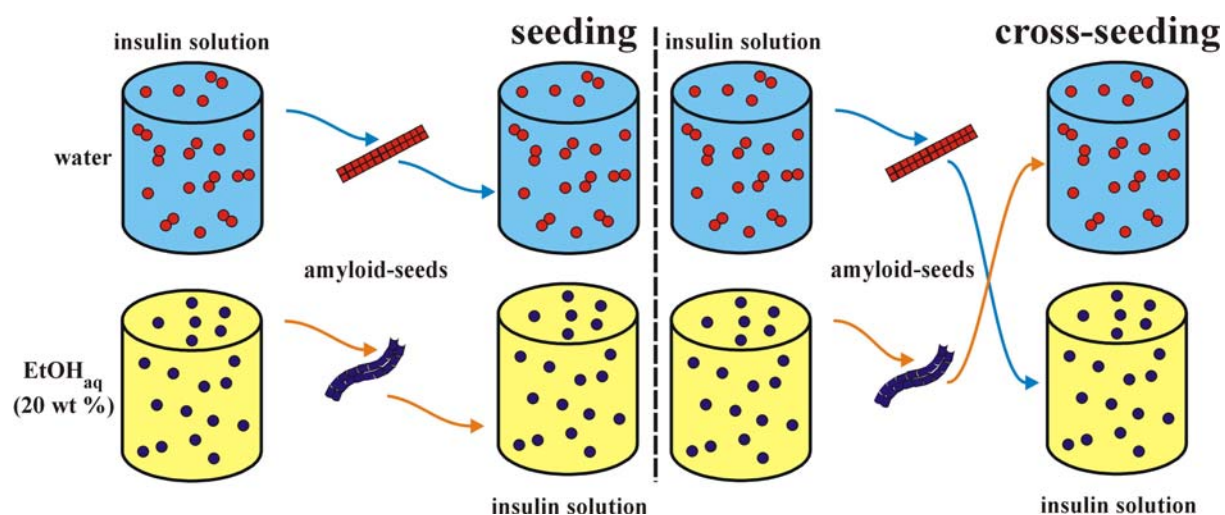


**Figure 3.1** Scheme of the seeding (left) and cross-seeding (right) procedure.

The following AFM-sample preparation steps, such as dilution and application onto a freshly cleaved mica disc etc., are similar to those given in paragraph 3.2.1. Additionally, control samples of a fresh insulin solution (0.1 wt %, pH = 1.6), an insulin solution (0.1 wt %, pH = 1.6) incubated for 24 hours at 25 °C, and a 1:20 seed solution (0.1 wt %) were inspected by AFM to rule out features not provoked though seed-induced fibrillation (for relating AFM images, see appendix, Fig. 7. 4).

## 3.3   Polylysine Fibril Formation

Fibrillar samples for AFM imaging were obtained through a prolonged incubation (120 h) of mixed 1.5 wt % solutions of PLL and PDL in $H_2O$, pH-adjusted to 11.6 with NaOH, at a temperature below the conformational transition of a single enantiomer (20 °C), thus preventing spontaneous heat-induced aggregation of the respective PAA. Subsequently, the sample was diluted 100 or 150 times in water, pH pre-adjusted to 11.6 with NaOH, and applied (15 µL resp. 2 µL) onto a freshly cleaved mica disc (9 mm diameter). After drying in air (1-2 h), AFM data were acquired in tapping mode. In order to exclude artifacts, control samples, like freshly cleaved mica, mica applied with 15 µL aqueous sodium hydroxide solution (pH = 11.6), and mica applied with 15 µL alkaline PLL-solution or PDL-solution (pH = 11.6) (the latter should rule out the possibility of heat-induced aggregation), were also investigated with AFM. Additionally, heat-induced  PDL and PLL fibril formation was recorded to back up the identification of mixed fibrils in terms of size and morphology (70 °C, incubation time: 48 and 72 h).

## 3.4   AFM Instrumentation

All AFM images were recorded on a MultiMode scanning probe microscope equipped with a Nanoscope IIIa Controller from Digital Instruments (Santa Barbara, California, USA). The microscope was coupled to an AS-12 E-scanner (13-µm) and an Extender Electronics Module EX-II (Santa Barbara, California, USA), which allows for acquisition of phase images. Typically used AFM-probes were aluminum-coated NCHR silicon SPM sensors (force constant = 42 N/m; length = 125 µm; resonance frequency ≈ 300 kHz; nominal tip radius of curvature ≤ 5 nm) from Nanosensors (Neuchâtel, Switzerland). For the high resolution imaging, the AFM head with optical block and base was placed atop a commercially available active, piezo-actuated vibration-damping desk from Halcyonics (Göttingen, Germany).

## 3.5   AFM Operation and Image Analysis

Throughout the measurements, the "tapping-in-air" AFM mode was used. This affords both lateral and vertical resolution in the nanometer regime and enables nondestructive imaging of soft surfaces or weakly attached samples. Only completely dry samples were subjected to

AFM imaging. Because a shift of the resonance frequency of the AFM cantilever is induced by approaching the tip to the surface, the drive frequency, which has to be adjusted before first surface contact, is reduced until the vibrational amplitude reaches 95% of the maximum value. The typical value of drive amplitude was 120 - 700 mV. To prevent thermal or scanner-drifts, images were recorded after a warm-up phase of at least 2 h.

Height and phase-shift data were collected simultaneously in the trace-retrace direction of a raster scan. Additionally, the scan-angle or direction was changed in case of repeated scans to exclude scan artifacts caused by contaminated or damaged probes. To ensure correct height data, scanner calibration in the *z*-direction was checked by height measurements on mica crystal layers, which exhibit steps of precisely 1 nm. The scan rate was tuned proportionally to the area scanned (from 500 nm × 500 nm to 10 µm × 10 µm) and was kept within the 0.75 - 2 Hz range. To reduce the possibility of tip contamination, samples were engaged at a zero scan position. The resolution of image acquisition was 512 pixels per line (512 × 512 pixels/image).

To minimize possible distortional effects, the lateral size determination method was applied. This permits sufficiently accurate height determination (maximal vertical resolution was 0.1 Å). Horizontal distances were only ascertained if height data between two corresponding topographic maxima could be unambiguously determined. Vertical dimensions of the fibrillar aggregates were obtained from individual cross-section profiles generated by the AFM accessory data analysis software (Nanoscope III 5.12r3). Whenever the size of a probed object was appropriate, 20 subsequent measurements of an individual feature were carried out and averaged. If necessary, only first-order plane-fittings were performed with the analytical software. If a small substrate tilt angle remained, the height was measured twice at both the cis- and the trans-position of the relating object. The fibril periodicity was determined by two methods after profiling the longitudinal fibril axis: 1) through the averaging of distances between two neighboring maxima and 2) through the averaging of distances between the most remote maxima divided by the number of elevations. Only if the two sets of data were in accordance (occasionally an exact location of the apex is difficult), the data were analyzed and are discussed.

# 4   Results and Discussion

## 4.1   Insulin Fibrillogenesis at 60 and 70 °C monitored by Time-lapse AFM

### 4.1.1   Prefibrillar Stage

Figure 4.1 (see next two pages) presents the progress of the spontaneous amyloidogenesis of insulin at 60 °C (Fig. 4.1, a - i) and 70 °C (Fig. 4.1, j - r) in a time-dependent sequence of AFM images. The increased temperature shortens the lag phase of the aggregation, which is defined here as lapse-time passed until the appearance of first fibrillar forms (rather than of transient early amorphous aggregates - see Fig. 4.1, b, c, and j). The lag phase of insulin aggregation may be monitored by a number of techniques sensitive to larger protein assemblies (e.g., light scattering) or selectively detecting the amyloid fibrils (fluorescence of amyloid labeled with thioflavin T; e.g., [Jansen et al., 2004]). Unless the aggregation process is enhanced by preformed insulin (the so-called seeding [Dzwolak et al., 2004b]), the lag phase is a typical feature of protein amyloidogenesis related to the thermodynamically unfavorable nucleation process [Bouchard et al., 2000; Nielsen et al., 2001a]. The tiniest seed-like forms appear within the first minute of incubation at either temperature. Once a sufficient amount of nuclei is formed, the following phase of fibril elongation becomes the major route of the conformational transition of insulin. This is reflected by the rapid increase in the number of fibrils and the increasing complexity of fibrillar topology (Fig. 4.1, e - i, and m - r). Some characteristic traits of the mature amyloid fibrils are their tendency to bend, twist, and agglomerate. At 60 °C, primary branches and twists occur after 10 min and are followed by bent structures. The lateral association is seen in the corresponding AFM images after 30 min at 60 °C, but already after ∼ 20 min at 70 °C. The further growth beyond 1 h is accompanied by formation of super-fibrillar structures. The increased temperature also appears to accelerate the elongation stage. Unlike at 60 °C, the fibrillization at 70 °C appears to be complete within ∼ 24 h (Fig. 4.1 q) and no remaining oligomers are detected. The AFM images of the mature amyloid at 70 °C (Fig. 4.1 q and r) clearly show domains of parallel fibrils with little tendency to crisscross.

After this brief characterization of the gross stages of insulin amyloidogenesis, a more detailed analysis will be put forward. Figure 4.2 shows the unheated insulin sample, which at room temperature (20 °C) has little tendency to aggregate. The two images present singular
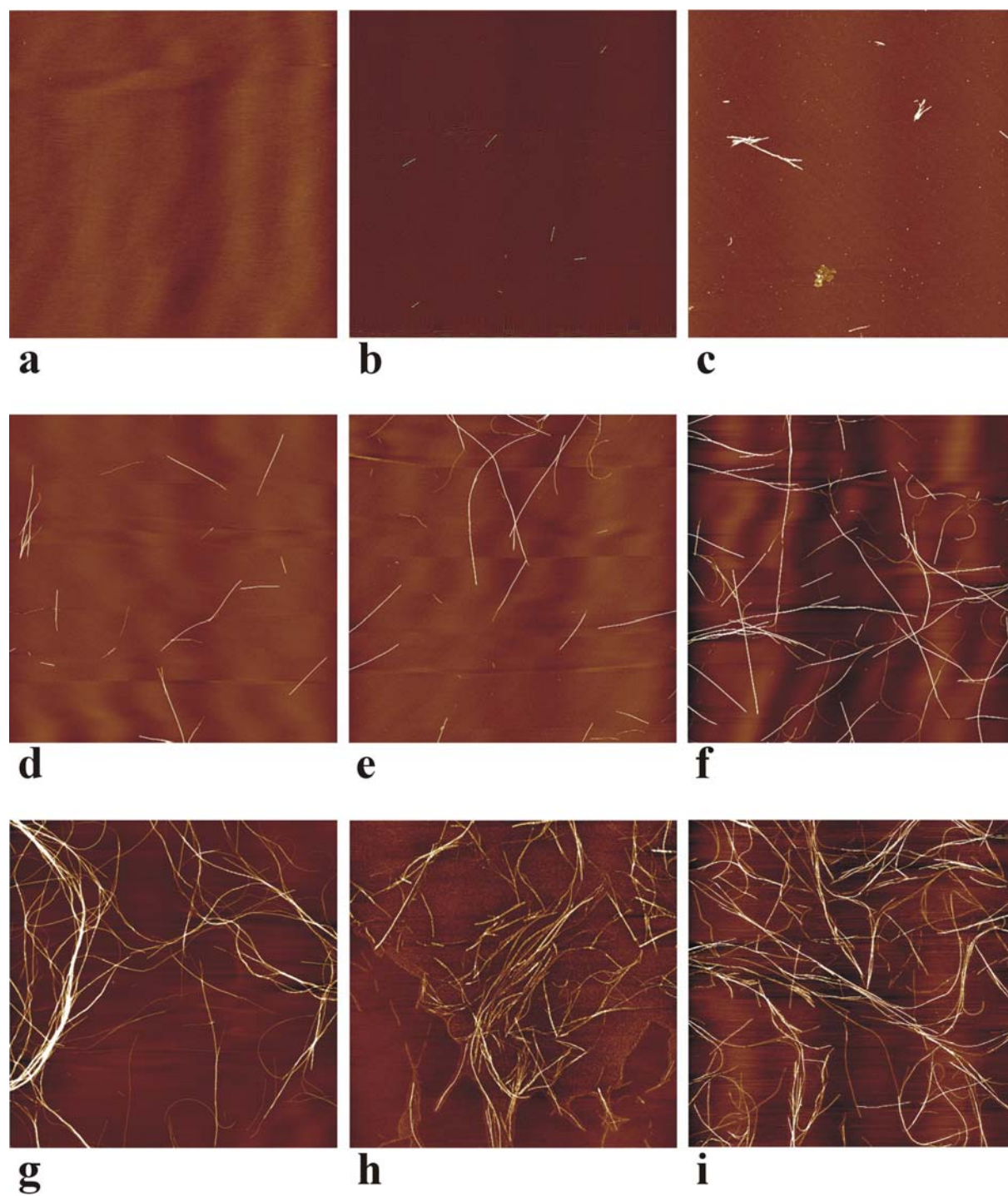
**Figure 4.1 (first part)** The overview of insulin fibrillization at 60 °C monitored by time-lapse AFM. The following images correspond to: 0 min (a), 1 min (b), 5 min (c), 10 min (d), 20 min (e), 30 min (f), 1 h (g), 1 day (h), and 1 week (i). The scan size of each picture is 10 µm × 10 µm.
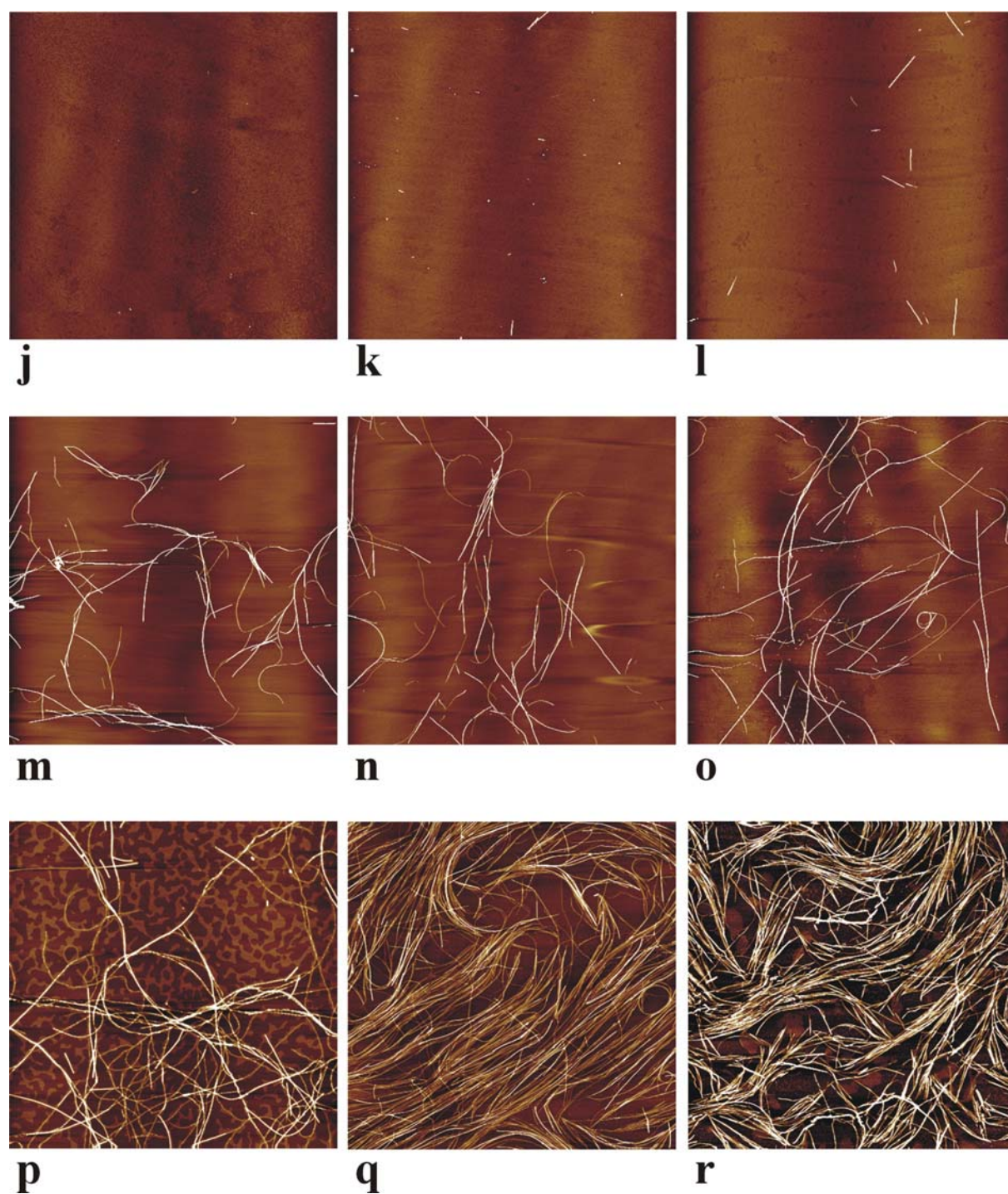
**Figure 4.1 (continued)** The overview of insulin fibrillization at 70 °C monitored by time-lapse AFM. The following images correspond to: 0 min (j), 1 min (k), 5 min (l), 10 min (m), 20 min (n), 30 min (o), 1 h (p), 1 day (q), and 1 week (r). The scan size of each picture is 10 µm × 10 µm.

particles randomly distributed over the whole surface. The particles have heights of (1.1 ± 0.2) nm. Given the accuracy of the height determination and that of X-ray diffraction and small-angle X-ray scattering data (e.g. [Nielsen et al., 2001a; Ahmad et al., 2003]) on the actual dimensions of native insulin monomers (∅ = 1.11 nm) and dimers (∅ = 1.49 nm) - the two predominant species at this low pH - ,the particles appear to be lying flat on the mica surface.
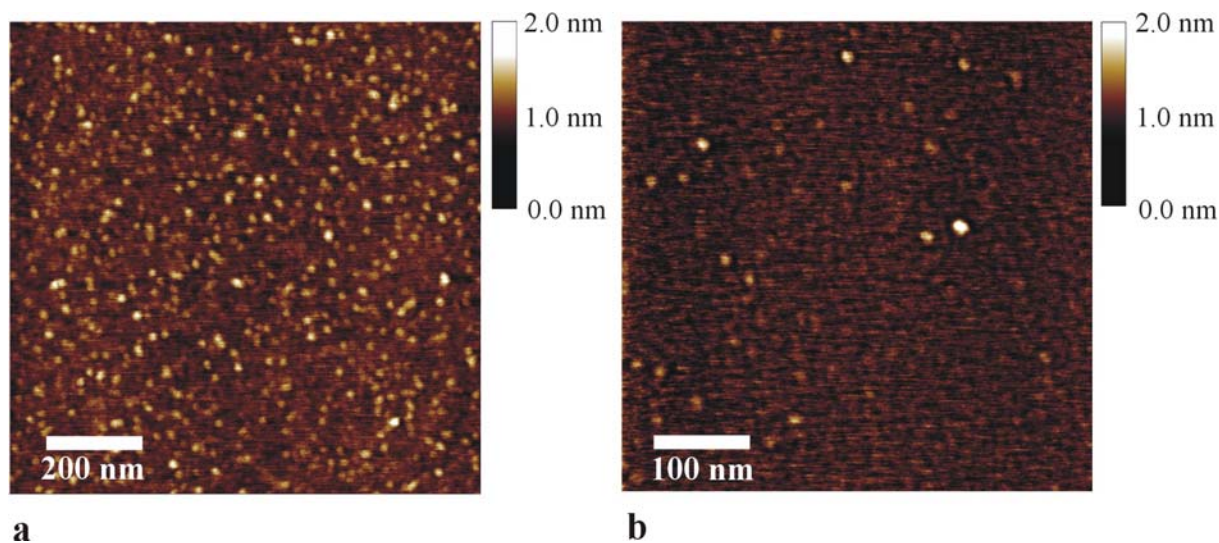


**Figure 4.2** An AFM height image of fresh, unheated insulin solution, pH = 1.6, *T* = 20 °C (a). The magnified image in b shows spherical shapes of the protein particles.

The shortest incubation time at 60 °C (or 70 °C) applied to insulin samples was only 30 s. Yet, as Fig. 4.3a proves, this treatment is capable of already inducing pronounced changes in morphology of the small insulin particles, which immediately begin to cluster. Previous studies have pointed out that at low pH and in the absence of cosolvents the dimeric insulin must undergo temperature-induced monomerization before the actual aggregation occurs [Nettleton et al., 2000; Hua and Weiss, 2004]. As determined earlier from our group, this preliminary stage of the aggregation process is endothermic [Dzwolak et al., 2003] and occurs above 50 °C. The monomers are prone to fast oligomerization. Although newly formed oligomers initially retain a native-like structure [Bouchard et al., 2000], they represent the last pre-amyloidal state with a native secondary fold. The once-formed oligomers will remain after the temperature decrease, acting as early nucleation centers. Interestingly, the clusters are not spherical, and peal-like arrangements and elongated forms appear to dominate (examples are marked in Fig. 4.3a with arrows and a green line). Given the height scaling used in these measurements, the elongated species are not loosely interacting groups of single

particles, but, instead, unified entities. The brief high temperature treatment of insulin for 30 s already results in a marked broadening of the height-distribution of the particles, shifting toward larger oligomers, as is shown in Fig. 4.3b. Such large (3.2 - 3.9 nm in diameter) partially unfolded spherical oligomers are apparently capable of merging into an amyloid precursor. The remarkable size may result from both the number of monomers involved and the fact that insulin aggregation intermediates are rather bulky and swollen with water [Dzwolak et al., 2003; Ahmad et al., 2003].
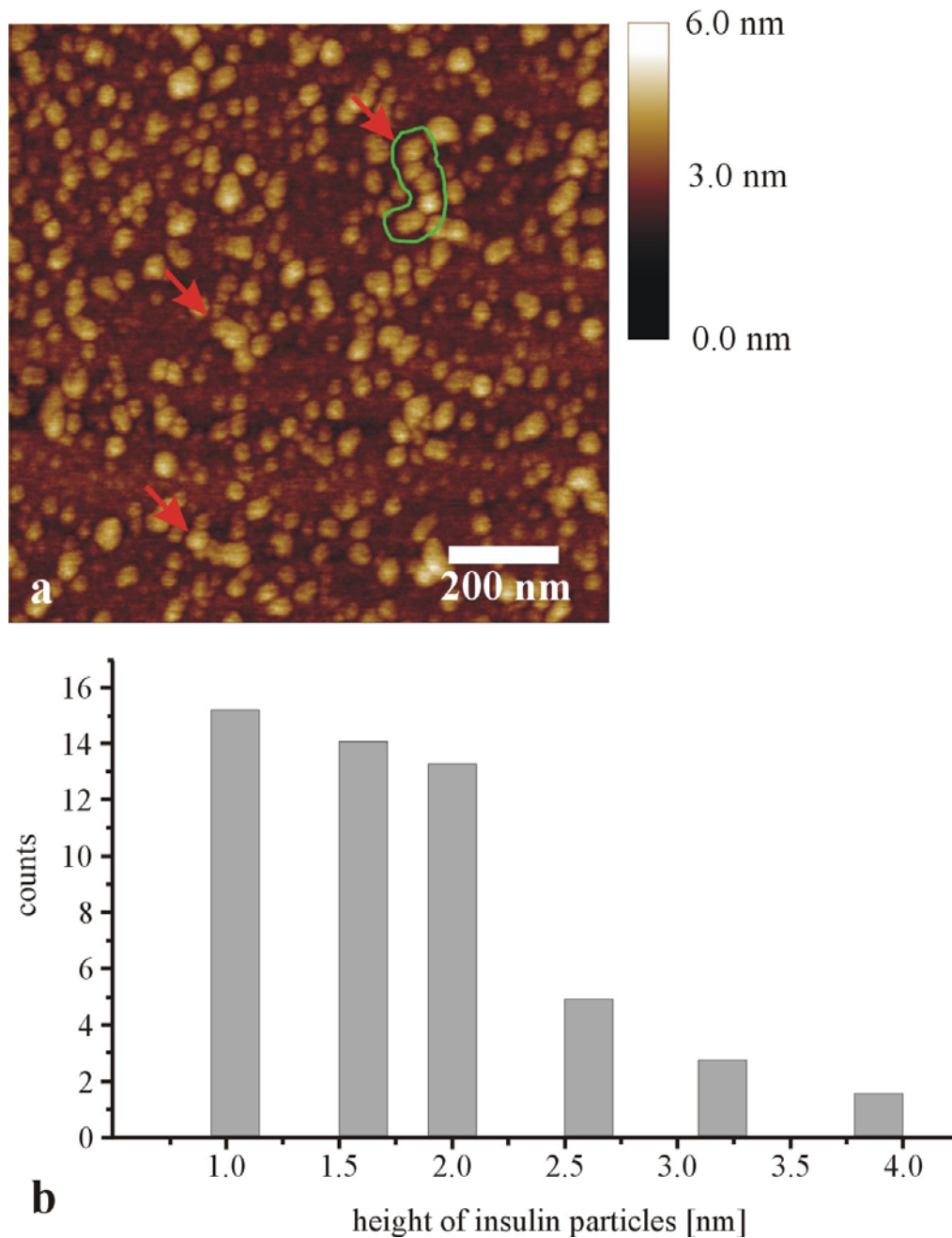


**Figure 4.3** (a) AFM height image of the early insulin aggregates formed during the first 30 s of incubation at 60 °C. The arrows mark the first elongated, prefibrillar loose aggregates. (b) Averaged size-distribution of the particles.

It is a well-established experimental fact that upon insulin fibrillogenesis the first to appear are thin elongated forms of (~ 1.2 ± 0.3) nm in diameter [Khurana et al., 2003], which are likely to consist of tubularly-stacked β-helices [Jiménez et al, 2002]. Such protofilaments merge and intertwist yielding thin fibrils, which are capable of further association and twining, finally producing mature amyloids. The driving force transforming destabilized protein molecules to protofibrils and protofilaments to fibrils arises from hydrophobic and electrostatic interactions. The same type of interactions plays a role in the lateral clumping of monomers/oligomers and fibrils. The compact mature fibrillar structures formed at the endpoint of the aggregation process may hence largely result from an effort to minimize the exposure of hydrophobic residues.

Such a hierarchical scenario of amyloidogenesis [Aggeli et al., 2001] has been observed for several proteins including $\beta_2$-microglobulin [Kad et al., 2003], α-synuclein [Khurana et al., 2003], yeast prion protein Ure2 [Jiang et al., 2004], and insulin [Bouchard et al., 2000; Jimenez et al., 2002; Khurana et al., 2003]. In this study, however, it is also observed, along the typical transient structural motifs, that lateral interactions, normally dominating at the later stages of fibrillogenesis and being responsible for the thickening of the fibers, may in fact play a role at the very beginning of the process, and lead to an alternative sub-pathway of amyloidal assembly.

## 4.1.2   Early Fibrillar Forms

Among the first fibrillar forms of insulin aggregates, which appear within the first 60 s of the incubation at 60 °C, few and relatively thick rod-like specimens can be seen, which are abundant at a later stage of the aggregation process (after ~ 5 min). An example shown in Fig. 4.4 consists of 4 cord-like subunits. The AFM image of the fibroid with a total length of (544 ± 12) nm may be interpreted as showing either a periodically twisted structure with a regular helical (right handed) pitch of (52 ± 2) nm or linearly-staggered elements, each (52 ± 2) nm long, constituting a longer topological block. On average, these fibrils are ~ 80 to 500 nm long and rather uniform in height, (4.4 ± 0.3) nm (the average is based on 20 measurements), which otherwise corresponds to the thickness of regular mature insulin amyloid fibrils [Khurana et al., 2003]. The 70 °C preparations yield populations of equally long, but (2.9 ± 0.6) nm or (6.5 ± 0.6) nm high seeds. In Fig. 4.4a, the helical groove-depth is (1.7 ± 0.14) nm.

The height values corresponding to the three outer subcords seen in Fig. 4.4a are $(7.2 \pm 0.29)$ nm (left), $(7.9 \pm 0.37)$ nm (central), and $(5.3 \pm 0.25)$ nm (right).
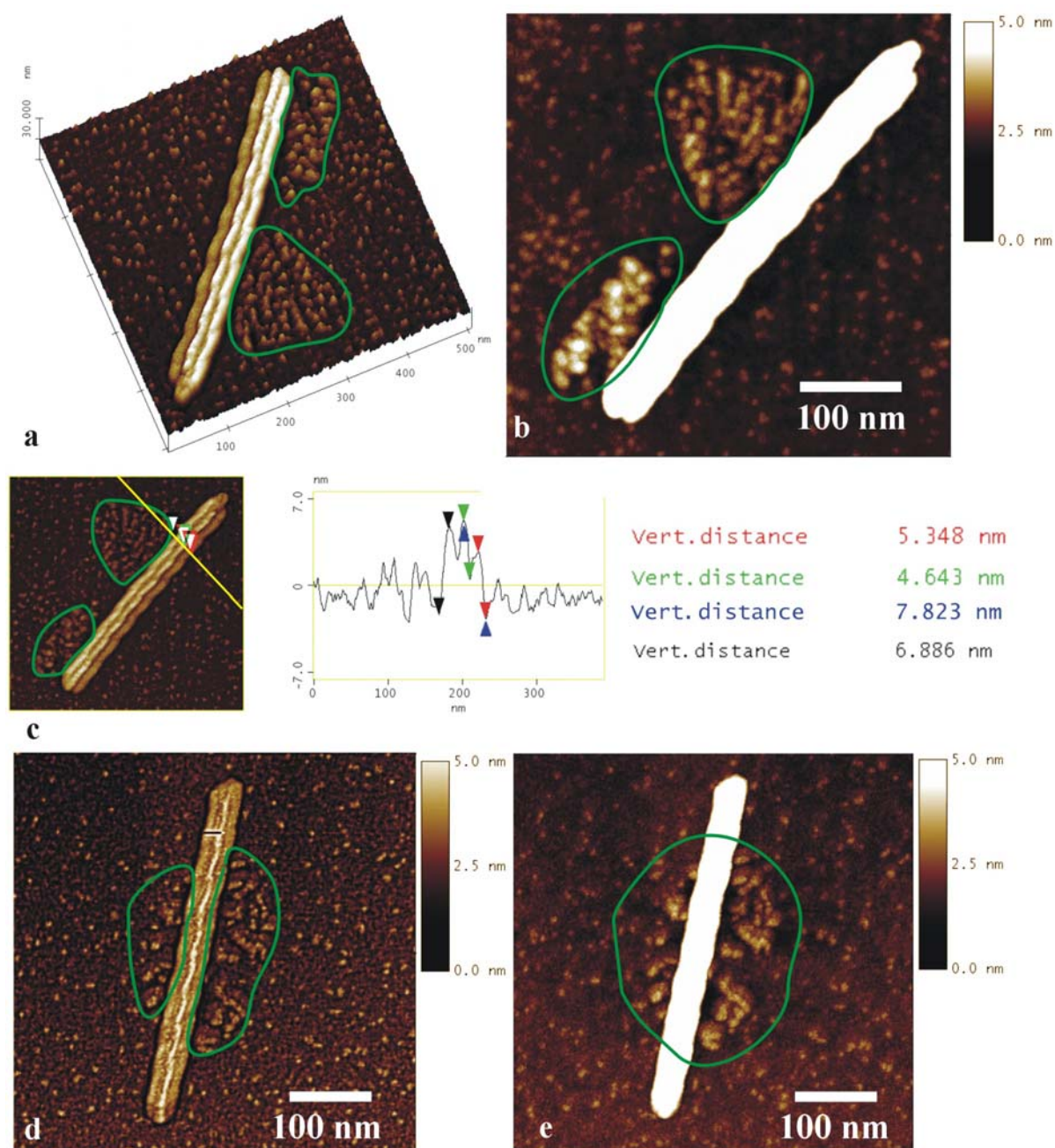


**Figure 4.4** First rod-like insulin aggregates formed after 1 min at 60 °C (a and b). An example illustrating the filament height determination (c). Particles of prefibrillar aggregates tend to cluster in the proximity of the early fibers (b, d, and e) - marked by green lines.

A thorough examination of these initial forms is of interest, as in this early timescale of the aggregation process, both nucleation and elongation processes coexist and may influence each other. Interestingly, a closer scrutiny of the insulin aggregates obtained after 1 min of incubation at 60 °C indicates that clusters of swollen insulin particles tend to align within the

immediate vicinity of the early fibers (Fig. 4.4 b, d, and e). This suggests that the once-formed fibroid enhances - through lateral interactions - formation of subsequent fibers. When attempting to elucidate a plausible mechanism of formation of these early, yet relatively thick fibrils, it must be taken into account that the fibril ends are not frayed, i.e., the ingredient subcords are of equal length and are evenly aligned. Such an effect would be quite improbable and surprising, meaning that the fiber is produced by a spontaneous association of several free pre-existing protofilaments of the same length. On the contrary, it seems that a single protofilament may act as a lateral template or scaffold for small insulin particles, which would constitute a neighboring subcordlike features in the fibril shown in Fig. 4.4a. This "protofilament + monomers/oligomers" scenario is an alternative pathway to the otherwise dominating "protofilament + protofilament" way for the lateral growth of the protein fibrils.
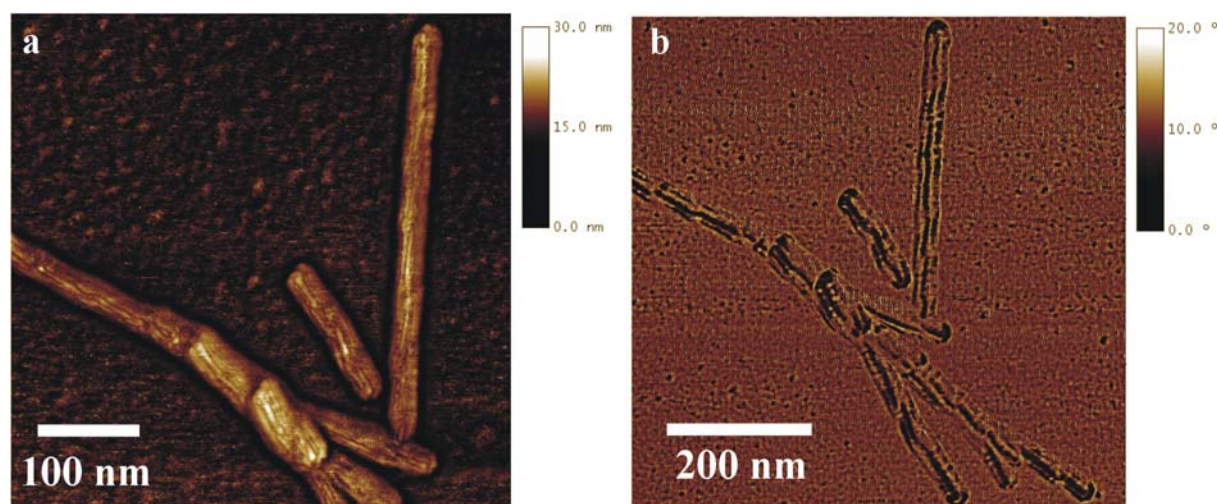


**Figure 4.5** Height (a) and phase-shift (b) AFM images of a cluster of insulin aggregates formed after 5 min of incubation at 60 °C.

In Fig. 4.5a, height and in Fig. 4.5b, phase AFM images of the morphological features obtained after 5 min of the 60 °C incubation are displayed. The fibers are considerably thicker (the average diameter judged from the height data is $(9.3 \pm 0.7)$ nm) and their surface appears to be structured with 6 - 8 subcords aligned in parallel, which are likely to be protofilaments of an individual height of $(\sim 2.0 \pm 0.5)$ nm. Therefore, depending on internal packing, it can be approximately estimated that the thick fiber consists of over a dozen of laterally associated protofilaments.

Phase AFM (Fig. 4.5b) enables probing the relative hardness of the imaged object. This approach has been employed here to deconvolute the fibrillar structure shown in Fig. 4.5a into ingredient subcords of various packing; four or six of which are apparently

distinguishable on a single fiber surface. Although it is known that parts of the insulin chain, such as the C-terminal of the B-chain, are not expected to participate in the tight intra- and interfibrillar packing (therefore giving rise to loose and soft elements protruding alongside the protofilament [Jiménez et al., 2002]), it may be as well the different degrees of packing of protofilaments in the core of the fiber and on its surface that evoke this effect.

The prolonged 10-min incubation at 60 °C promotes further elongation of the fibers even up to 2.8 µm. The fibrils grown at 70 °C on the same timescale are longer (up to 5.5 µm) and approximately three times more abundant (25 particles at 60 °C versus 71 particles per unit surface area at 70 °C). Apart from the faster kinetics, the increased temperature leads to a more complex morphological variability: long straight rods, twisted ribbon-like structures, rod bundles and rope-like structures become prominent in the corresponding AFM data. Highly twisted fibrils, along with the species of negligible helicity, have been reported earlier for different insulin amyloid preparations [Nielsen et al., 2001c]. Figure 4.6a shows a representative example of the morphological variability in fibrillar insulin aggregates grown for 10 min at 70 °C. The features can be classified as parallel tubular fibers, twisted ribbon-like structures, rod bundles and rope-like textures. The seven distinguishable fibers seen in this picture were inspected in a detailed manner: four of them are tubular or ribbon-like double-corded (indicated by the red, blue, yellow and turquoise arrows) and three are more or less twisted (marked with the green, white and pink arrows).

Another difference between the 10-min insulin aggregate preparations at 60 and 70 °C concerns diversely convoluted shapes, whose presence is more pronounced in the latter case. These forms vary from slight bends over double turns to semicircles of variable radii of curvature (not smaller than 250 nm). In the 70 °C samples, semicircles and sinusoidal bends are observed. Further experiments (compare chapter 4.2) revealed that the pressure-induced circular amyloid of insulin consists of several loops of a thin and untwisted form, possibly a single protofilament [Jansen et al., 2004]. It may be therefore hypothesized that the protofilament structure gives rise to an inherent mechanical strain, which may be relaxed either by a collective twisting of associated protofilaments or a curling of those. The observed tendency of untwisted lateral agglomerates (Fig. 4.5) to transform co-operatively into hierarchically twisted features (Fig. 4.6) may be a consequence of a more effective relaxation of the mechanical strain (at a similar entropic cost of the assembly).
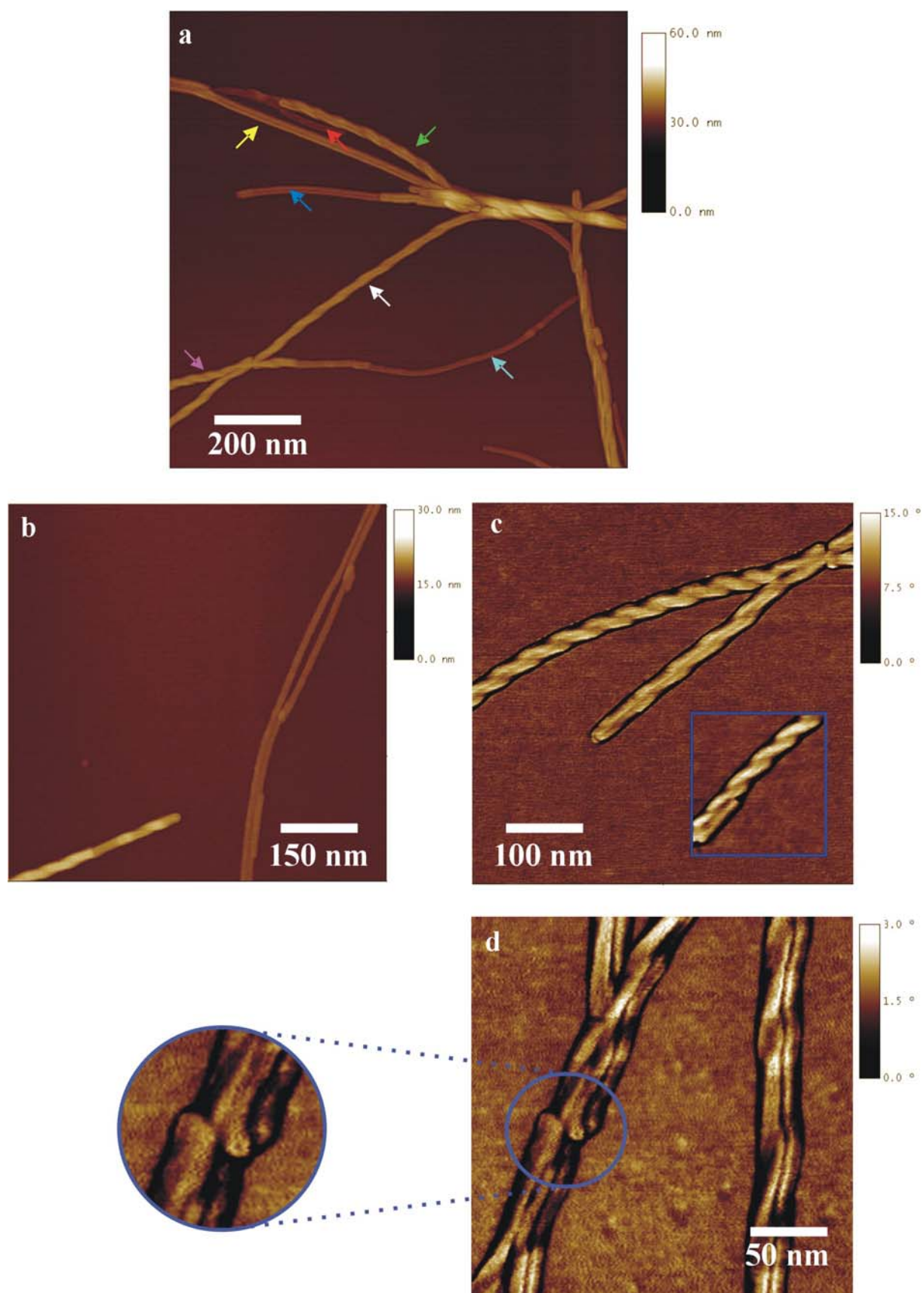
**Figure 4.6** Morphological variability in insulin amyloid samples obtained after 10 min of incubation at 70 °C (a - c). Fibril diameters: $(4.2 \pm 0.20)$ nm (red arrow), $(5.5 \pm 0.57)$ nm (turquoise), $(7.2 \pm 0.50)$ nm (blue), and $(9.0 \pm 0.36)$ nm (yellow). (d) Image of fibers obtained through 10 min of incubation of native insulin at 60 °C.

### 4.1.3   Structural Polymorphism of Mature Fibrils

Figures 4.6b and c represent other morphological motifs often found in the 10 min insulin aggregate preparations at 70 °C: for example, two laterally connected double-stranded fibers of equal height of 3.1 nm (Fig. 4.6b) splitting over a certain distance, or, as shown in Fig. 4.6c, two highly twisted fibrils with different morphologies overlapping each other. It appears therefore that even for a homogeneous insulin sample undergoing a controlled temperature treatment, there is still more than one kind of superhelical assembly of protofilaments. In Fig. 4.6d, the end of one thread (indicated by the blue circle) seems to grow out of the image plane facing vertically upwards and making the subfibrils interior accessible to the AFM tip. The zoom-in reveals the entrance to a fibrillar canal of ~ 1 nm diameter. This, in fact, is a direct evidence supporting the model of amyloid fibrils as waterfilled nanotubes [Perutz et al., 2002].

The juxtaposed differences between the populations of fibers grown at 60 and 70°C clearly concern not only the rate of the aggregation process, but also different quaternary folds. Although different distribution profiles of fibrillar features may still be explained in terms of kinetic effects (temperature may differently affect the kinetics at various stages of the assembly, effectively marginalizing certain sequential processes), the higher temperature may also have a more direct effect on amyloidogenesis, for instance by increasing the thermal energy of the interacting molecules and hence causing the alignment of protofilaments to become less accurate. Such unspecific effects may contribute to morphological differences in any protein amyloid samples induced at high temperature. However, the morphological variation herein observed after increasing temperature bears a more profound meaning in light of the ongoing debate as to the identity of an aggregation-prone protein conformation (completely unfolded or partly unfolded protein) and the study of our research group, showing that under similar conditions bovine insulin is substantially more unfolded at 70 than at 60 °C [Dzwolak et al., 2003]. According to the polymeric paradigm [Fändrich and Dobson, 2002] of amyloidogenesis and the importance of backbone interactions implicated therein, the more the native structure becomes distorted (and the protein backbone becomes exposed), the higher is the chance that the protein enters the amyloidogenic pathway. Although considerable evidence suggests that only partial destabilization of insulin is the prerequisite for its aggregation [Ahmad et al., 2003], the present data indicate that additional temperature-induced destabilization may be a factor that broadens the range of accessible fibrillar forms.
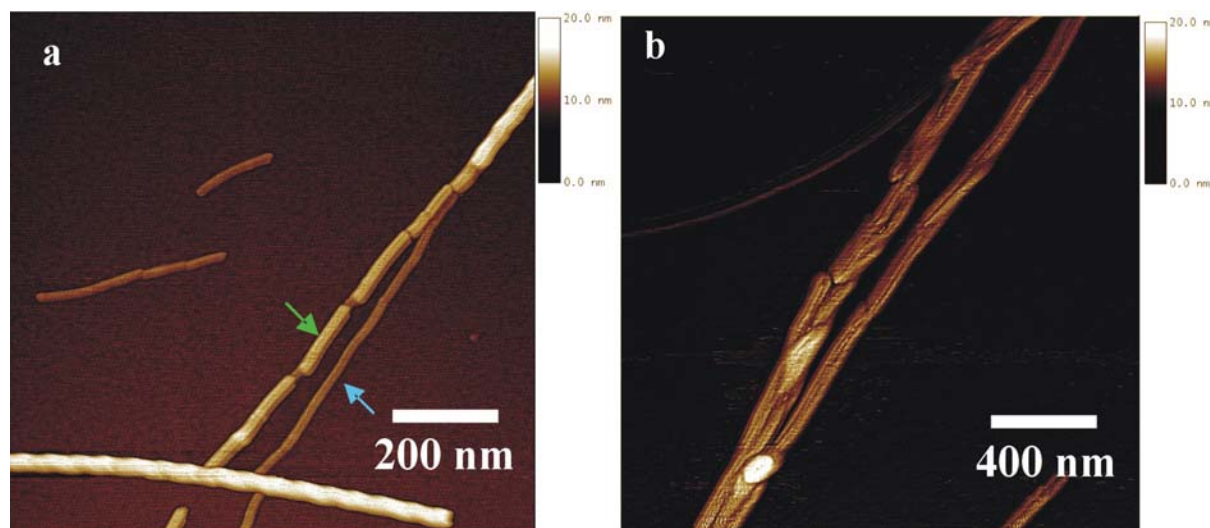
**Figure 4.7** AFM images of mature insulin amyloid fibrils grown at 70 °C for 20 min (a) or 30 min (b).

An interesting aspect of the late stages of the amyloidogenic assembly is provided by AFM data on insulin samples heated at 70 °C for 20 (Fig. 4.7a) and 30 (Fig. 4.7b) min. The two fibers marked with the green and blue arrows are of comparable height of $(6.5 \pm 0.5)$ nm. The fiber marked with the green arrow appears to consist of joined segments $(\sim 153 \pm 8)$ nm long. The fiber height at the intersegment joints is only $(3.4 \pm 0.2)$ nm. In the vicinity of this chain-like fiber, there are single amyloid stretches of $(155 \pm 5)$ nm length, which is in excellent agreement with the unit size of the chain. Another interesting object visible in Fig. 4.7a is a pair of such units. This data may be interpreted as yet another way of assembling amyloid fibrils through chainlike queuing of preformed discrete amyloidal subunits. Fig. 4.7b shows fibrils found in insulin samples incubated even longer at 70 °C. The fibril gains a braid-like outlook with an increased average diameter of up to $(9.6 \pm 0.8)$ nm. The more laterally expanded architecture with a regular repeat of roughly 150 nm suggests an event of lateral binding of the 150 nm long segments alongside the fiber.

Under these experimental conditions, no prominent qualitative changes in the elementary morphological folds were observed at times of incubation exceeding 1 h. The full fibril length is not definable any longer for dimensions exceeding the maximum (16 µm) scan size of the apparatus. In general, the lateral binding seems to be highly variable. A new aspect is the formation of so-called "superfibrillar" aggregates as shown in Fig. 4.1g: 5 (often also 10 - 15 or sometimes even more than 20) fibers with diverse characteristics (like tubular, twisted or undulated forms) and diameters generate both tight- and loose-plait ropelike aggregates (diameter: 5 - 25 nm) with endings fraying in single fibers.
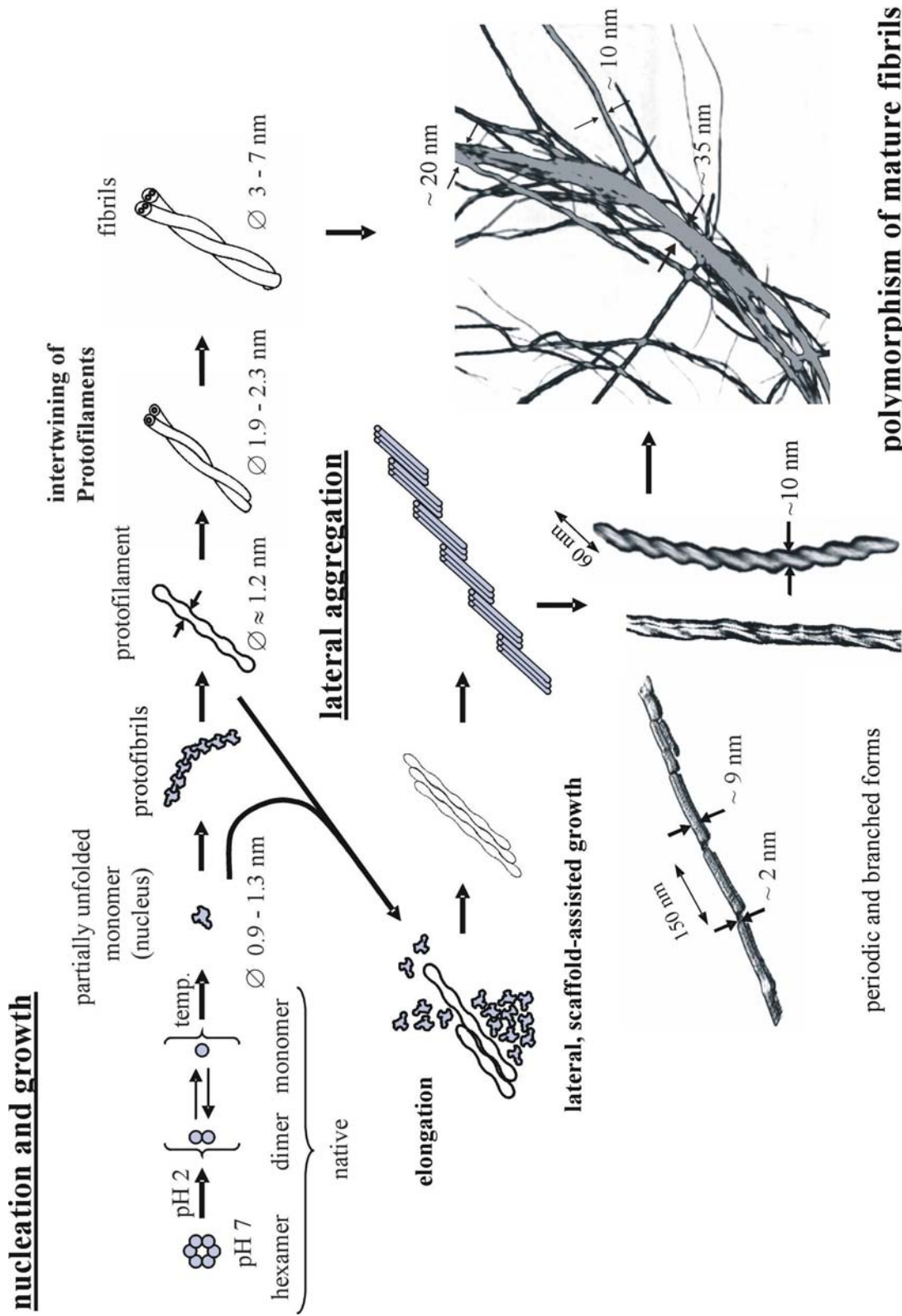
**Figure 4.8** Generalized scheme of the multipathway fibrillization of insulin. The lateral interaction of early, prefibrillar forms with protofibrils and protofilaments, followed by the lateral association of protofilaments, is a self-assembly route alternative to the hierarchical intertwining of protofilaments. The observed polymorphism of mature amyloid samples suggests that, under the given conditions, insulin fibrillization proceeds via both pathways.

In contrast to the 60 °C incubation, in which an increase of the fibril concentration of approximately 1/4 (235 fibers versus 325 fibers) can be determined within 1 day and 1 week, a noteworthy change of the fibril concentration at 70 °C in the same period does not take place. This suggests that the aggregation process is essentially completed after 1 h at 70 °C. Interestingly, in these two samples (1 h and 1 week incubation at 70 °C) the fibers do not crisscross. In fact, there are large meander-like areas in which they have nearly the same orientation. This supports the earlier proposed mechanism of the early fibrils shown in Fig. 4.4 acting as lateral scaffolds for the subsequent formation of fibrils, which at the same time ensures an ordered, parallel organization of large domains of fibrils.

The insulin amyloidogenesis in vitro reported herein, induced by en masse destabilization of native dimers, proceeds through a multipathway assembling scheme, which employs - on one hand - the hierarchical intertwisting reported earlier, and on the other hand employs lateral interactions between single particles and fibrils leading to larger domains of parallel-aligned features (Fig. 4.8). Such an alternative scenario of fibrillar self-assembly may in the end lead to morphologies with screw-like outlook, otherwise postulated to result from the hierarchical twisting.

## 4.2   Insulin Fibril Formation under High Hydrostatic Pressure

In this study samples of insulin aggregates obtained under atmospheric pressure, at 750, 1200 and 1500 bar were subjected to analysis by AFM (Fig. 4.9). While the unpressurized insulin gives typical straight unbranched fibrils, the protein forms amyloids of quite a different morphology under pressure.
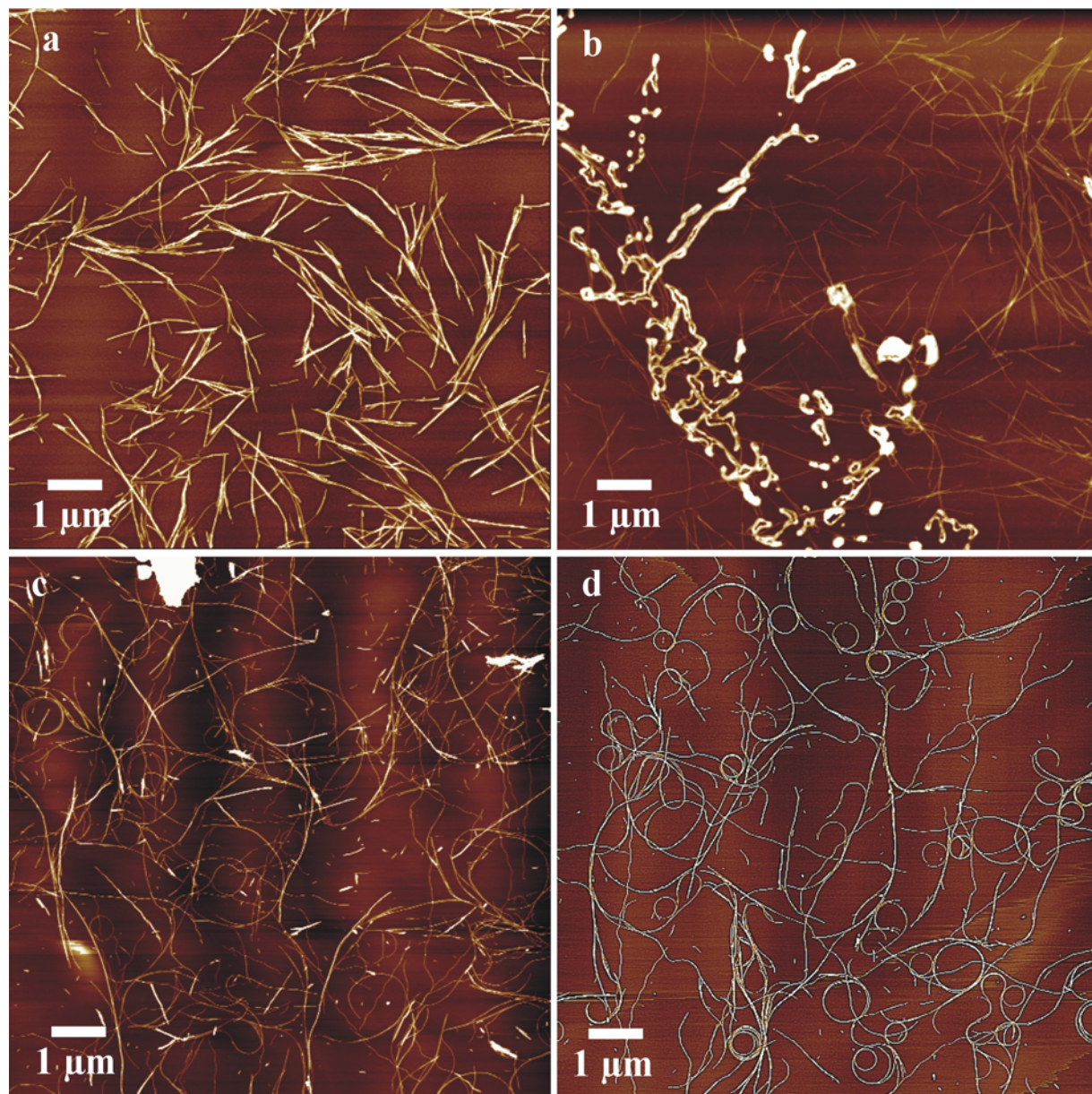


**Figure 4.9** AFM images of insulin fibers and aggregates, grown at ambient pressure (a), 750 bar (b), 1200 bar (c), and 1500 bar (d).

Unexpectedly, novel thick (30 - 65 nm in height), loop-shaped (largely distorted and stretched) aggregates (Fig. 4.9 b) at 750 bar and circular (Fig. 4.9 d) fibers at 1500 bar were

prevalent. At 1200 bar, apart form ordinary fibrils, both forms - but in a less pronounced manner and quantity - occurred. In this intermediate pressure regime none of the novel species seemed to be preferentially promoted. Fig. 4.10 shows a stepwise zoom-in of the 750 bar grown loop-shaped aggregates. Herein, two types of clustered amorphous aggregates were distinguishable: small doughnut-shaped ((150 ± 20) nm in diameter) forms and large loops (200 nm - 3.5 µm distance between the most remote points), which for the most part exhibit irregular and caved-in morphologies. Since pressures up to 500 bar (see appendix, Fig. 7.2b) only retarded ordinary fibrillar growth, but did not promote such amorphous aggregates, there may exist only a small pressure-window allowing their formation, possibly induced by pressure exposure of hydrophobic residues. Similar aggregate forms occur under the influence of certain cosolvents (cf. chapter 4.3).
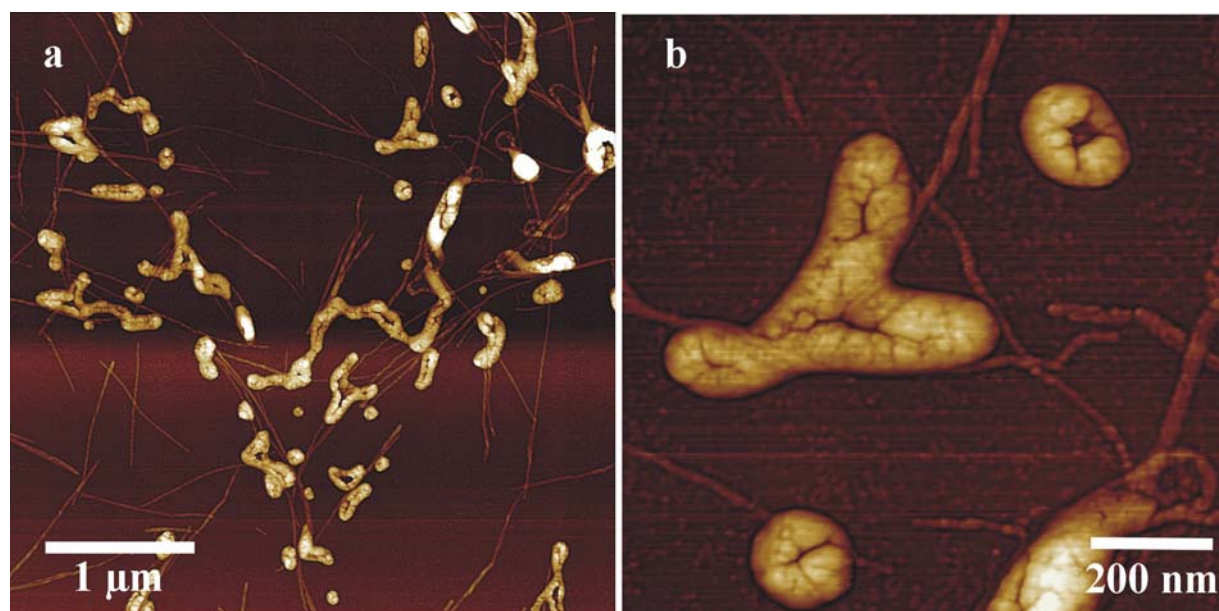


**Figure 4.10** Doughnut- and loop-shaped amorphous insulin aggregates grown at 60 °C and 750 bar after 20 hours of incubation (a, b). (b) Zoom-in of the upper right quarter of (a).

Most of the circular insulin fibrils shown in Fig. 4.9d exhibit diameters of 340 - 420 nm. Although larger ring-shaped aggregates were present, they were rare and mostly distorted. The conditions evoking the circular morphology do not induce pronounced changes in the secondary fold that would be detectable in infrared spectra. Fourier transform infrared (FTIR) spectra of the circular amyloid [Jansen et al., 2004] were similar to those of most ambient pressure insulin amyloid preparations in water [Nielsen et al., 2001c]. High-resolution AFM scans permitted a more thorough analysis of the structural features of the circular amyloid (Fig. 4.11a and b). The most abundant, roughly 400 nm large circles are

accompanied by semicircles and "cracked" rings of approximately the same radius. It remains unclear whether these structures are indeed disrupted regular circles, or rather early, incomplete fibers, whose growth was stopped in the experiment. Shorter, bent fibers of a length of approximately 20 - 100 nm were present in all samples containing the circular forms (Fig. 4.9d, and 4.11a and b). Such short stretches have also been observed to form when mature fibers are subjected to repetitive freeze-thawing [Nielsen et al., 2001c] or sonication, and are expected to become very effective seeds both *in vitro* and *in vivo* [Saborio et al., 2001], due to the shear multiplication of "sticky fiber ends". Additionally performed experiments aiming to study the effect of pressures of up to 4500 bar on the topology of linear fibers grown under ambient pressure conditions revealed no change of their topology as expected owing to the densely packed, non-elastic nature of the straight fibers (see appendix, Fig. 7.2a).
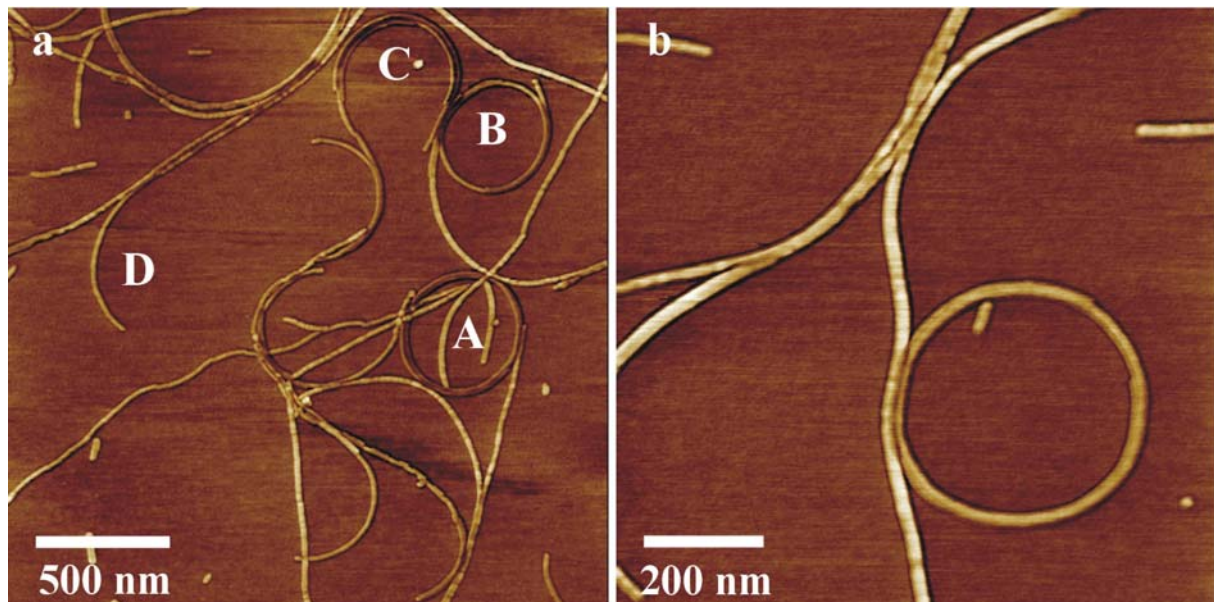


**Figure 4.11** Typical morphological features of insulin amyloids grown at 1500 bar. (a) Closed (A and B), open (C), and partly bent (D) fibers appear. (b) The most abundant circular form has a diameter of 340 - 420 nm and is accompanied by bent stretches of fibrils that are typically 20 - 100 nm long.

Fig. 4.12a shows a magnified, high-resolution AFM image of a typical amyloid "circle". The ring of 340 nm internal diameter and 56 nm thickness is, in fact, a spiral comprising roughly seven coaxially folded unitary loops, visible in Fig. 4.12a by fine grooves. The separation between the grooves is 7 nm while the height is 2 nm (Fig. 4.12b), suggesting that a single circular loop as identified in this AFM image can still consist of two to four protofilaments.

High pressure generally promotes processes leading to a volume contraction and disfavors those accompanied by a volumetric expansion. Whereas high pressure retards insulin aggregation, the protein nevertheless slowly forms amyloid of an unprecedented circular morphology. Considering that the fibers are likely to be filled with water [Perutz et al., 2002], an additional volume contraction may stem from a more effective packing around some amino acid residues within the fiber and a resulting global reduction in void volumes.
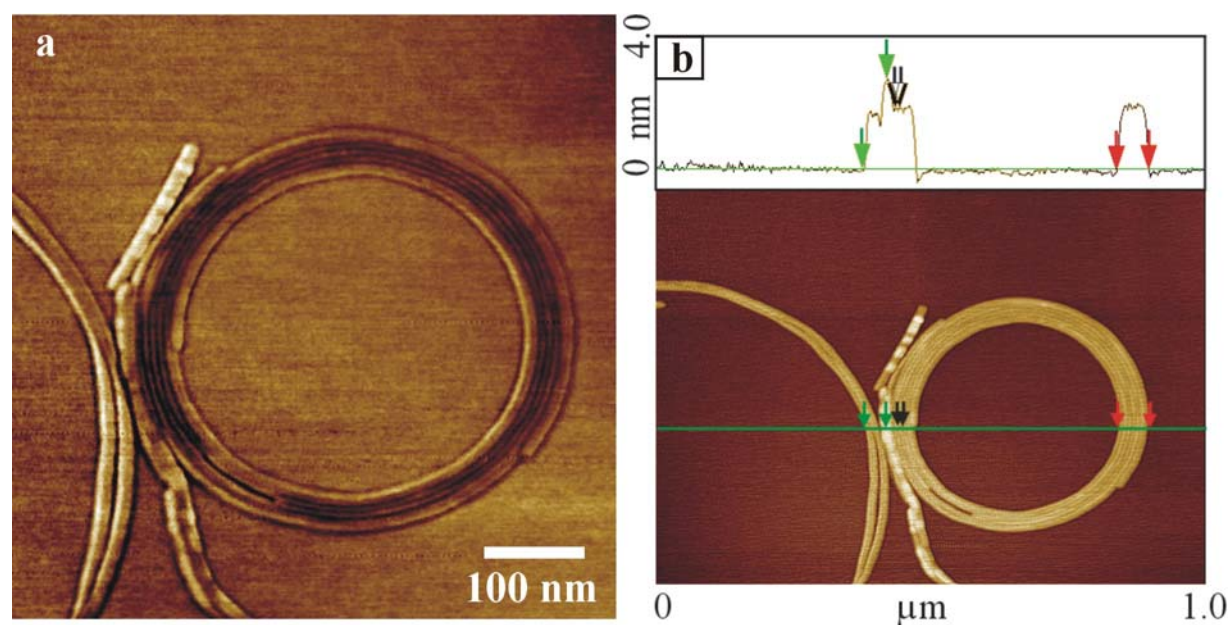


**Figure 4.12** High-resolution AFM images of the circular amyloid reveal its ultrastructural features. (a) Enlarged surface image of the spirally bent amyloid. (b) The corresponding AFM height profile. Given the large difference in vertical and horizontal scaling (4 nm versus 1000 nm), the amyloid fiber is, in fact, quite flat.

Furthermore, the highly regular circular fold of pressure-grown amyloid suggests that there may be an anisotropic distribution of such void volumes in the "ambient-conditions" straight insulin fiber. Therefore, at high pressure, the fiber tends to bend in one direction only throughout the elongation process. This claim is supported by a very recent study proving that the insulin Asn A21 residues evenly populate two different structural environments within the amyloid, implying two different packing modes along the fiber [Nilson and Dobson, 2003]. The high degree of uniformity of amyloid fibril morphologies, regardless of the length of a polypeptide chain and amino acid composition, makes one expect some packing incompatibility of side-chain residues within the fibrillar structure. This is likely to cause "periodic" void volumes along the fiber. The aggregation-preventing pressure effect may be overcome if the structural transitions occurring on the early aggregation pathway permit a collapse of these void volumes. This would give rise to morphologies reflecting a distribution

of these void volumes along the fiber. While this may give clues to the amyloid structure and become a testing ground for some amyloid models [Aggeli et al., 2001; Jiménez et al., 2002], it may also raise new questions as to the possible undesirable biological activity of protein aggregates induced by high-pressure food processing.

## 4.3   Cosolvent-Perturbed Insulin Self-Assembly

The AFM studies reveal that the structural variations of the mature aggregates grown under different solvent conditions manifest in characteristic morphological features. Figs. 4.13 to 4.16[4] depict typical morphological motifs that occur with varying cosolvent concentrations. The unbranched fibrillar morphology of insulin aggregates grown in the presence of 5 wt % glycerol (Fig. 4.13 a and d) hardly differs from that of typical water-grown fibrils of the same age (Fig 4.13 f), but their quantity is reduced. However, the fibrils grown in 20 wt % glycerol show extensive buckles and exhibit a rather "cracked" morphology, wherein the fibrillar architecture (4 - 6 filaments) is maintained (Fig. 4.13 b and e). Regarding to their quantity, Fig. 4.13b indicates a decrease in the amount of mature fibrils in comparison to Fig. 4.13a. A further increase of the glycerol concentration to 40 wt % still evokes fibrillar - but more flexible - material, the quantity of which, however, is much smaller compared to that at lower glycerol concentrations (Fig. 4.13 c). Notably, the vast majority of insulin remains unaggregated (Fig. 4.13 c, inset) even after six days, which gives a clue as to the retarded aggregation kinetics with increasing glycerol content. The average size of the unaggregated insulin particles in the presence of glycerol is $(0.7 \pm 0.2)$ nm (possible differences in the dimensions within the glycerol concentration series turn out to be smaller than the error range), which is slightly smaller than the smallest insulin particles found in pure water (cf. chapter 4.1: particle height is 1.1 nm). Also, the fibrils grown under the influence of glycerol appear to be slightly more compact, as judged by their average diameter of $(2.7 \pm 0.3)$ nm, than the thinnest water grown fibers (cf. chapter 4.1: $(2.9 \pm 0.6)$ nm). Consistently, these results are in agreement with data obtained by CD spectroscopic and fluorescence anisotropy studies carried out in our research group [Grudzielanek et al., 2005].

In contrast to the monotonic concentration effects on the aggregate quantity and morphology as seen with glycerol, the addition of as low as 5 wt % of EtOH triggers the appearance of bent and circular fibrils, the diameters of which are typically 750 - 800 nm (Fig. 4.14 a). Compared to water-grown fibrils (Fig. 4.13f), an increase of the amount of fibers is revealed. The amount of circular forms is reduced in 20 wt % EtOH in favor of amorphous material (Fig. 4.14 b), and completely vanishes at 40 wt % EtOH, where clusters of amorphous aggregates prevail besides ring-shaped amorphous specimens with diameters between 50 and 170 nm and heights between 8 and 22 nm (Fig. 4.14 c). An additional experiment performed at 70 wt % EtOH even yields doughnut shaped forms with diameters

---

[4] Due to their large size, the figures are shown at the end of this chapter on pages 70 to 73.

up to ~ 700 nm and heights of ~ 300 nm (Fig. 4.14 d; for additional images see appendix, Fig. 7.3).

Similar, but less pronounced trends are observed for the aggregates in TFE-containing solutions. Straight fibrils dominate besides a few circularly bent specimens at 5 wt % TFE (Fig. 4.15 a), the fraction of which slightly increases in 20 wt % TFE (Fig. 4.15 b). Rarely, amorphous agglomerates of insulin oligomers with heights between roughly 1.3 and 4 nm also appear. In a complementary fashion, few single fibrils and filaments are embedded in an amorphous, cocoon-like matrix at 40 wt % TFE (Fig. 4.15 c and Fig. 4.16 b), which, with respect to morphology, corresponds to the situation observed in 20 wt % EtOH (Fig. 4.14b and 4.16a). According to the average heights of EtOH and TFE-grown fibrils, no significant differences to water-grown fibers are observed. However, as a result it can be stated that at high ethanol or TFE concentrations clusters of amorphous aggregates are the most likely product of insulin association. This is in excellent agreement with the non-monotonic solvation scenario recently proposed for these systems [Grudzielanek et al., 2005; Dzwolak et al., 2004b]: At low concentrations, the monoalcohols facilitate the formation of aggregation-prone intermediates by destabilization of the native assembly showing a reversal from a rather kosmotropic to a merely chaotropic solvational behavior due to micelle-like clustering of alcohols above a critical threshold concentration (15 wt %; [Cinelli et al., 1997]). This may explain the accelerating effect on ordered fibrillation at low and the inhibitory nature at high concentrations of EtOH and TFE, ultimately leading to amorphous aggregation.

Amazingly, the doughnut-shaped species obtained upon addition of high alcohol concentrations resemble the amorphous rings occurring at 750 bar pressure (cf. chapter 4.2). Furthermore, the circular shaped fibers triggered at 1500 bar pressure as well as at 5 wt % EtOH only differ in their average diameters of ~ 380 nm (pressure grown) and ~ 750 nm (5 wt % EtOH), respectively, and in the less distorted shape of the pressure-grown compared to the alcohol-grown circles (rather elliptical than circular). This suggests that both, the impact of pressure and cosolvents facilitate similar self-assembly pathways for insulin.
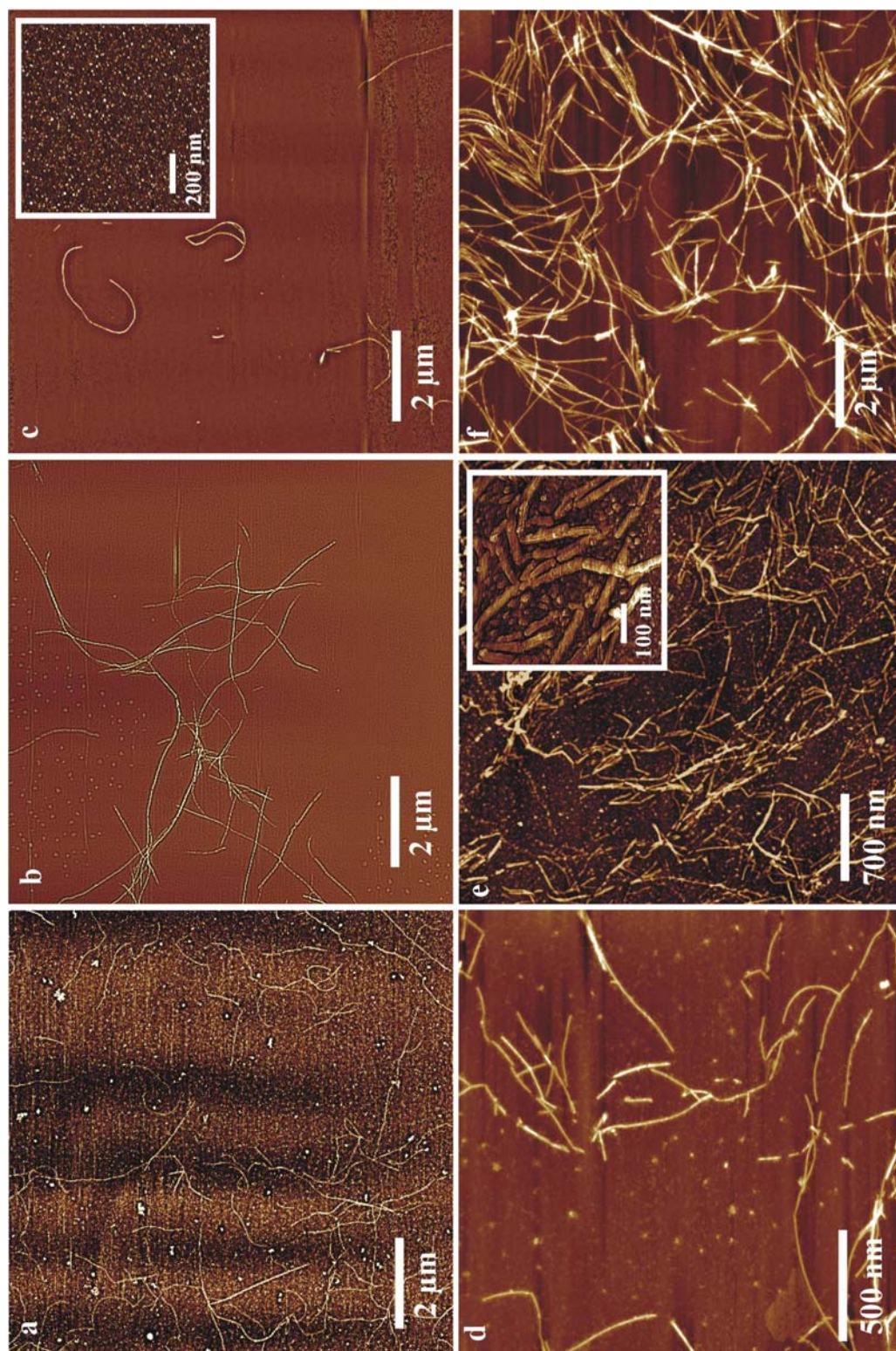
**Figure 4.13** AFM images of 0.1 wt % insulin, aggregated at 60 °C for 6 days in 5 wt % (a and d), 20 wt % (b and e) and 40 wt % (c) glycerol. The reference sample of water-grown fibers incubated at 60 °C for the same period is shown in (f).
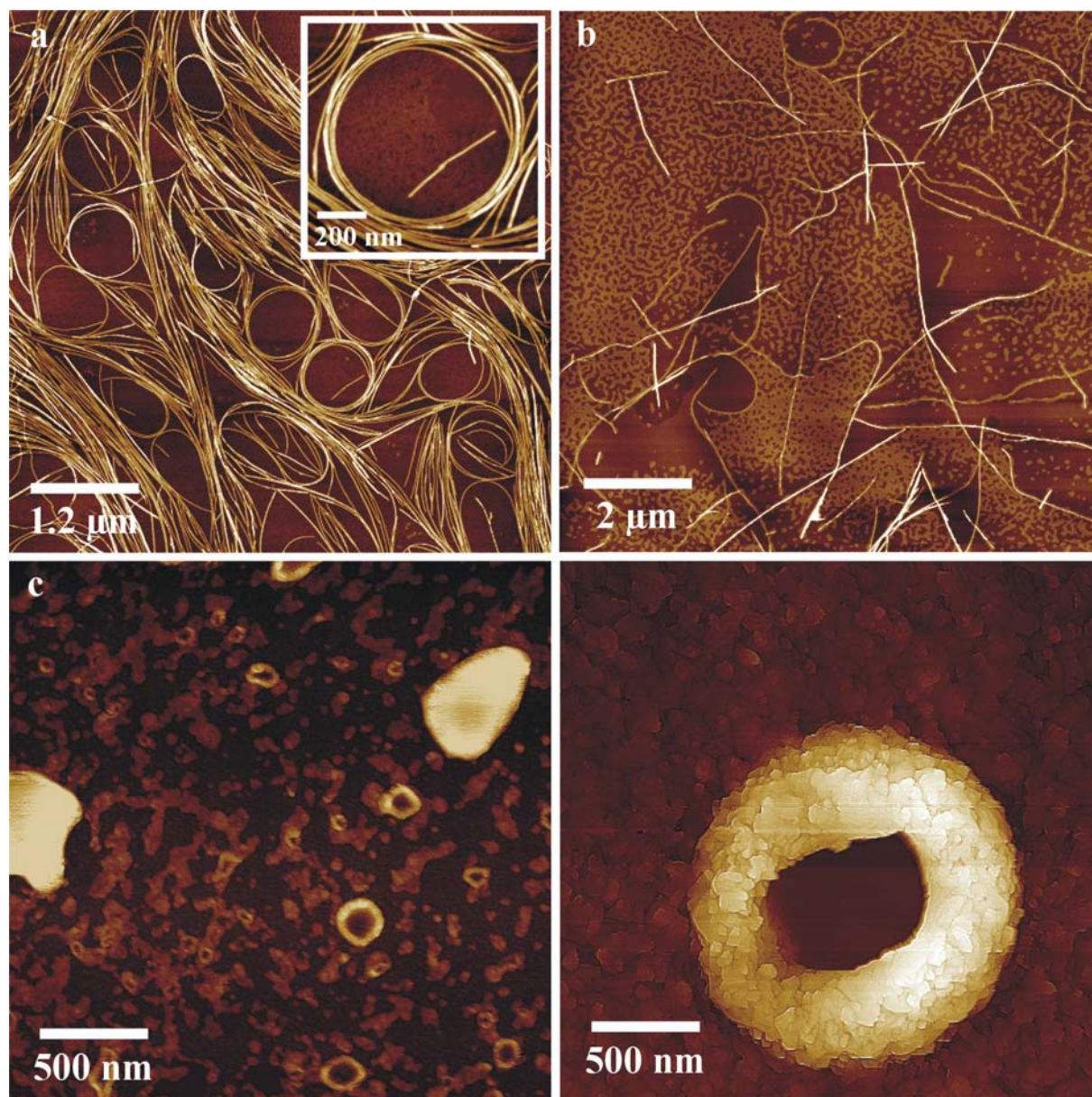
**Figure 4.14** AFM images of 0.1 wt % insulin, aggregated at 60 °C for 6 days in the presence of a) 5 wt %, b) 20 wt %, c) 40 wt % and d) 70 wt % ethanol.
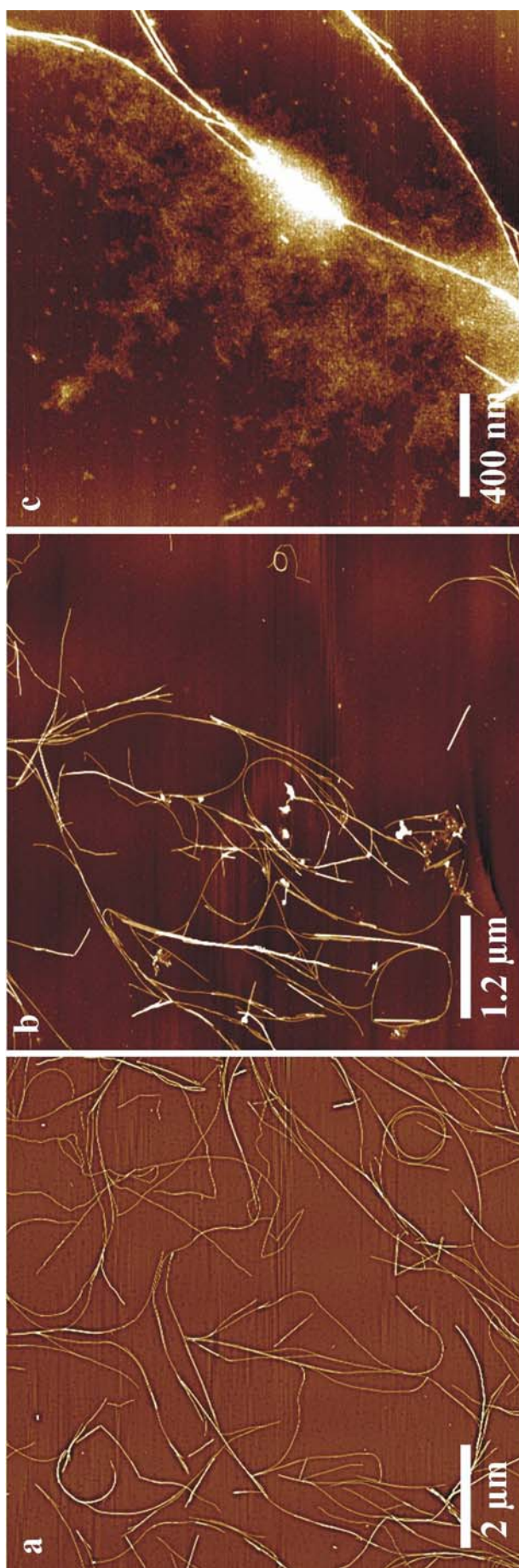
**Figure 4.15** AFM images of 0.1 wt % insulin, aggregated at 60 °C for 6 days in the presence of a) 5 wt %, b) 20 wt % and c) 40 wt % TFE, respectively.
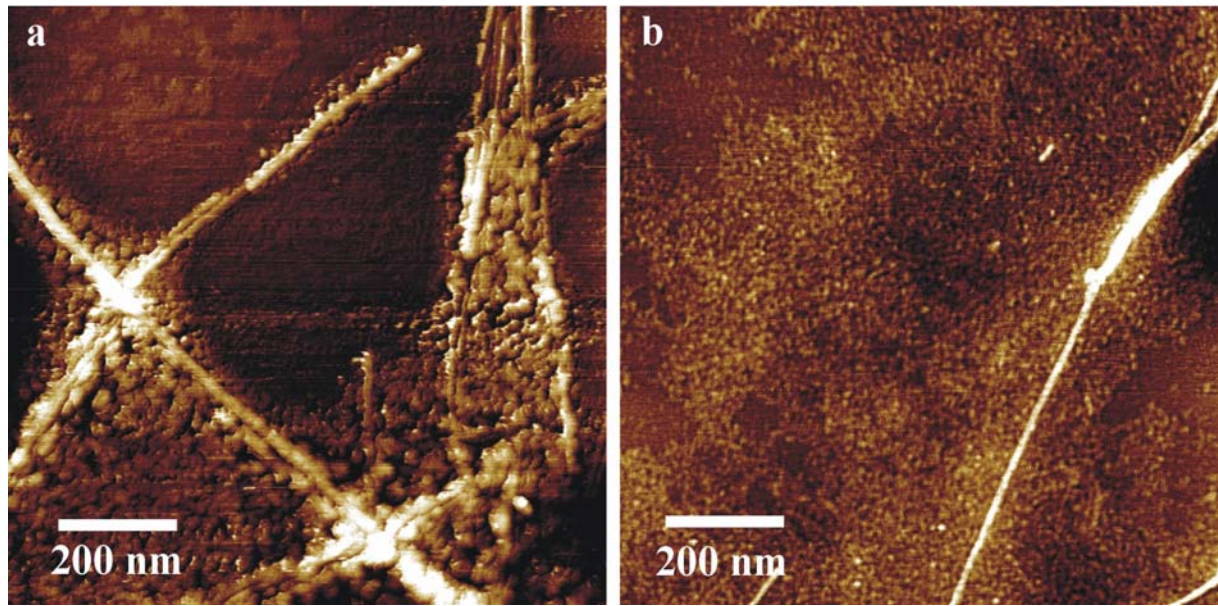
**Figure 4.16** AFM images reflecting in each case a zoom-in of a) Fig. 4.14 b with 20 wt % EtOH grown insulin aggregates, and of b) Fig. 4.15 c with 40 wt % TFE-grown insulin aggregates, respectively. Both pictures exhibit corresponding topological motifs of single fibrils embedded in an amorphous, cocoon-like matrix.

## 4.4   Seeding and Cross-Seeding Experiments with Insulin

Since fibrillar morphology is the most tangible aspect of conformational variations, which are expected to underlie the strain phenomenon, high resolution AFM as a probe differentiating between diverse types of amyloidal architectures is applied in this study.

Depending on the solvent conditions, the amyloidogenesis of insulin has been shown to result in distinct fibrillar morphologies. Therefore, seeding and cross-seeding of native insulin in different solvation scenarios is carried out and inspected with AFM. Fig. 4.17 presents images of the fibrils formed at 25 °C by seeding of insulin dissolved in water, or insulin, dissolved in 20 wt.% EtOH (pH = 1.6), with sonicated fibrils pre-formed spontaneously through an incubation of unstirred protein solutions for 24 h at 60 °C. The fibrils formed at 60 °C in water are long, straight and unbranched with heights of 4 - 5 nm (Fig. 4.17b). In the presence of 20 wt % EtOH, thinner (max 1.8 nm in height), and curved forms (partially S-shaped) prevail. Once formed, either type is stable and does not change its outlook upon transfer to an alternative environment. Seeding of unstirred protein solutions (either in water or in 20 wt % ethanol) was carried out for 24 h at 25 °C. The images of daughter fibrils in Fig. 4.17 convey a clear proof that the homogenously seeded amyloid fibrils (a, b), i.e. grown under solvent conditions corresponding to the preparation of the zero-generation fibrils, retain the original template morphologies. Interestingly, according to the cross-seeding data (c, d), the type of template, not the solvent condition of seeding determines the morphology of the subsequent daughter generations of fibrils. This parallels the cross-seeding FTIR spectroscopy data of the same fibrillar systems [Dzwolak et al., 2005a]. It suggests that the two different morphologies are a more tangible aspect of the existence of two distinct conformational variants of insulin amyloid, both of which possess strong autocatalytic properties enabling thermodynamically favorable self-assembly pathways [Dzwolak et al., 2004b]. Further experiments with homogeneous-following-heterogeneous (and vice versa) seedings, as summarized in a recent study [Dzwolak et al., 2005a], support the notion that the original, unseeded templates determine the structural features of the following generation of seeded fibrils, regardless of environmental biases. This observation is in accordance with the now discussed AFM data.

The seeding patterns of insulin amyloid reported herein can be concluded to mirror a "templated memory" of the protein fibrils, which stores the solvation history of the original seeds, but not the properties of the environment, in which growth of following seeded generations continued (Fig. 4.18).
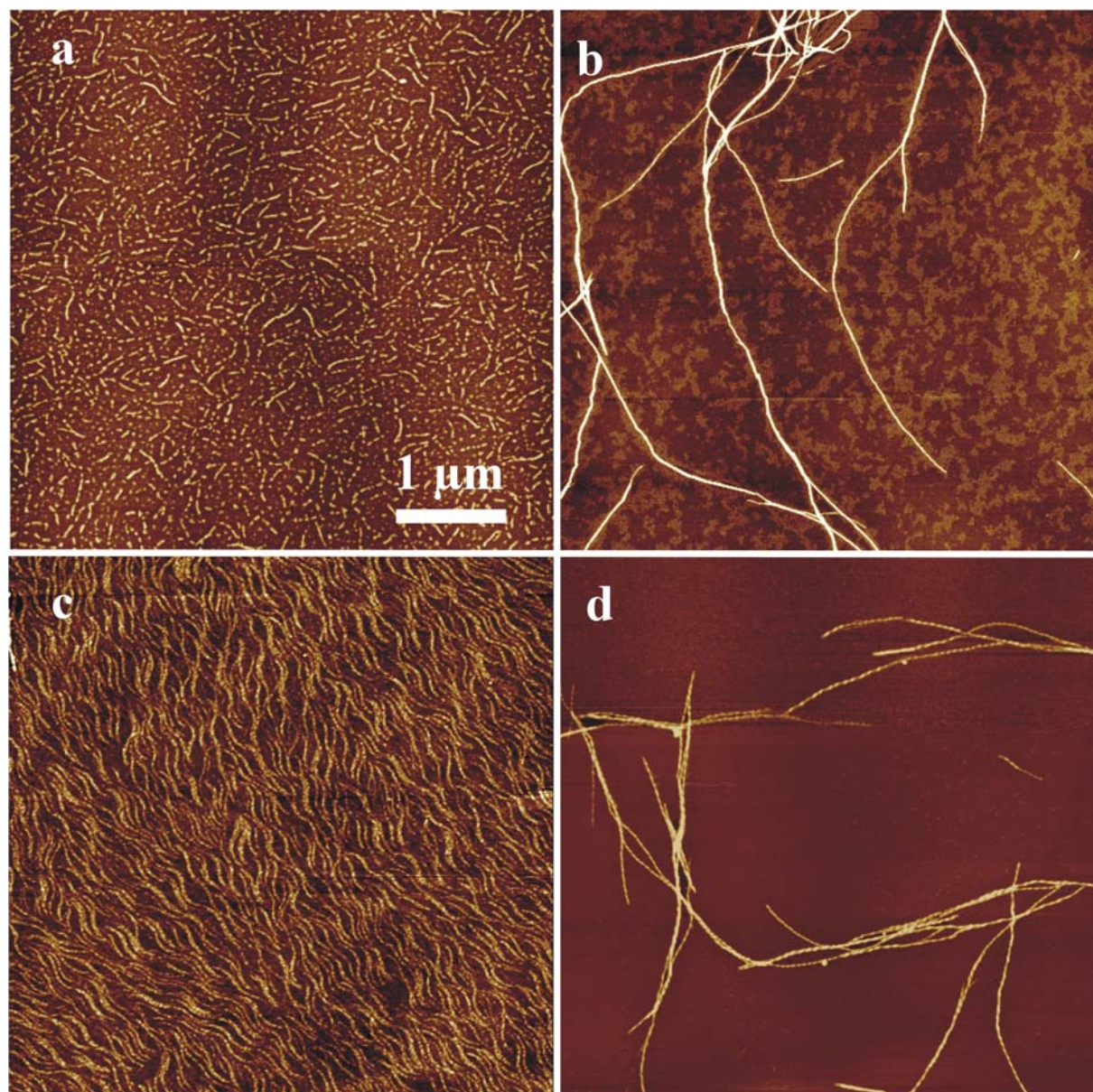
**Figure 4.17** AFM images of the first generation of insulin amyloid fibrils seeded homogeneously (a: EtOH-grown seeds injected to an insulin solution of 20 wt % EtOH; b: water-grown seeds injected to an aqueous insulin solution) and cross-seeded (c: EtOH-grown seeds injected to an aqueous insulin solution; d: water-grown seeds injected to an insulin solution in 20 wt % EtOH) reflect the prevalence of the template self-assembly history over the current environmental (solvational) properties. The relatively short, thin and curved insulin amyloid fibrils formed spontaneously in the presence of ethanol will reproduce the same morphology whether seeded homogeneously in an insulin solution of 20 wt % ethanol (a), or cross-seeded in an aqueous protein solution (c). Likewise, the long, thick and straight fibrils typical for water-based insulin amyloid preparations will proliferate maintaining the original morphology throughout both the homogeneous seeding (b) and the cross-seeding in the insulin solution of 20 wt % ethanol (d).

The actual nucleation event (i.e. assembly of destabilized insulin molecules into an amyloid template) takes place only during the unseeded amyloidogenesis at 60 °C [Nielsen et al., 2001a]. The temperature-induced (partial) unfolding of insulin causes exposure of

hydrophobic side-chains and renders the protein molecules sensitive to forces of EtOH-controlled preferential hydration and/or binding [Timasheff, 2002]. During the seeding at 25 °C, nucleation is kinetically marginalized by template-assisted elongation of fibrils. In other words, a thermodynamic control (through hydrational/solvational forces) of insulin self-assembly patterns is feasible only during the nucleation step, which occurs in the lag phase of the spontaneous aggregation process. Once the nucleus is formed and the elongation of a fibril sets in, the now kinetically controlled process tends to ignore environmental biases. Like a crystal, a growing amyloid fibril incorporates only those destabilized protein conformations in the fibrillar core which are capable of interacting similarly with the fibril to those conformers already existing in the fibril.

The presented case of fibril morphology controlled by the solvation history of aggregation nuclei opens up new prospects for the in situ synthesis of biomaterials, such as scaffolds that override unfavorable transient solvent conditions and maintain their programmed topology. At the same time, the fact that two morphologically distinguishable amyloidogenic templates may be induced in a single, covalently unmodified amino acid sequence parallels the prion strain phenomenon, and by the same token is an argument for the generic character of strains [Chien et al., 2004]. The cosolvent-effect used herein may be explored in a more comprehensive way in terms of preferential hydration and binding, and therefore offers means to explain physicochemical mechanisms leading to the occurrence of different amyloid strains.
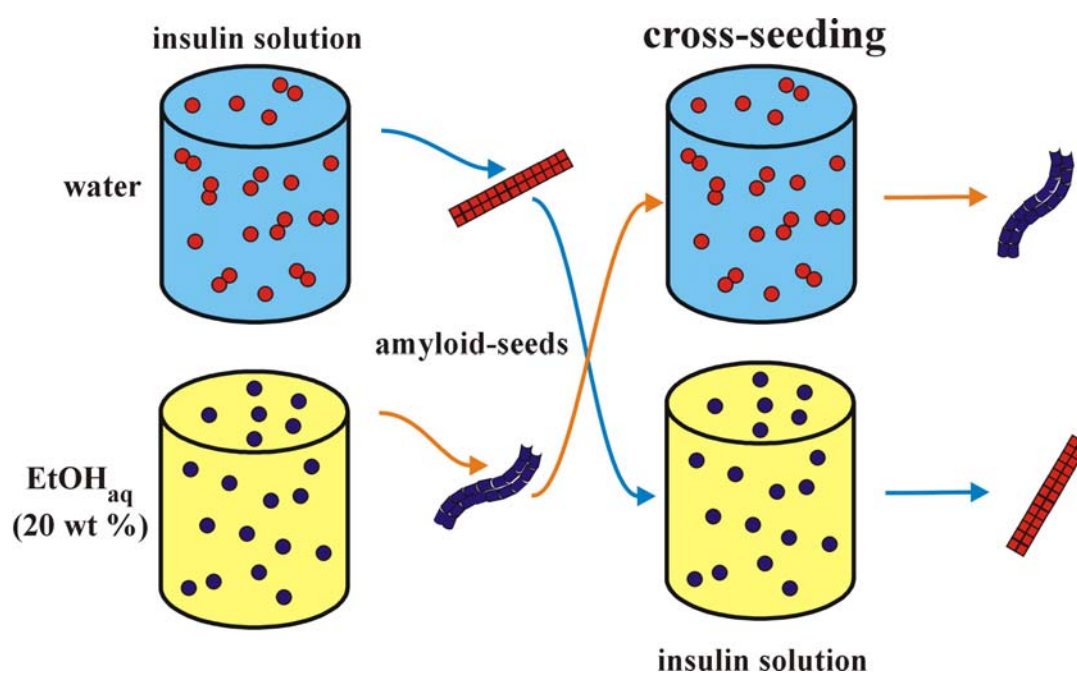


**Figure 4.18** The schematic summary of the insulin cross-seeding experiments shows how a "foreign" template is kinetically overriding a thermodynamically preferred aggregation pathway and reproduces its own morphology (under particular cosolvent conditions).

## 4.5   The Handedness of Twisted Insulin Fibrils

In conclusion of the insulin relating AFM study, a thorough re-examination of the entire raw AFM data with regard to the handed sense of twisted fibrillar structures was performed (the principle is illustrated in the appendix, Fig. 7.6). The motive for doing so was to check the well established hypothesis that the left-handed sense of twisted fibrils could be a generic feature of all amyloids. This assumption is based on the fact that all amyloid fibrils for which the handed sense has been determined have been reported to have a left-handed helical twist [Jiménez et al., 2002; Chamberlain et al., 2000; Goldsbury et al., 1999; Goldsbury et al., 2000; Iunescu-Zanetti et al., 1999; Harper et al., 1997]. The results yielded here were rather surprising, because the majority of the detected twisted fibrils turned out to be right-handed. On closer inspection, the following observations came to light:

Purely temperature-induced fibrils grown from the 60 and 70 °C test series, the cosolvent test series (20 wt % HAc, 20 wt % Glycerol and pure $D_2O$, all pH adjusted to 1.6 (instrument-reading)) exclusively exhibited right-handed fibrils (for examples, see Fig. 4.19). In sharp contrast to this, fibrils induced by seeding or cross-seeding experiments (water-grown seeds (0.1 wt %; pH = 1.6) injected into an aqueous insulin solution (0.1 wt %; pH = 1.6) with a mixing ratio of 1:20 merely showed a left-handed sense (Fig. 4.20). Likewise, fibrils matured under high hydrostatic pressure conditions (1 and 3.5 kbar) proved to be left-handed without any detectable exception (Fig. 4.20).

Another astonishing aspect is the fact that only AFM images with one handedness – either right or left – were observed. Please note that each of these observations is based on several independently performed sample preparations and monitorings, which stresses the general validity of our findings.

So far, the subject concerning the handed sense of amyloid fibrils is hardly investigated, and there have only a few provisional explanations been put forward. Based on EM investigations of insulin fibrils (grown under similar conditions to the 60 °C test series) and a computerized model for the β-strand arrangement and protofilament assembly of an insulin amyloid, Jiménez [Jiménez et al., 2002] claims that the left-handed sense of insulin fibrils is due to the left-handed twist between β-strands in β-sheets, which inevitably leads to a left-handed twist of the protofilaments and fibrils. At least, it can be stated now that this model is not universally applicable to all insulin fibrils. Moreover, it becomes evident that there is a strong need for a more mechanistic approach to this subject, which may explain the occurrence of distinct handed fibrils in relation to the kind of their induction and environmental factors (e.g. solvation, high pressure) influencing their genesis.
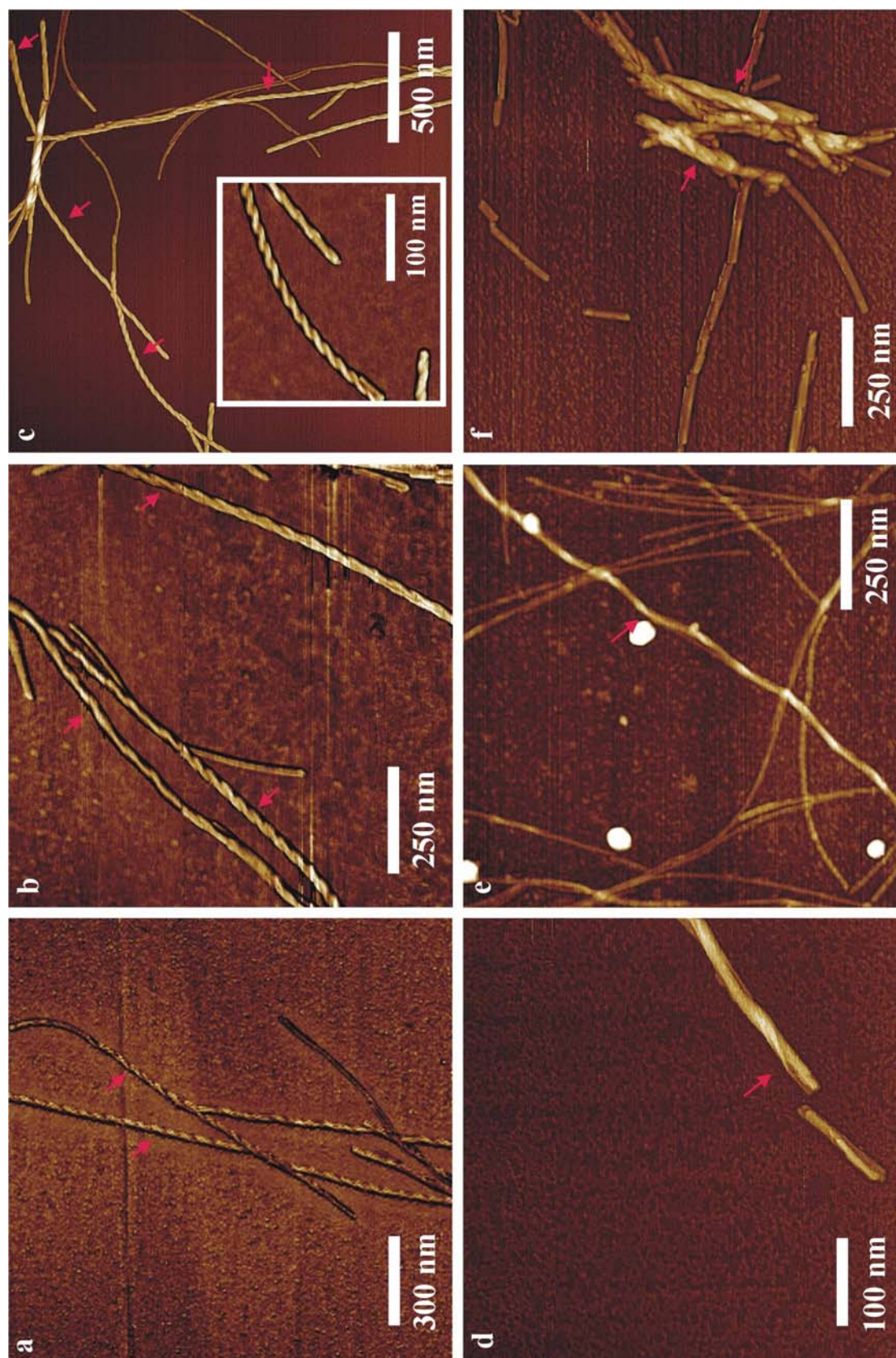
**Figure 4.19** AFM images showing right-handed insulin fibrils (red arrows). Fibrils obtained after 10 min and 20 min of incubation of a 0.1 wt % insulin solution (pH = 1.6) at 60 °C (a and b) and after 10 min of incubation at 70 °C (c). 0.5 wt % insulin (pH = 1.6) aggregated at 50 °C for 2 h in 20 wt % HAc (d) and in $D_2O$ (pH = 1.6; instrument reading) (f). 0.1 wt % insulin (pH = 1.6) aggregated at 60 °C for 6 days in 20 wt % glycerol (e).
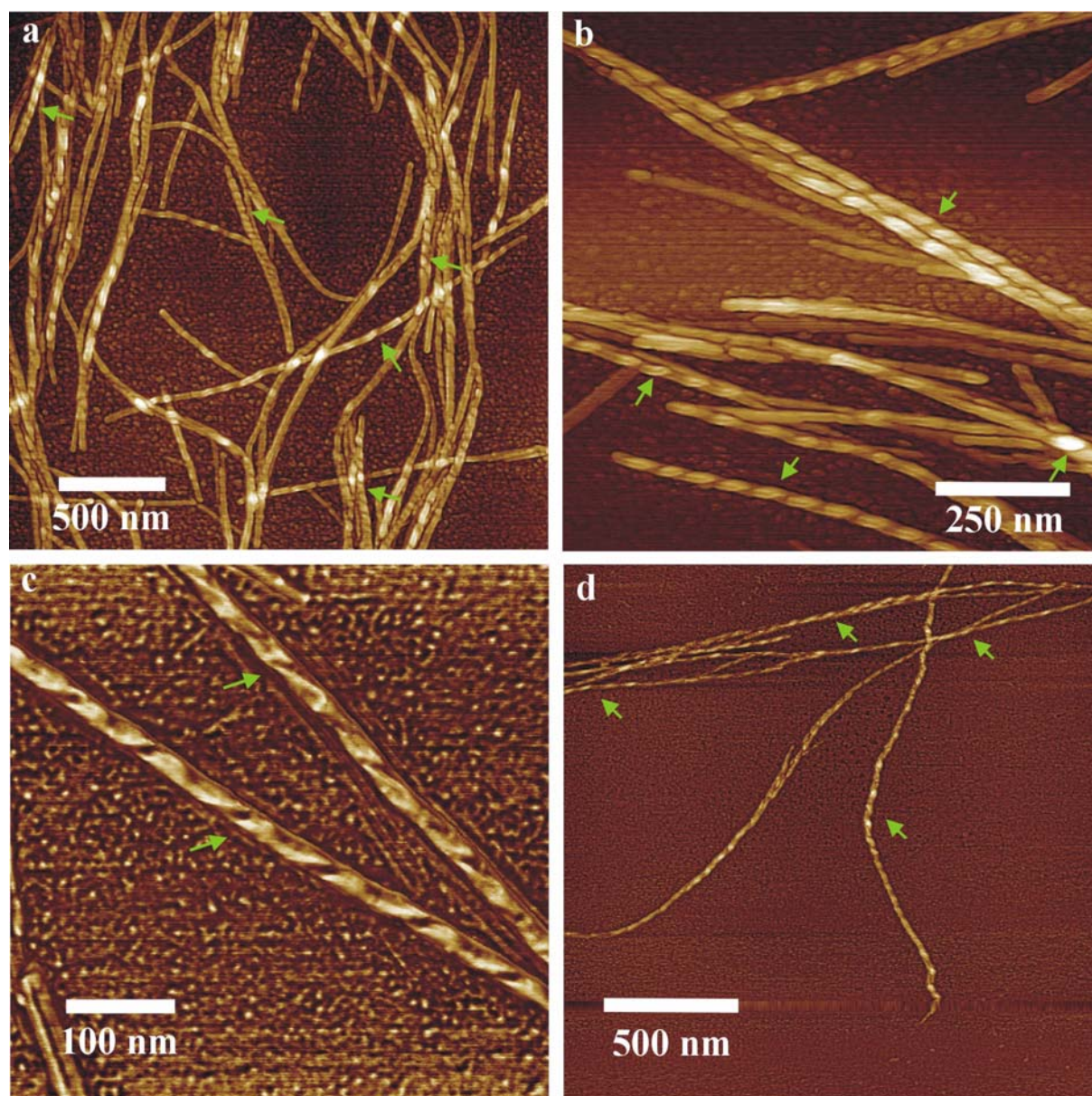
**Figure 4.20** AFM images showing left-handed insulin fibrils (green arrows). (a and b) Fibrils obtained from a 0.1 wt % insulin solution (pH = 1.6) after 19.5 h and 48h incubation at 1 kbar and 3.5 kbar, respectively ($T = 60\,°C$). (c and d) AFM images of the first generation of insulin fibrils seeded homogenously (c; water-grown seeds injected to an aqueous insulin solution) and cross-seeded (d; water-grown seeds injected into an insulin solution of 20 wt % EtOH). The incubation time for both seeding experiments was 24 h at 25 °C and the injection volume of the 0.1 wt % seed solution, which was inserted into the 0.1 wt % insulin solution (pH = 1.6), was 5 vol %.

## 4.6   Diastereomeric Self-Assembly of Polylysine

In order to complement the diverse parameters affecting the fibrillation phenomenon (like temperature, high hydrostatic pressure, solvational environment and the presence of pre-formed templates), possible consequences of stereospecific interactions between two polypeptide enantiomers are studied, using poly(D-lysine) (PDL) and poly(L-lysine) (PLL) as model polypeptides.

At 20 °C, the interaction of PLL and PDL in an equimolar, basic solution fosters a fast conformational α-to-β-transition, as shown in a recently published study of our research group [Dzwolak et al., 2004a]. As a consequence, after 96 hours first pre-fibrillar structures and after 120 hours mature amyloid-like fibrils form, whose AFM images are shown in Figs. 4.21 and 4.22. Judged by the cross-sectional heights of $(8 \pm 2)$ nm, $(16 \pm 3)$ nm, $(22 \pm 3)$ nm and $(32 \pm 6)$ nm, the defect-rich fibrils represent apparently various stages of structural assembly: from protofibrils to mature amyloid-like forms. It should be stressed that, although the time scale of the incubation is similar to that warranting the fibrillization of PLL alone [Fändrich and Dobson, 2002], only mixed enantiomers form the fibers at 20 °C, well below the temperature that triggers the conformational transition in a single enantiomer of polylysine (~ 35 °C).
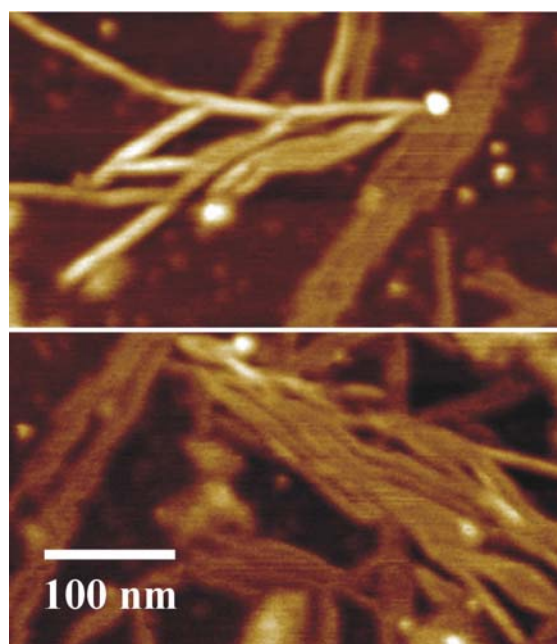


**Figure 4.21** AFM images of fibrils obtained after 120 h of incubation of an equimolar mixture of 1.5 wt % solutions of PDL and PLL in water, pH = 11.6.

The fibrils appear to have more defects than those composed of a single enantiomer observed by Fändrich and Dobson [Fändrich and Dobson, 2002]. One may speculate that the pronounced irreversibility [Dzwolak et al., 2004a] of the diastereomeric aggregation process somehow contributes to this observation, as this, on the molecular scale, would be likely to reduce the chains' capability of a topological rearrangement of a once-formed β-strand.
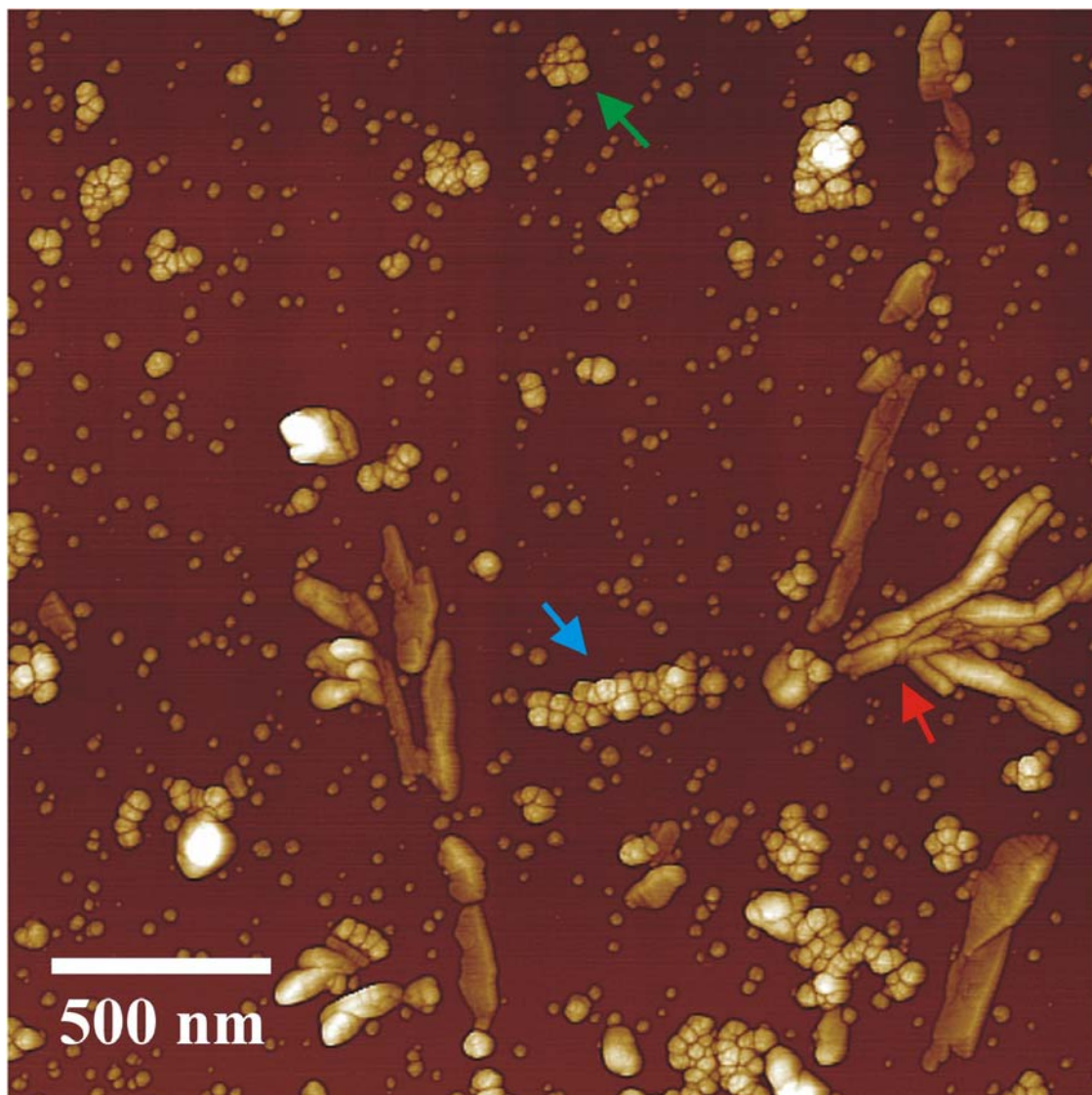


**Figure 4.22** High resolution AFM image showing the morphology of early pre-fibrillar and fibrillar structures (96 hours of incubation of an equimolar mixture of 1.5 wt % solutions of PDL and PLL in water, pH = 11.6). Apart from single polylysine particles, small and for the most part globular clusters of 10 -15 particles on average occur ((32 ± 3) nm in height; green arrow). Larger clusters with the same height ((32 ± 6) nm) form elongated shapes ((320 ± 5) nm in length; blue arrow) and turn into the primary fibrillar species (red arrow) of the same dimensions.

Regarding the early pre-fibrillar species occurring after 96 hours, their topology remarkably resembles insulin clusters and protofibrils despite of the natural difference in size (cf. Fig.

4.3a). The fact that two different and unrelated proteinaceous species, whose aggregation is triggered by two different driving forces (temperature-induced on one hand, and on the other hand stereospecific aggregation) create nearly identical fibril-precursors should be taken as another clue that amyloids are a generic trait of proteins and polypeptide chains. In this context it should also be stressed that in recent studies [Stefani and Dobson, 2003] especially these early aggregates are supposed to be more toxic than mature fibrils. It is speculated that their intrinsic ability to impair fundamental cellular processes by interacting with cellular membranes causes oxidative stress among others, which leads to necrotic cells death.

To conclude, this work has provided supporting ideas regarding the mechanisms that underlie the fibrillogenesis of two (structurally unrelated) polypeptides. The morphological characterization of their amyloidal self-assembly in distinct environments has demonstrated the relationship between various structural motifs that occur on the multi-pathway process of amyloidogenesis in vitro. Originally, it was the case of the forgetful lady "Auguste D." that has triggered extensive research in the - yet vastly unexplored - field of amyloid-related diseases. In that respect, this thesis may also contribute to a more detailed understanding of pathogenic amyloidogenesis and offer a rationale as to the medical control of protein conformational disorders.

# 5 Summary

In this study, the morphological events accompanying bovine insulin aggregation under ambient conditions, high hydrostatic pressure, cosolvent perturbation, and the presence of preformed seeds grown under different environmental conditions, were investigated with high resolution atomic force microscopy.

This work reveals the multistage, hierarchical character of the spontaneous fibrillation of insulin at low pH-value at 60 and 70 °C. Due to the marked enhancement of AFM image resolution achieved, it provides new clues as to fibril ultrastructures and mechanisms of assembly. In particular, the focus on the prefibrillar amorphous aggregates occurring 30 seconds after elevating temperature to 60 °C revealed the tendency of the globule-shaped oligomers to queue and assembly into elongated forms. This suggests that the shape of the nuclei itself predetermines in part the fibrillar architecture of the amyloid. Among first fibrillar structures, short but relatively thick (8 nm) seed-like forms appeared on a very short time scale within the first minute of incubation. It has been shown that such fibrils are likely to act as lateral scaffolds for the growth of amyloid. By using phase-image AFM as a nanometer-resolving probe of elastic surface properties, it could be shown that bundles of early protofilaments, associated into parallel fibrils, are capable of a cooperative transformation into twisted, highly ordered superhelices of the mature amyloid. Independently from producing evidence for the step-resolved character of the aggregation process, intermediate and morphologically heterogeneous forms were trapped and characterized, which yields direct evidence for the multipathway character of the amyloidogenesis of insulin. Apart from the faster kinetics, the increased temperature of 70 °C leads to a higher degree of morphological variability: along straight rods, twisted ribbon-like structures, rod bundles, and ropelike structures become prominent.

The high hydrostatic pressure experiments revealed that insulin forms amyloid fibrils of a unique circular morphology at 1500 bar. Despite some degree of size distribution, the smallest forms of an approximate diameter of 340 - 420 nm are most abundant among the ring-shaped structures. While the ability of high pressure to evoke such drastic perturbations on an amyloidogenic pathway may help to tune the conformation of amyloid templates, the very finding raises new questions concerning possible consequences for high-pressure food processing.

Solvational perturbations, accomplished by the addition of three model cosolvents, glycerol, ethanol and trifluoroethanol, exert a pronounced and diversified impact on the non-

native assembly of the amyloidogenic protein insulin. Glycerol stabilizes - through enhanced hydration - the native oligomeric state and retards fibrillar aggregation at all concentrations studied. In both ethanol- and TFE-water mixtures, an increasing concentration of alcohol has non-monotonic effects on the aggregation behavior of insulin. At low alcohol concentrations an accelerating effect on ordered fibrillation, bearing circular fibers, is observed. However, at high alcohol concentrations an inhibitory effect on fibrillation, ultimately leading to amorphous aggregation, could be revealed.

In the presence of ethanol, insulin forms an amyloid morphologically distinct from the ambient specimen. Due to the stability of fibrils and the autocatalytic character of the amyloid formation process, the two amyloid templates, when seeded, replicate the initial morphologies regardless of the solventional biases. Such "templated memory" effect appears to parallel the prion strains phenomenon, suggesting that strains may reflect a generic trait in all amyloids, including those not associated with diseases.

A general re-examination of the entire insulin relating (raw) AFM data concerning the handedness of twisted fibril structures yields surprising results: Contrary to the well established finding that all amyloid fibrils, for which the handedness has been determined, have been reported to have a left-handed helical twist, in this study also right-handed fibrils appear. In particular purely temperature-induced fibrils (60 and 70 °C test series, cosolvent test series with 20 wt % HAc (pH = 1.6), with 20 wt % glycerol (pH = 1.6) and in pure $D_2O$ (pH = 1.6; instrument reading)) exclusively show a right handed sense. On the other hand, fibrils induced by seeding and cross seeding or grown under high hydrostatic pressure conditions, feature twisted structures which are left-handed. At the moment, there is no mechanistically relevant interpretation available which may explain the occurrence of distinct twisted fibrillar structures in relation to the way of triggering fibrillation.

In order to spotlight further aspects of fibril formation, additional AFM-studies on the amyloidogenic behavior of a racemic mixture of poly(D-lysine) and poly(L-lysine) were performed. As a result, fibrillar structures were observed at a temperature far below that which triggers the conformational transition in a single enantiomer of polylysine. This suggests a stereospecific cooperative aggregation of polylysine enantiomers (diastereomeric aggregation).

# 6 Zusammenfassung

In der vorliegenden Arbeit wurden die morphologischen Aspekte der Aggregation von Rinderinsulin unter Umgebungsbedingungen, hohem hydrostatischem Druck, Cosolvens-Einfluß und bei Anwesenheit von Fibrillkeimen, die zuvor unter abweichenden Ausgangsbedingungen gereift sind, mittels Rastersondenmikroskopie untersucht.

Diese Studie stellt den mehrstufigen, hierarchischen Charakter der spontanen Fibrillbildung von Insulin bei einem pH-Wert von 1,6 und Temperaturen von 60 bzw. 70 °C vor. Aufgrund des guten rastermikroskopischen Auflösungsvermögens, das unter den gegebenen Arbeitsbedingungen bis in den Nanometerbereich reicht, konnten neue ultrastrukturelle und mechanistische Merkmale der Insulinfibrillbildung aufgezeigt werden. Ein Hauptaugenmerk wurde dabei auf die präfibrillären amorphen Formen, die bereits nach 30 Sekunden bei 60 °C auftreten und sich zu perlenkettenartigen Clustern vereinigen, gelegt. Deren lineare Form impliziert, daß hierdurch der faserartige Amyloidaufbau mit vorbestimmt wird. Innerhalb einer Inkubationszeit von einer Minute treten die ersten stäbchenartigen, relativ dicken (8 nm) fibrillären Spezies auf, die als Matrix auch zum lateralen Fibrillwachstum beitragen können. Mit Hilfe von AFM-Phasenbildern, die Veränderungen der Oberflächenelastizität detektieren, konnte aufgezeigt werden, daß Bündel früher Protofilamente, die sich zu parallel angeordneten Fibrillen zusammenfügen, kooperativ in helikal gewundene Endformen übergehen können. Unabhängig von den sich überwiegend stufenweise bildenden Fibrillformen konnten daneben auch die verschiedenartigsten morphologischen Übergangsformen und heterogen zusammengesetzten Fibrillagglomerate charakterisiert werden, was als direkter Hinweis auf einen stark verzweigten Reaktionsweg gewertet werden kann. Die erhöhte Inkubationstemperatur von 70 °C führt nicht nur zu einer beschleunigten Kinetik, sondern bewirkt auch eine erhöhte morphologische Variabilität der entstandenen Amyloidspezies: Neben geraden unverzweigten Stäbchen treten verdrehte und verflochtene bandartige Strukturen, Stabbündel und seilartige Strukturen auffallend in Erscheinung.

Die unter hohem hydrostatischem Druck (1500 bar) erzeugten Insulinfibrillen weisen eine zum ersten Mal für Insulinfibrillen beobachtete Kreisform mit Durchmessern von überwiegend 340 - 420 nm auf. Hierbei eröffnen sich nicht nur Möglichkeiten, durch definierte Kompression gezielt bestimmte Fibrilltemplate zu erzeugen, sondern es werden auch Fragen hinsichtlich möglicher Gefahren bei der Hochdrucksterilisation von Lebensmitteln aufgeworfen.

Lösungsmittelstöreinflüsse, hervorgerufen durch Zugabe der drei Modell-Cosolventien Glycerol, Ethanol und 2,2,2-Trifluorethanol, führen zu einem unterschiedlichen Aggregationsverhalten von Insulin. Glycerol stabilisiert durch „präferentielle Hydratation" die nativen Insulinoligomere und retardiert die Fibrillbildung. Dieser Effekt verstärkt sich zunehmend mit der Glycerolkonzentration. Im Gegensatz dazu weisen die mit Ethanol bzw. TFE versetzten Inkubationslösungen ein nicht monotones Verhalten auf. Bei niedrigem Alkoholanteil wird die geordnete Fibrillation, in der verstärkt kreisförmige Fibrillen auftreten, beschleunigt. Steigt jedoch der Alkoholanteil in der Inkubationslösung, so wird die Fibrillreifung zunehmend inhibiert und schließlich nur noch die Bildung amorpher Aggregate beobachtet.

Bei Anwesenheit von Ethanol bildet Insulin fibrilläre Species, die sich von denen in reiner wäßriger Lösung deutlich unterscheiden. Impfexperimente zeigen, daß im Zuge der Elongation neu eintretende Insulinmoleküle die Konformation der Moleküle im Keim (Templat) adaptieren, obwohl diese unter den aktuellen Lösungsmittelbedingungen nicht begünstigt werden sollte. Die Tatsache, daß die Konformation der Insulinmoleküle unabhängig von den Lösungsmittelbedingungen durch Impfung weitergegeben oder „vererbt" werden kann, ist kinetischen Ursprungs und wirft Parallelen zum Prionen-Stamm Phänomen auf und deutet den in dieser Hinsicht generischen Charakter aller Proteine an.

Eine abschließende Überprüfung aller schraubenförmigen fibrillären Strukturen des gesamten AFM-Insulin-Bilderpools führt zu folgendem überraschenden Ergebnis: Entgegen der bisher etablierten Auffassung, daß alle gewundenen amyloidogenen Fibrillen einen linksgängigen Drehsinn aufweisen müssen, treten in dieser Studie auch rechtsgängige Fibrillen auf. Dabei ist festzustellen, daß Fibrillen mit (ausschließlich) rechtem Drehsinn dann in Erscheinung treten, wenn die Fibrillogenese unter Umgebungsdruck und erhöhter Temperatur erfolgte. Selbst unter Cosolvenseinfluß (20 wt% Glycerol oder 20 wt% HAc) bzw. in reinem $D_2O$ waren ausschließlich rechtsdrehende Fibrillen auffindbar. Wurde die Gense der Fibrillen jedoch durch Beimpfung ausgelöst oder geschah diese unter hohem hydrostatischen Druck, entstanden ausschließlich Fibrillen mit linkem Drehsinn. Ein mechanistischer Zusammenhang zwischen der Auslöseform des Fibrillwachstums bzw. den Reifungsbedingungen und dem resultierenden Fibrilldrehsinn ist bis heute noch nicht aufgedeckt worden.

Außerhalb der Insulinversuchreihen wurde auch das amyloidogene Verhalten chiraler Polyaminosäuren untersucht. Dabei konnte ein diastereomerer Effekt aufgezeigt werden, der das Amyloidphänomen von einer neuen Seite beleuchtet. Es konnte nachgewiesen werden,

daß in einer racemischen Mischung aus Poly-D-lysin und Poly-L-lysin fibrillartige Strukturen weit unterhalb der Phasenumwandlungstemperatur des entsprechenden Enantiomers gebildet werden. Es scheint sich hier um eine neue, durch diastereomere Kooperation ausgelöste, Aggregationsvariante zu handeln.

# 7 Appendix

**Table 7.1** Amyloidogenic proteins and amyloid-based clinical disorders. (Adapted from [Uversky and Fink, 2004].)

| Disease-associated amyloidogenic proteins | | | |
| --- | --- | --- | --- |
| Amyloidogenic protein | Type of structure | Disease | Tissue distribution of protein deposits |
| Prion protein and its fragments | N-terminal fragment (23-121) is natively unfolded; C-terminal domain (121-230) is α-helical (perdominantly) | Creutzfeld-Jacob disease Gerstmann-Straussler-Schneiker syndrome Fatal familial insomnia Kuru BSE and scrapie | Brain |
| Amyloid-β and its fragments | Natively unfolded | AD Dutch hereditary cerebral hemorrhage Congophilic angiopathy | Brain Brain, spinal cord |
| ABri Cystain C | Natively unfolded α/β | Familial British dementia Hereditary cystain c angiopathy | Brain Brain |
| Huntingtin Androgen rececptor protein | α-Helical Ligand-binding and DNA-binding domains are α-helical; amino-terminal domain is natively unfolded | Huntington Disease Spinal and bulbar muscular atrophy | Brain Brain, scrotal skin, dermis, kidneys, heart, and testis, spinal cord |
| Ataxin-1 | Unknown | Spinocerebral ataxia Neuronal intranuclear inclusion disease | Brain, spinal cord Central and peripheral nervous system |
| DRPLA protein | Unknown | Hereditary dentatorubral-pallidoluysian atrophy | Brain |
| Serum amyloid A and its fragments | α/β | AA amyloidosis | Bladder, stomach, thyroid, kidneys, liver, spleen, gastrointestinal tract |
| Medin | β-Sheet | Aortic medial amyloidosis | Aortic smooth muscle |
| Islet amyloid polypeptide (IAPP, Amylin) | Natively unfolded | Pancreatic islet amyloidosis in late-onset diabetes (type II diabetes mellitus) | Pancreas |
| Calcitonin | Natively unfolded | Medullary Carcinoma of the Thyroid | Thyroid |
| Lysozyme | α+β | Hereditary systemic amyloidosis | Several visceral organs and tissues |
| Gelsolin | α/β | Hereditary systemic amyloidosis Finish-type familial amyloidosis | Several visceral organs and tissues |

**Table 7.1** (continued)

| Disease-associated amyloidogenic proteins | | | |
| --- | --- | --- | --- |
| Amyloidogenic protein | Type of structure | Disease | Tissue distribution of protein deposits |
| Transthyretin | β-Sheet (predominantly) | Senile systemic amyloidosis | Almost all organs and tissues, including heart, gland, arteries, bones, liver, digestive tract, etc. |
| | | Familial amyloid polyneuropathy | Various organs and tissues |
| Apolipoprotein A1 | α-Helical | Hereditary systemic amyloidosis | Eyes |
| $\beta_2$-Microglobulin | β-Sheet | Amyloid associated with hemodialysis | Musculoskeletal tissues (joints, bones, muscles), peripheral nervous system, gastrintestinal tract, tongue, heart urogeniteal tract |
| Tau protein | Probably natively unfolded | AD, Pick's disease, Progressive supranuclear palsy | Brain |
| Immunoglobulin light chain variable domains | β-Sheet | Light chain associated amyloidosis | Almost all organs and tissues, including heart, liver, kidneys, spleen, gastrointestinal tract, skin, tongue, endocrine glands, peripheral nervous system, etc. |
| | | Light chain deposition disease | Liver, spleen, bone marrow, vessel walls, prenchymal tissue, kidneys, heart liver, skin, lungs, tongue, ovary, pancreas, etc. |
| | | Light chain cast nephropathy | Kidneys |
| | | Light chain cardiomyopathy | Heart |
| α-Synuclein | Natively unfolded | Parkinson's disease Diffuse Lewy bodies disease Lewy bodies variant of AD Hallervorden-Spatz disease | Brain |
| NAC | Natively unfolded | AD | Brain |
| Fibrinogen and its fragments | β-Sheet | Hereditary renal amyloidosis | Kidneys |
| Atrial natriuretic factor | ? | Atrial amyloidosis | Heart |
| Insulin | Predominantly α-Helical | Injection-localized amyloidosis | Skin, muscles |

**Figure 7.1** View of the AFM-lab showing the technical setup for AFM investigations.
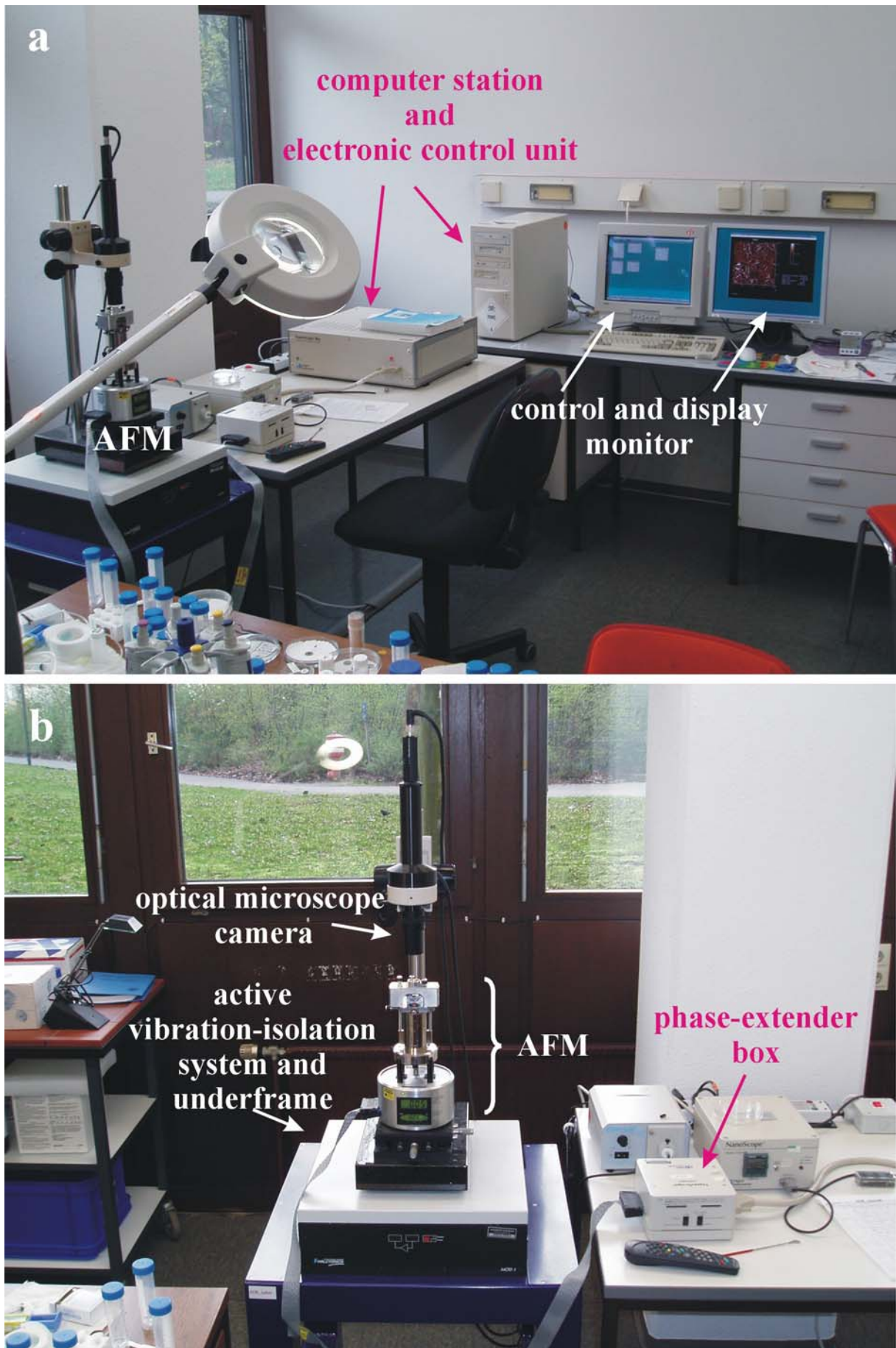
**Figure 7.2** (a) AFM image of insulin fibrils (0.1 wt %, pH = 1.6) grown at 60°C for 8 days under ambient pressure and incubated subsequently at 4.5 kbar and room temperature for 48 h. No distinct morphological modifications are perceptible. (b) Insulin fibers (0.5 wt %, pH = 1.6) grown at 60 °C and 500 bar for 20 hours.
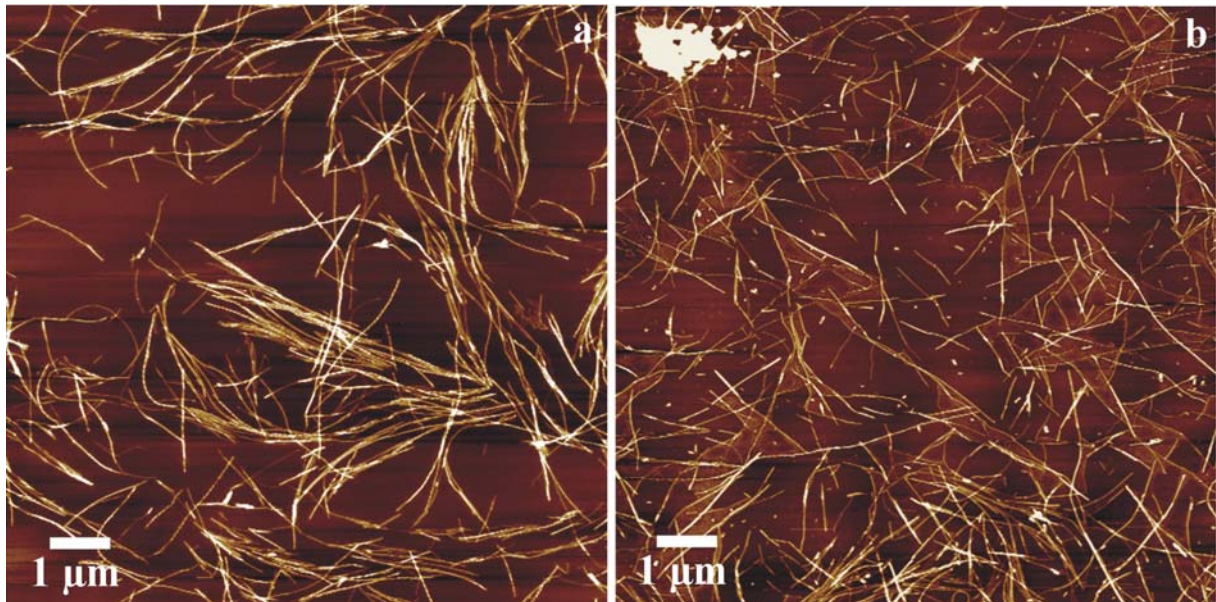


**Figure 7.3** Amorphous insulin (0.1 wt %, pH = 1.6) aggregates incubated for 6 days at 60 °C in presence of 70 wt % EtOH. (a) No fibrillar forms are detectable and new doughnut-shaped forms, ~ 40 nm in height and ~ 150 nm in diameter appear to dominate (green arrows). (b) Sporadically, giant species with diameters up to 1.5 μm and heights of 300 nm occur.
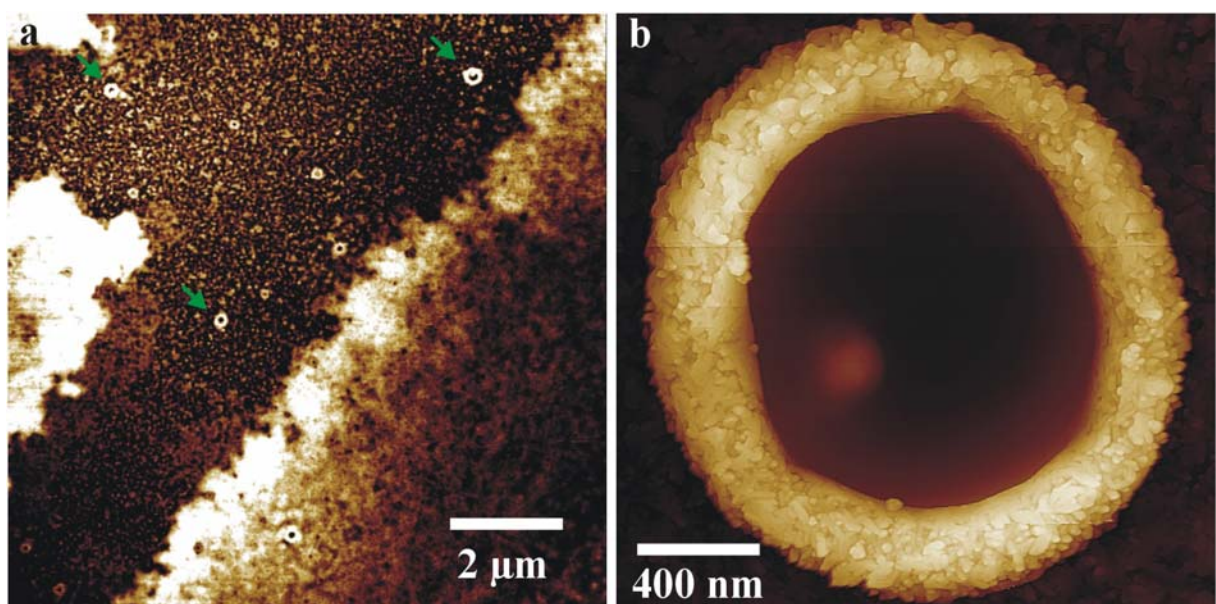
**Figure 7.4** Seeding control samples showing mica surfaces, applied with a) a fresh 0.1 wt % insulin solution (pH = 1.6), b) insulin (0.1 wt %, pH = 1.6) incubated for 24 hours at 25 °C, a 1:20 (vol/vol) mixture of 0.1 wt % freshly sonificated insulin fibrils and pure water, and d) a homogeneously (water→water) seeded insulin solution incubated for 24 hours at 25 °C.
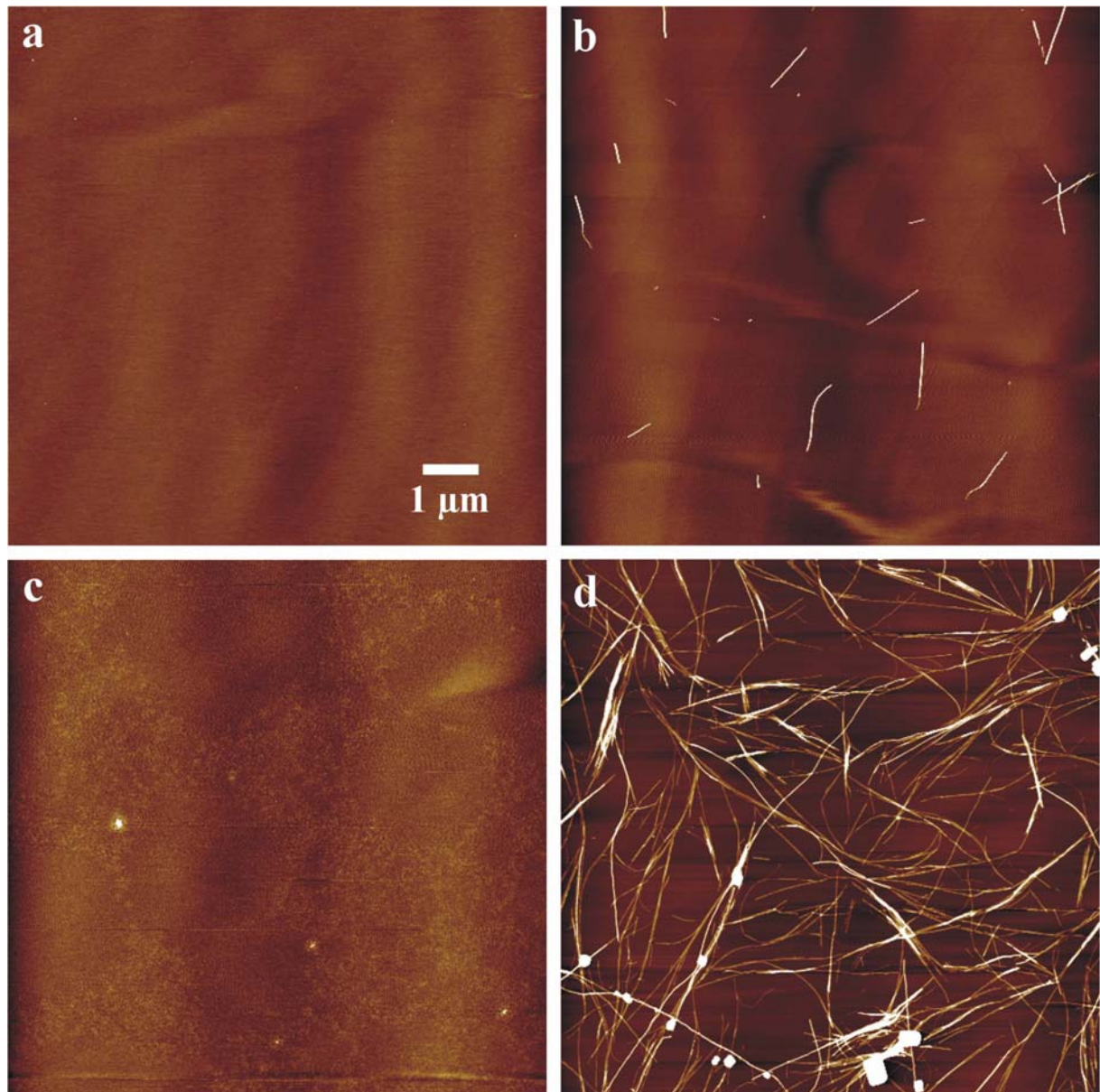
**Figure 7.5** Model of atomic arrangements for bulk-like terminated silicon tips, (a) pointing in the <100> direction and (b) in the <111> direction.
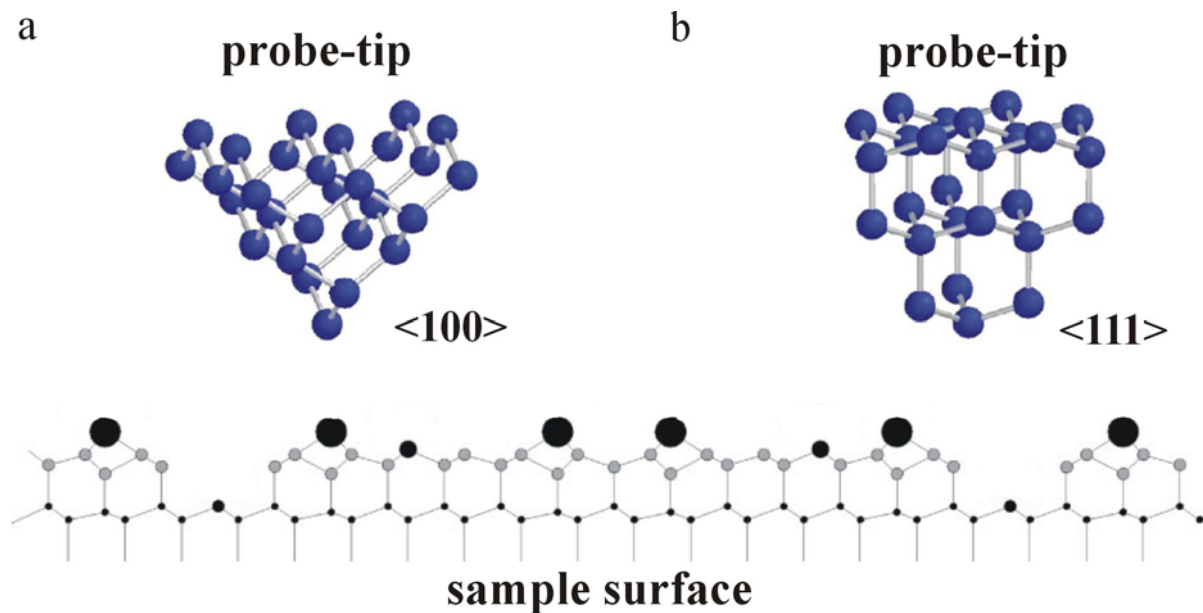


**Fig. 7.6** Simple method for determining whether a twisted structure is right-handed or left-handed: Make fists of your two hands with thumbs outstretched and pointing straight up. Looking at the left hand, think a helix spiraling up the left thumb in the direction in which the other four fingers are curled as shown (clockwise). The resulting helix is left-handed (a). The right hand will demonstrate a right-handed structure, which rotates in the counterclockwise direction as it spirals up the right thumb (b).
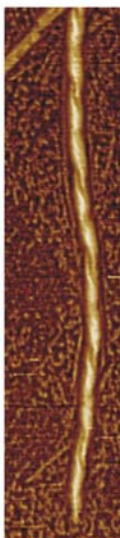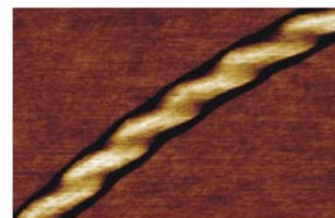
# 8   References

Aggeli, A., Nyrkova, I. A., Bell, M., Harding, R., Carrick, L., McLeish, T. C., Semenov, A. N. and Boden, N. (2001). Hierarchical self-assembly of chiral rod-like molecules as a model for peptide β-sheet tapes, ribbons, fibrils, and fibers. *Proc. Natl. Acad. Sci. U.S.A.* **98**, 11857 - 11862.

Aguzzi, A. (2004). Understanding the diversity of prions. *Natl. Cell. Biol.* **6**, 290 - 292.

Ahmad, A., Millett, I. S., Doniach, S., Uversky, V. N. and Fink, A. L. (2003). Partially folded intermediates in insulin fibrillation. *Biochemistry* **42**, 11404 - 11416.

Anfinsen, C. B., Redfield, R. R., Choate, W. I., Page, J. and Carrol,W. R. (1954). Studies on the gross structure, cross-linkages, and terminal sequences in ribonuclease. *J. Biol. Chem.* **207**, 201 - 210.

Anfinsen, C. B. (1973). Principles that govern the folding of protein chains. *Science* **181**, 223 - 230.

Arora, A., Ha, C. and Park, C. B. (2004). Insulin amyloid fibrillation at above 100 degrees C: New insights into protein folding under extreme temperatures. *Protein Sci.* **13**, 2429 - 2436.

Bailey, S. W. (ed.) (1988). *Hydrous Phyllosilicates (exlusive of micas)*, Mineralogical Society of America, Washington.

Bellotti, V., Mangione, P. and Stoppini, M. (1999). Biological activity and pathological implications of misfolded proteins. *Cell. Mol. Life Sci.* **55**, 977 - 991.

Binnig, G., Rohrer, H., Gerber, Ch. and Weibel, E. (1982). Surface studies by scanning tunnelling microscopy. *Phys. Rev. Letts.* **49**, 57 - 61.

Binnig, G., Quate, C. F. and Gerber, Ch. (1986). Atomic Force Microscope. *Phy. Rev. Lett.* **56**, 930 - 933.

Bonnell, D. A. (1993). *Scanning Tunnelling Microscopy and Spectroscopy*, VCH Verlagsgesellschaft mbH, New York.

Boonyaratanakornkit, B. B., Park, C. B. and Clark, D. S. (2002). Pressure effects on intra- and intermolecular interactions within proteins. *Biochim. Biophys. Acta* **1595**, 235 - 249.

Booth, D. R., Sunde, M., Bellotti, V., Robinson, C. V., Hutchinson, W. L., Fraser, P. E., Hawkins, P. N., Dobson, C. M., Radford, S. E., Blake, C. C. F. and Pepys, M. B. (1997). Instability, unfolding and aggregation of human lysozyme variants underlying amyloid fibrillogenesis. *Nature* **385**, 787 - 793.

Bouchard, M., Zurdo, J., Nettleton, E. J., Dobson, C. M. and Robinson, C. V. (2000). Formation of insulin amyloid fibrils followed by FTIR simultaneously with CD and electron microscopy. *Protein Sci.* **9**, 1960 - 1967.

Brange, J., Skelbaek-Pedersen, B., Langkjaer, L., Damgaard, U., Ege, H., Havelund, S., Heding, L. G., Jorgensen, K. H., Lykkeberg, J., Markussen, J., Pingel, M. and Rasmussen, E. (1987). In *Galenics of insulin. The physicochemical and pharmaceutical aspects of insulin and insulin preparations*, Springer-Verlag, Berlin.

Brange, J., Andersen, L., Laursen, E. D., Meyn, G., and Rasmussen, E. (1997). Toward understanding insulin fibrillation. *J. Pharm. Sci.* **86**, 517 - 525.

Brettin, M. (2001). Alzheimer. *GEO* **12**, 72 - 94.

Bryant, C., Strohl, M., Green, K. L., Long, H. B., Alter, L. A., Pekar, A. H., Chance, R. E. and Brems, D. N. (1992). Detection of an equilibrium intermediate in the folding of a monomeric insulin analog. *Biochemistry* **31**, 5692 - 5698.

Buck, M. (1998). Trifluoroethanol and colleagues: cosolvents come of age. Recent studies with peptides and proteins. *Quarterly Rev. Biophys.* **31**, 297 - 355.

Bull, H. B. and Breese, K. (1978). Interaction of alcohols with proteins. *Biopolymers* **17**, 2121 - 2131.

Bundesministerium für Bildung und Forschung (eds.) (2002). *Nanotechnologie in Deutschland - Standortbestimmung*, Referat Publikationen des Ministeriums, Bonn.

Burke, M. J. and Rougvie, M. A. (1972). Cross-β protein structures. I. Insulin fibrils. *Biochemistry* **11**, 2435 - 2439.

Bustamante, C., Rivetti, C. and Keller, D. J. (1997). Scanning force microscopy under aqueous solutions. *Curr. Opp. Struct. Biol.* **7**, 709 - 716.

Butt, H.-J. (1991a). Electrostatic interaction in atomic force microscopy. *Biophys. J.* **60**, 777 - 785.

Butt, H.-J. (1991b). Measuring electrostatic, van der Waals, and hydration forces in electrolyte solutions with an atomic force microscope. *Biophys. J.* **60**, 1438 - 1444.

Butt, H.-J., Jaschke, M. and Ducker, W. (1995). Measuring surface forces in aqueous solution with the atomic force microscope. *Bioelectrochem. Bioenerg.* **38**, 191 - 201.

Carrier, D., Mantsch, H. H. and Wong. P. T. T. (1990a). Protective effect of lipidic surfaces against pressure-induced conformational changes of poly(L-lysine). *Biochemistry* **29**, 254 - 258.

Carrier, D., Mantsch, H. H. and Wong, P. T. T. (1990b). Pressure-induced reversible changes in secondary structure of poly(L-lysine): An IR spectroscopic study. *Biopolymers* **29**, 837 - 844.

Chamberlain, A. K., MacPhee, C. E., Zurdo, J., Morozova-Roche, L. A., Hill, H. A. O., Dobson, C. M. and Davis, J. J. (2000). Ultrastructural organization of amyloid fibrils by atomic force microscopy. *Biophys. J.* **79**, 3282 - 3293.

Chang, X., Jorgensen, A. M., Bardrum, P. and Led, J. J. (1997). Solution structures of the $R_6$ human insulin hexamer. *Biochemistry* **36**, 9409 - 9422.

Chen, C. J. (1993). *Introduction to Scanning Tunnelling Microscopy*, Oxford University Press, New York.

Chi, E. Y., Krishnan, S., Randoplh, T. W. and Carpenter J. F. (2003). Physical stability of proteins in aqueous solution: Mechanism and driving force in nonnative protein aggregation. *Pharm. Res.* **20**, 1325 - 1336.

Chien, P. and Weissmann, J.S. (2001). Conformational diversity in a yeast prion dictates its seeding specificity. *Nature* **410**, 223 - 227.

Chien, P., Weissman, J. S. and DePace, A. H. (2004). Emerging principles of conformation-based prion inheritance. *Annu. Rev. Biochem.* **73**, 617 - 656.

Chiou, J. S., Tatara, T., Sawamura, S., Kaminoh, Y., Kamaya, H., Shibata, A. and Ueda, I. (1992). The α-helix to β-sheet transition in poly(L-lysine): Effects of anesthetics and high pressure. *Biochim. Biophys. Acta* **1119**, 211 - 217.

Chiti, F., Webster, P., Taddei, N., Clark, A., Stefani, M., Ramponi, G. and Dobson, C. M. (1999). Designing conditions for in vitro formation of amyloid protofilaments and fibrils. *Proc. Natl. Acad. Sci. U. S. A.* **96**, 3590 - 3594.

Cinelli, S., Onori, G. and Santucci,A. (1997). Effects of aqueous alcohol solutions on the thermal transition of lysozyme. *J. Phys. Chem. B* **101**, 8029 - 8043.

Cleveland, J. P., Ancykowski, B., Schmid, A. E. and Elings, V. B. (1998). Energy dissipation in tapping-mode atomic-force microscopy. *Appl. Phys. Lett.* **72**, 2613 - 2615.

Czeslik, C., Seemann, H. and Winter, R. (2001). *Basiswissen Physikalische Chemie*, Teubner, Stuttgart, Leipzig, Wiesbaden.

Czeslik, C., Jansen, R., Ballauff, M., Wittemann, A., Royer, C. A., Gratton, E. and Hazlett, T. (2004). Mechanism of protein binding to spherical polyelectrolyte brushes studied *in situ* using two-photon excitation fluorescence fluctuation spectroscopy. *Phys. Rev. E* **69**, 021401-1 - 021401-9.

Delineau, L. (2001). *Dynamik der Spitze-Probe Wechselwirkung bei der Rasterkraft-mikroskopie an Elastomeren*, Dissertation, Albert-Ludwigs-Universität, Freiburg im Breisgau.

Derewenda, U. and Dodson, G. G. (1993). In *Molecular Structures in Biology*, (eds. R. Diamonds et al.) pp. 260 - 277. Oxford University Press, Oxford.

Dobson, C. M. (1999). Protein misfolding, evolution and disease. *Trends Biochem. Sci.* **24**, 329 - 332.

Ducker, W. A., Senden, T. J. and Pashley, R. M. (1991). Direct measurements of colloidal forces using an atomic force microscope. *Nature* **353**, 239 - 241.

Dunn, R. (1999). Near-field scanning optical microscopy. *Chem. Rev.* **99**, 2891 - 2927.

Dzwolak, W., Ravindra, R., Lendermann, J. and Winter, R. (2003). Aggregation of bovine insulin probed by DSC/PPC calorimetry and FTIR spectroscopy. *Biochemistry* **42**, 11347 - 11355.

Dzwolak, W., Ravindra, R., Nicolini, C., Jansen, R. and Winter, R. (2004a). The diastereoisomeric assembly of polylysine is the low-volume pathway for preferential formation of β-sheet aggregates. *J. Am. Chem. Soc.* **126**, 3762 - 3768.

Dzwolak, W., Smirnovas, V., Jansen, R. and Winter, R. (2004b). Insulin forms amyloid in a strain-dependent manner: An FT-IR spectroscopic study. *Protein Sci.* **13**, 1927 - 1932.

Dzwolak, W., Jansen, R., Smirnovas, V., Loksztejn, A., Porowski, S. and Winter, R. (2005a). Template-controlled conformational patterns of insulin fibrillar self-assembly reflect history of solvation of the amyloid nuclei. *Phys. Chem. Chem. Phys.* **7**, 1349 - 1351.

Dzwolak, W., Grudzielanek, S., Smirnovas, V., Ravindra, R., Nicolini, C., Jansen, R., Loksztejn, A., Porowski, S. and Winter, R. (2005b). Ethanol-perturbed amyloidogenic self-assembly of insulin: Looking for origins of amyloid strains. *Biochemistry*, in press.

Engel, A., Schoenenberger, C.-A. and Müller, D. J. (1997). High-resolution imaging of native biological sample surfaces using scanning probe microscopy. *Curr. Opin. Struct. Biol.* **7**, 279 - 284.

Engel, A., Gaub, H. E. and Müller, D. J. (1999). Atomic force microscopy: A forceful way with single molecules. *Curr. Biol.* **9**, R133 - R136.

Falbe, J. and Regtiz, M. (eds.) (1995). *CD-Römpp, Chemielexikon*, vers. 1, Georg Thieme Verlag, Stuttgard.

Fändrich, M., Fletcher, M. A. and Dobson, C. M. (2001). Amyloid fibrils from muscle myoglobin - Even an ordinary globular protein can assume a rogue guise if conditions are right. *Nature* **410**, 165 - 166.

Fändrich, M. and Dobson, C. M. (2002). The behaviour of polyamino acids reveals an inverse side chain effect in amyloid structure formation. *EMBO J.* **21**, 5682 - 5690.

Farley, C. (1999). *NanoScope® Command Reference Manual*, Version 4.42, Digital Instruments Veeco Metrology Group, Santa Barbara.

Ferrão-Gonzales, A. D., Souto, S. O., Silva, J. L. and Foguel, D. (2000). The preaggregated state of an amyloidogenic protein: Hydrostatic pressure converts native transthyretin into the amyloidogenic state. *Porc. Natl. Acad. Sci. U. S. A.* **97**, 6445 - 6450.

Fezoui, Y. and Templow, D. B. (2002). Kinetic studies of amyloid β-protein fibril assembly. *J. Biol. Chem.* **277**, 36948 - 36954.

Fioroni, M., Diaz, M. D., Burger, K. and Berger, S. (2002). Solvation phenomena of a tetrapeptide in water/trifluoroethanol and water/ethanol mixtures: A diffusion NMR, intermolecular NOE, and molecular dynamics study. *J. Am. Chem. Soc.* **124**, 7737 - 7744.

Foguel, D., Suarez, M. C., Ferrão-Gonzales, A. D., Porto, T. C. R., Palmieri, L., Einsiedler, C. M. *et al.* (2003). Dissociation of amyloid fibrils of alpha-synuclein and transthyretin by pressure reveals their reversible nature and the formation of water-excluded cavities. *Proc. Natl. Acad. Sci. U. S. A.* **100**, 9831 - 9836.

Gerlough, T. D., and Bates, R. W. (1932). The purification and some properties of insulin. *J. Pharmacol. Exp. Ther.* **45**, 19 - 51.

Giessibl, F.J. (1997). Forces and frequency shifts in atomic resolution dynamic force microscopy. *Phys. Rev. B* **56**, 16010 - 16015.

Giessibl, F. J., Hembacher, S., Bielefeldt, H. and Mannhart, J. (2000). Subatomic features on the silicon (111) - (7×7) surface observed by atomic force microscopy. *Science* **289**, 422 - 425.

Giessibl, F. J., Hembacher, S., Bielefeldt, H. and Mannhart, J. (2001). Response to technical comment: Subatomic features in atomic force microscopy images. *Science* **291**, 2509a.

Giessibl, F. J. (2003). Advances in atomic force microscopy. *Rev. Mod. Phys.* **75**, 949 - 983.

Goodman, F. O. and Garcia, N. (1991). Roles of the attractive and repulsive forces in atomic-force microscopy. *Phys. Rev. B* **43**, 4728 - 4731.

Goldsbury, C., Kistler, J., Aebi, U., Arvinte, T. and Cooper, G. J. S. (1999). Watching amyloid fibrils grow by time-lapse atomic force microscopy. *J. Mol. Biol.* **285**, 33 - 39.

Goldsbury, C., Wirtz, S., Müller, S. A., Sunderji, S., Wicki, P., Aebi, U. and Frey, P. (2000). Studies on the *in vitro* assembly of Aβ 1-40: Implications for the search for Aβ fibril formation inhibitors. *J. Struct. Biol.* **130**, 217 - 231.

Gorovits, B. M. and Horowitz, P. M. (1998). High hydrostatic pressure can reserve aggregation of protein folding intermediates and facilitate acquisition of native structure. *Biochemistry* **37**, 6132 - 6135.

Gross, M. and Jaenicke, R. (1994). Proteins under Pressure. The influence of high hydrostatic pressure on structure, function and assembly of proteins and protein complexes. *Eur. J. Biochem.* **221**, 617 - 630.

Groß, M. (2003). Amyloidkrankheiten - kleine Fortschritte, große Fragen. *Nachrichten aus der Chemie* **51**, 1261 - 1263.

Grudzielanek, S., Jansen, R. and Winter, R. (2005). Solvational tuning of the unfolding aggregation and amyloidogenesis of insulin. *J. Mol. Biol.*, in press.

Halcyonics (2003). *MOD™ System Information Booklet*, Halcyonics GmbH, Göttingen.

Hamaker, H. C. (1937). The London-van der Waals attraction between spherical particles. *Physica (Amsterdam)* **4**, 1058 - 1072.

Harper, J. D., Lieber, C. M. and Lansbury, P. T. (1997). Atomic force microscopy imaging of seeded fibril formation and fibril branching by the Alzheimer's amyloid beta protein. *Chem. Biol.* **4**, 951 - 959.

Herberhold, H. and Winter, R. (2002). Temperature- and pressure-induced unfolding and refolding of ubiquitin: A static and kinetic Fourier transform infrared spectroscopy study. *Biochemistry* **41**, 2396 - 2401.

Herz, M., Giessibl, F. J. and Mannhart, J. (2003). Probing the shape of atoms in real space. *Phys. Rev. B* **68**, 045301-1 - 045301-7.

Hirota, N., Mizuno, K. and Goto, Y. (1998).Group additive contributions to the alcohol-induced α-helix formation in mellitin: implication for the mechanism of the alcohol effects on proteins. *J. Mol. Biol.* **275**, 365 - 378.

Hong, D. P., Hoshino, M., Kuboi, R. and Goto, Y. (1999). Clustering of fluorine-substituted alcohols as a factor responsible for their marked effects on proteins and peptides. *J. Am. Chem. Soc.* **121**, 8427 - 8433.

Hua, Q. X. and Weiss, M. A. (2004). Mechanism of insulin fibrillation: The structure of insulin under amyloidogenic conditions resembles a protein-folding intermediate. *J. Biol. Chem.* **279**, 21449 - 21460.

Hug, H. J., Lantz, M. A., Abdurixit, A., van Schendel, P. J. A., Hoffmann, R., Kappenberger, A. and Baratoff, A. (2001). Technical comment: Subatomic features in atomic force microscopy images. *Science* **291**, 2509a.

Hummer, G., Garde, S., Garcia, A. E., Paulatis, M. E. and Pratt, L. R. (1998). The pressure dependence of hydrophobic interactions is consistent with the observed pressure denaturation of proteins. *Proc. Natl. Acad. Sci. U. S. A.* **95**, 1552 - 1555.

Ionescu-Zanetti, C., Khurana, R., Gillespie, J. R., Petrick, J. S., Trabachino, L. C., Minert, L. J., Carter, S. A. and Fink, A. L. (1999). Monitoring the assembly of Ig light-chain amyloid fibrils by atomic force microscopy. *Proc. Natl. Acad. Sci. U. S. A.* **96**, 13175 - 13179.

Ismail, A. A. and Mantsch, H. H. (1992). Salt bridge induced changes in the secondary structure of ionic polypeptides. *Biopolymers* **32**, 1181 - 1186.

Israelachvili, J. N. (1994). *Intermolecular and surface forces*, 2<sup>nd</sup> ed., Academic Press, London, San Diego, New York, Boston, Sydney, Tokyo, Toronto.

Jackson, M., Haris, P. I. and Chapman, D. (1989). Conformational transition in poly(L-lysine): Studies using Fourier transform infrared spectroscopy. *Biochim. Biophys. Acta* **998**, 75 - 79.

Jansen, R., Grudzielanek, S., Dzwolak, W. and Winter, R. (2004). High pressure promotes circularly shaped insulin amyloid. *J. Mol. Biol.* **338**, 203 - 206.

Jansen, R., Dzwolak, W. and Winter, R. (2005). Amyloidogenic self-assembly of insulin aggregates probed by high resolution atomic force microscopy. *Biophys. J.* **88**, 1344 - 1353.

Janshoff, A., Neitzert, M., Oberdorfer, Y. and Fuchs, H. (2000). Kraftspektroskopie an molekularen Systemen - Einzelmolekülspektroskopie an Polymeren und Biomolekülen. *Angew. Chem.* **112**, 3346 - 3374.

Jiang, Y., Li, H., Zhu, L., Zhou, J. M. and Perret, S. (2004). Amyloid nucleation and hierarchical assembly of Ure2p fibrils. Role of asparagine/glutamine repeat and nonrepeat regions of the prion domains. *J. Biol. Chem.* **279**, 3361 - 3369.

Jiménez, J. L., Nettleton, E. J., Bouchard, M., Robinson, C. V. and Dobson, C. M. (2002). The protofilament structure of insulin amyloid fibrils. *Proc. Natl. Acad. Sci. U. S. A.* **99**, 9196 - 9201.

Kad, N. M., Myers, S. L., Smith, D. P., Smith, D. A., Radford, S. E. and Thomson, N. H. (2003). Hierarchical assembly of $\beta_2$-microglobulin amyloid *in vitro* revealed by atomic force microscopy. *J. Mol. Biol.* **330**, 785 - 797.

Karrasch, S., Dolder, M., Hoh, J., Schabert, F., Ramsden, J. and Engel, A. (1993). Covalent binding of biological samples to solid supports for scanning probe microscopy in buffer solution. *Biophys. J.* **65**, 2437 - 2446.

Kasas, S., Thomson, N. H., Smith, B. L., Hansma, H. G., Zhu, X., Guthold, M., Bustamante, C., Kool, E. T., Kashlev, M. and Hansma, P. K. (1997). *Escherichia coli* RNA polymerase activity observed using atomic force microscopy. *Biochemistry* **36**, 461 - 468.

Katzman, R. and Saitoh, T. (1991). Advances in Alzheimer's disease. *FASEB J.* **5**, 278 - 286.

Kauzmann, W. (1959). Some factors in the interpretation of protein denaturation. *Adv. Protein Chem.* **14**, 1 - 67.

Kentsis, A. and Sosnick, T. R. (1998). Trifluoroethanol promotes helix formation by destabilizing backbone exposure: desolvation rather than native hydrogen bonding defines the kinetic pathway of dimeric coiled coil folding. *Biochemistry* **37**, 14613 - 14622.

Khurana, R., Ionescu-Zanetti, C., Pope, M., Li, J., Nielson, L., Ramirez-Alvarado, M., Regan, L., Fink, A. L. and Carter, C. A. (2003). A general model for amyloid fibril assembly based on morphological studies using atomic force microscopy. *Biophys. J.* **85**, 1135 - 1144.

Kupczik, I. (2004). Vollständiger Verlust des Ichs. *Welt am Sonntag.* July 25th . **30**, 51.

Lee, J. and Pilch, P. F. (1994). The insulin receptor: structure, function and signalling. *Am. J. Physiol. (Cell Physiol.)* **266**, C319 - C334.

Linke, R. P. (1996). Amyloidosen. In *Klinische Immunologie*, (eds. H. H. Peter and W. J. Pichler) pp. 822 - 833. Urban & Scharzenberg, Munich, Vienna, Baltimore.

Löffler, G. and Petrides, P. E. (1990). *Physiologische Chemie*, 4th ed., 1st corr. reprint, Springer-Verlag, Berlin, Heidelberg, New York, London, Paris, Tokyo.

Magonov, S. N. and Whangbo, M.-H. (1996). *Surface analysis with STM and AFM. Experimental and theoretical aspects of image analysis*, VCH Verlagsgesellschaft mbH, Weinheim, New York, Basel, Cambridge, Tokyo.

Magonov, S. N., Elings, V. and Whangbo, M.-H. (1997). Phase imaging and stiffness in tapping-mode atomic force microscopy. *Surf. Sci.* **375**, L385 - L391.

Marcus, R., Ravi, T., Gmitter, T., Chin, K., Liu, D., Orvis, W., Ciarlo, D., Hunt, C. and Trujillo, J. (1990). Formation of silicon tips with 1 nm radius. *Appl. Phys. Lett.* **56**, 236 - 238.

Markiewicz, P. and Goh, M. C. (1995). Atomic force microscope tip deconvolution using calibration arrays. *Rev. Sci. Instrum.* **66**, 3186 - 3190.

Martin, L. D., Vesenka, J. P., Henderson, E. and Dobbs, D. L. (1995). Visualization of nucleosomal substructure in native chromatin by atomic force microscopy. *Biochemistry* **36**, 4610 - 4616.

Mazia, D., Schatten, G. and Sale, W. (1975). Adhesion of cells to surfaces coated with polylysine. *J. Cell Biol.* **66**, 198 - 200.

McCormick, M. and Quinn, L. (2002). Treatment of type 2 diabetes mellitus: Pharmacologic intervention. *J. Cardiovasc. Nurs.* **16**, 55 - 67.

Möller, C., Allen, M., Elings, V., Engel, A. and Müller, D. J. (1999). Tapping-mode atomic force microscopy produces faithful high-resolution images of protein surfaces. *Biophys. J.* **77**, 1150 - 1158.

Moelbert, S., Normand, B. and De Los Rios, P. (2004). Kosmotropes and chaotropes: modelling preferential exclusion, binding and aggregate stability. *Biophys. Chem.* **112**, 45 - 57.

Morris, V. J., Kirby, A. R. and Gunning, A. P. (1999). *Atomic Force Microscopy for Biologists*, Imperial College Press, London.

Mozhaev, V. V., Heremans, K., Frank, J., Masson, P. and Balny, C. (1996). High pressure effects on protein structure and function. *Proteins* **24**, 81 - 91.

Müller, D. J., Engel, A. and Amrein, M. (1997). Preparation techniques for the observation of native biological systems with the atomic force microscope. *Biosens. Bioelectron.* **8**, 867 - 877.

Müller, D. J., Fotiadis, D., Scheuring, S., Müller, S. A. and Engel, A. (1999). Electrostatically balanced subnanometer imaging of biological specimens by atomic force microscope. *Biophys. J.* **76**, 1101 - 1111.

Müller, D. J., Janovjak, H., Leht, T., Kürschner, L. and Anderson, K. (2002). Observing structure, function and assembly of single proteins by AFM. *Prog. Biophys. Mol. Biol.* **79**, 1 - 43.

Munishkina, L. A., Phelan, C., Uversky, V. N. and Fink, A. L. (2003). Conformational behaviour and aggregation of α-synuclein in organic solvents: Modelling the effects of membranes. *Biochemistry* **42**, 2720 - 2730.

Nanosensors™ (2004). *Point Probe®Plus Non Contact- High ResonanceFrequency-Reflex Coating (PPP-NCHR) - Infobooklet*, NanoWord AG, Neuchatel.

Nettleton, E. J., Tito, P., Sunde, M., Bouchard, M., Dobson, C. M. and Robinson, C. V. (2000). Characterization of the oligomeric states of insulin in self-assembly and amyloid fibril formation by mass spectrometry. *Biophys. J.* **79**, 1053 - 1065.

Nielsen, L., Khurana, R., Coats, A., Frokjaer, S., Brange, J., Vyas, S., Uversky, V. N. and Fink, A. L. (2001a). Effect of environmental factors on the kinetics of insulin fibril formation: Elucidation of the molecular mechanism. *Biochemistry* **40**, 6036 - 6046.

Nielsen, L., Frokjaer, S., Brange, J., Uversky, V. N. and Fink, A. L. (2001b). Probing the mechanism of insulin fibril formation with insulin mutants. *Biochemistry* **40**, 8397 - 8409.

Nielsen, L., Frokjaer, S., Carpenter, J. F. and Brange, J. (2001c). Studies of the structure of insulin fibrils by Fourier transform infrared (FTIR) spectroscopy and electron microscopy. *J. Pharm. Sci.* **90**, 29 - 37.

Nielson, M. R. and Dobson, C. M. (2003). Chemical modification of insulin in amyloid fibrils. *Protein Sci.* **12**, 2637 - 2641.

Onuchic, J. N. and Wolyness, P. G. (2004). Theory of protein folding. *Curr. Opin. Struct. Biol.* **14**, 70 - 75.

Panick, G. and Winter, R. (2000). Pressure-induced unfolding/refolding of ribonuclease: A static and kinetic Fourier transform infrared spectroscopy study. *Biochemistry* **39**, 1862 - 1869.

PDB, *Brookhaven National Laboratory's Protein Data Base*, Internet site: http://www.rcsb.org/pdb/, last update: April 2005.

Peretz, D., Williamson, R. A., Legname, G., Matsunaga, Y., Vergara, J., Burton, D. R., DeArmond, S. J., Prusiner, S. B. and Scott, M. R. (2002). A change in the conformation of prions accompanies the emergence of a new prions strain. *Neuron* **34**, 921 - 932.

Pertinhez, T. A., Bouchard, M., Tomlinson, E. J., Wain, R., Ferguson, S. J., Dobson, C. M. and Smith, C. J. (2001). Amyloid fibril formation by a helical cytochrome. *FEBS Lett.* **495**, 184 - 186.

Perutz, M. F., Finch, J. T., Berriman, J. and Lesk, A. (2002). Amyloid fibers are water-filled nanotubes. *Proc. Natl. Acad. Sci. U.S.A.* **99**, 5591 - 5595.

Pethica, J. B. and Oliver, W. C. (1987). Tip surface interactions in STM and AFM. *Phys. Scr.* **T19**, 61 - 66.

Physik Instrumente (2004). PZT unit cell. *Online tutorial info-booklet concerning piezoceramic actuators.* Internet site: http://www.physikinstrumente.de/ products/section4/link1.php, last update: 26.11.2004, Physik Instrumente GmbH & Co. KG, Karlsruhe.

Pohl, D. W. (1991). Scanning near-field optical microscopy (SNOM). *Adv. Opt. EM.* **12**, 243 - 312.

POVRAY, version 3.6, *3D-graphic creator*. Internet site: http://www.povray.org, Persistence of Vision Raytracer Pty. Ltd.

Ptitsyn, O. B. (1995). Molten globule and protein folding. *Adv. Protein Chem.* **47**, 83 - 229.

Radmacher, M., Fritz, M., Hansma, H. G. and Hansma, P. K. (1994). Direct observation of enzyme activity with the atomic force microscopy. *Science* **265**, 1577 - 1579.

Randolph, T. W., Seefeldt, M. and Carpenter, J. F. (2002). High hydrostatic pressure as a tool to study protein aggregation and amyloidosis. *Biochim. Biophys. Acta* **1595**, 224 - 234.

Rao, S. S. (1995). *Mechanical Vibrations*, 3rd ed., Addison-Wesley, New York.

Rief, M., Gautel, M., Oesterhelt, F., Fernandez, J. M. and Gaub, H. E. (1997). Reversible unfolding of individual titin immunoglobulin domains by AFM. *Science* **276**, 1109 - 1112.

Rochet, J. C. and Lansbury, P. T. (2000). Amyloid fibrillogenesis: Themes and variations. *Curr. Opin. Struct. Biol.* **10**, 60 - 68.

Rodríguez, T. R. and García, R. (2003). Theory of Q control in atomic force microscopy. *Appl. Phys. Lett.* **82**, 4821 - 4823.

Royer, C. M. (2002). Revisiting volume changes in pressure-induced protein unfolding. *Biochim. Biophys. Acta* **1595**, 201 - 209.

Russel, P.E. (2001).  SEM and AFM: Complementary techniques for high resolution surface investigations. Lecture given on the *2001 Pittsburgh Conference Symposium "Applications of Scanning Probe/Atomic Force Microscopy"*.

Saborio, G. P., Permanne, B. and Soto, C. (2001). Sensitive detection of pathological prion protein by cyclic amplification of protein misfolding. *Nature* **411**, 810 - 813.

Sakharov, D. V., Jie, A. F. H., Bekkers, M. E. A., Emeis, J. J. and Rijken, D. C. (2001). Polylysine as a vehicle for extracellular matrix-targeted local drug delivery, providing high accumulation and long-term retention within the vascular wall. *Arteioscler. Thromb. Vasc. Biol.* **21**, 943 - 948.

San Paulo, Á. and García, R. (2001). Tip-surface forces, amplitude, and energy dissipation in amplitude-modulation (tapping-mode) force microscopy. *Phys. Rev. B* **64**, 193411-1 - 193411-4.

Sarid, D., Ruskell, T. G., Workman, R. K. and Chen, D. (1996). Driven nonlinear atomic force microscopy cantilevers: From noncontact to tapping modes of operation. *J. Vac. Sci. Technol. B* **14**, 864 - 867.

Schabert, F. A. and Engel, A. (1994). Reproducible acquisition of *Eschericia coli* porin surface topographs by atomic force microscopy. *Biophys. J.* **67**, 2394 - 2403.

Schlote, W., Riede, U.-N. and Wiestler, O. D. (1993). Nervensystem. In *Allgemeine und spezielle Pathologie*, (eds. U.-N. Riede and C. P. Adler), 3rd ed., chap. 19. 1022 - 1093. Georg Thieme Verlag, Stuttgard, New York.

Selkoe, D. J. (1991). The molecular pathology of Alzheimer's disease. *Neuron* **6**, 487 - 498.

Senden, T. J., Drummond, C. J. and Kekicheff, P. (1994). Atomic force microscopy: Imaging with electrical double layer interactions. *Langmiur* **10**, 358 - 362.

Serpell, L. C. (2000). Alzheimer's amyloid fibrils: Structure and assembly. *Biochim. Biophys. Acta* **1502**, 16 - 30.

Shlyakhtenko, L. S., Potaman, V. N., Sinden, R. R. and Lyubchenko, Y. L. (1998). Structure and dynamics of supercoil-stabilzed DNA cruciforms. *J. Mol. Biol.* **280**, 61 - 72.

Sipe, J. D. and Cohen, A. S. (2000). History of the amyloid fibril. *J. Struct. Biol.* **130**, 88 - 98.

Sluzky, V., Tamada, J. A., Klibanov, A. M. and Langer, R. (1991). Kinetics of insulin aggregation in aqueous solutions upon agitation in the presence of hydrophobic surfaces. *Proc. Natl. Acad. Sci. U. S. A.* **88**, 9377 - 9381.

Smeller, L., Rubens, P. and Heremans, K. (1999). Pressure effect on the temperature-induced unfolding and tendency to aggregate of myoglobin. *Biochemistry* **38**, 3816 - 3820.

Srisailam, S., Kumar, T. K. S., Rajalingam, D., Kathir, K. M., Sheu, H.-S., Jan, F.-J., Chao, P.-C. and Yu, C. (2003).Amyloid fibril formation in all β-barrel protein. *J. Biol. Chem.* **278**, 17701 - 17709.

Stark, M., Möller, C., Müller, D. J. and Guckenberger, R. (2001). From images to interactions: High-resolution phase imaging in tapping-mode atomic force microscopy. *Biophys. J.* **80**, 3009 - 3018.

Stefani, M. and Dobson, C. M. (2003). Protein aggregation and aggregate toxicity: new insights into protein folding, misfolding diseases and biological evolution. *J. Mol. Med.* **81**, 678 - 699.

Strausser, Y. E., Diebold, D. B. and Huff. H. R. (1994). Measurement of silicon surface microroughness with AFM. *Extended Abstracts of the 185ᵗʰ Meeting of the ECS in Pennington, NJ.*, **94-1**, 461.

Sulchek, T., Hsieh, R., Adams, J. D., Yaralioglu, G. G., Minne, S. C., Quate, C. F., Cleveland, J. P., Atalar, A. and Adderton, D. M. (2000). High-speed tapping mode imaging with active Q control for atomic force microscopy. *Appl. Phys. Lett.* **76**, 1473 - 1475.

Sunde, M., Serpell. L. C., Bartlam, M., Fraser, P. E., Pepys, M. B. and Blake, C. C. F. (1997). Common core structure of amyloid fibrils by synchrotron x-ray diffraction. *J. Mol. Biol.* **273**, 729 - 739.

Sunde, M. and Blake, C. C. F. (1997). The structure of amyloid fibrils by electron microscopy and X-ray diffraction. *Ad. Protein Chem.* **50**, 123 - 159.

Sunde, M. and Blake, C. C. F. (1998). From the globular to the fibrous state: Protein structure and structural conversion in amyloid formation. *Quarterly Rev. Biophys.* **31**, 1 - 39.

Tanaka, M., Chien, P., Naber, N., Cooke, R. and Weissman, J. S. (2004). Conformational variations in an infectious protein determine prion strain differences. *Nature* **428**, 323 - 328.

Taylor, M. E. (1993). Dynamics of piezoelectric tube scanners for scanning probe microscopy. *Rev. Sci. Instrum.* **64**, 154 - 158.

Thomas, P. D. and Dill, K. A. (1993). Local and nonlocal interactions in globular proteins and mechanisms of alcohol denaturation. *Protein Science* **2**, 2050 - 2065.

Thompson, L. K. (2003). Unraveling the secrets of Alzheimer's β-amyloid fibrils. *Proc. Natl. Acad. Sci. U. S. A.* **100**, 383 - 385.

Timasheff, S. N. (1993). The control of protein stability and association by weak interactions with water: How do solvents affect these processes? *Annu. Rev. Biomol. Struct.* **22**, 67 - 97.

Timasheff, S. N. (1998). Control of protein stability and reactions by weakly interacting cosolvents: The simplicity of the complicated. *Adv. Protein Chem.* **51**, 355 - 432.

Timasheff, S. N. (2002). Protein-solvent preferential interactions, protein hydration, and the modulation of biochemical reactions by solvent components. *Proc. Natl. Acad. Sci. U.S.A.* **99**, 9721 - 9726.

Tompkins, B. (1999). *MultiMode™ SPM Instruction Manual*, Version 4.31ce, Digital Instruments Veeco Metrology Group, Santa Barbara.

Tremblay, P., Ball, H. L., Kaneko, K., Groth, D., Hegde, R. S., Cohen, F. E., DeArmond, S. J., Prusiner, S. B. and Safar, J. G. (2004). Mutant PrP$^{Sc}$ conformers induced by a synthetic peptide and several prions strains. *J. Virol.* **78**, 2088 - 2099.

Tuite, M. F. (2004). The strain of being a prion. *Nature* **428**, 265 - 267.

Turnell, W. G. and Finch, J. T. (1992). Binding of the dye congo red to the amyloid protein pig insulin reveals a novel homology amongst amyloid-forming peptide sequences. *J. Mol. Biol.* **227**, 1205 - 1223.

Uversky, V. N. and Fink, A. L. (2004). Conformational constraints for amyloid fibrillation: The importance of being unfolded. *Biochim. Biophys. Acta* **1698**, 131 - 153.

Vanik, D. L., Surewicz, K. A. and Surewicz, W. K. (2004). Molecular basis of barriers for interspecies transmissibility of mammalian prions. *Mol. Cell* **14**, 139 - 145.

Vigenaud, V. du., Sifferd, R. H. and Sealock, R. R. (1933). The heat precipitation of insulin. *J. Biol. Chem.* **102**, 521 - 533.

Villarrubia, J. S. (1996). Scanned probe microscope tip characterization without calibrated tip characterizers. *J. Vac. Sci. Technol. B* **14**, 1518 - 1521.

Wadsworth, J. D. F., Hill, A. F., Joiner, S., Jackson, G. S., Clarke, A. R. and Collinge, J. (1999). Strain-specific prion-protein conformation determined by metal ions. *Natl. Cell. Biol.* **1**, 55 - 59.

Walgers, R., Lee, T. C. and Cammers-Goodwin, A. (1998). An indirect chaotropic mechanism of the stabilization of the helix conformation of peptides in aqueous trifluoroethanol and hexafluoro-2-propanol. *J. Am. Chem. Soc.* **120**, 5073 - 5079.

Waugh, D. F. (1948). Regeneration of insulin from insulin fibrils by the action of alkali. *J. Am. Chem. Soc.* **70**, 1850 - 1857.

Weissmann, C., Enari, M., Klohn, P. C., Rossi, D. and Flechsig, E. (2002). Molecular biology of prions. *Acta Neurobiol. Exp.* **62**, 153 - 166.

Whangbo, M.-H., Bar, G. and Brandsch, R. (1998). Description of phase imaging in tapping mode atomic force microscopy by harmonic approximation. *Surf. Sci.* **411**, L784 - L801.

Whittingham, J. L., Scott, D. J., Chance, K., Wilson, A., Finch, J., Brange, J. and Dodson, G. G. (2002). Insulin at pH 2: Structural analysis of the conditions promoting insulin fibre formation. *J. Mol. Biol.* **318**, 479 - 490.

Wiesendanger, R. and Güntherodt. H. J. (1992 and 1993). *Scanning Tunnelling Microscopy*, vol. I, II and III, Springer Verlag, Heidelberg.

Winter, R. and Noll, F. (1998). *Methoden der Biophysikalischen Chemie*, Teubner, Stuttgard.

Yang, D. S., Yip, C. M., Huang, T. H. J., Chakrabartty, A. and Fraser, P. E. (1999). Manipulating the amyloid-β aggregation pathway with chemical chaperones. *J. Biol. Chem.* **274**, 32970 - 32974.

Yang, J., Mou, J., Yuan, J.-Y. and Shao, Z. (1996). The effect of deformation on the lateral resolution of atomic force microscopy. *J. Microscopy* **182**, 106 - 113.

Yao, Z.-P., Zeng, Z.-H., Li, H.-M., Zhang, Y., Feng, Y.-M. and Wang, D. C. (1999). Structure of an insulin dimer in an orthorhombic crystal: the structure analysis of a human insulin mutant (B9 Ser → Glu). *Acta Crystallog. sect. D* **55**, 1524 - 1532.

Zhang, Y., Whittingham, J. L., Turkenburg, J. P., Dodson, E. J., Brange, J. and Dodson, G. G. (2002). Crystallization and preliminary crystallographic investigation of a low-pH native insulin monomer with flexible behaviour. *Acta Crystallog. sect. D* **58**, 186 - 187.

Zhu, X. and Ohtsu, M. (eds.) (1999). *Near-field Optics: Principles and Applications*, World Scientific Publishing, Singapore.

# Lebenslauf

| | |
|---|---|
| Name | Ralf Jansen |
| Geburtsdatum | 23.10.1968 |
| Geburtsort | Wesel |

## Schulausbildung

| | |
|---|---|
| September 1975 bis Juli 1979 | Grundschule in Spellen |
| September 1979 bis Juni 1988 | Gymnasium der Stadt Voerde |
| Juni 1988 | Allgemeine Hochschulreife |

## Wehrdienst

| | |
|---|---|
| Juli 1988 bis September 1989 | ABC/SE-Ausbildung in Goslar |
| | Fla-Rak-Generatorentechnik in Delmenhorst und Elsfleth |

## Industriepraktika

| | |
|---|---|
| August 1990 | Benteler AG in Dinslaken |
| April bis Juni 1993 | Henkel KGaA in Düsseldorf |

## Studium

| | |
|---|---|
| Oktober 1990 bis Oktober 1994 | Studium der Chemietechnik an der Universität Dortmund |
| Oktober 1994 bis März 2002 | Studium der Chemie an der Universität Dortmund |
| August 2001 bis März 2002 | Diplomarbeit „Rasterkraftmikroskopische Untersuchungen von Biopolymeren an festen Grenzflächen" |
| 15. März 2002 | Diplom |
| Mai 2002 | Beginn der Promotion am Lehrstuhl für Physikalische Chemie I bei Prof. Dr. R. Winter, Universität Dortmund |
| 27. Oktober 2005 | Disputation |

## Berufstätigkeit

| | |
|---|---|
| Mai 2001 bis März 2002 | Wissenschaftliche Hilfskraft |
| April 2002 bis Juni 2005 | Wissenschaftlicher Angestellter |